Three-Dimensional Effects of Tsunami Impact on Bridges

Hin Kei Wong

A thesis submitted in partial fulfillment of
the requirements for the degree of

Master of Science in Civil Engineering

University of Washington

2015

Reading Committee:

Michael R. Motley, Co-Chair

Marc O. Eberhard, Co-Chair

Pedro Arduino

Program Authorized to Offer Degree:
Department of Civil and Environmental Engineering

University of Washington

Abstract

Three-Dimensional Effects of Tsunami Impact on Bridges

Hin Kei Wong

Co-Chairs of the Supervisory Committee:
Assistant Professor Michael R. Motley
Department of Civil and Environmental Engineering

Professor Marc O. Eberhard
Department of Civil and Environmental Engineering

Field investigations following major tsunamis in recent years have shown that damage to and loss of bridge structures can cause delays in disaster relief and recovery. The damaged bridges were subject to extreme fluid loads such as uplift due to buoyancy and overturning from wave impacts, and these loads are not currently considered within bridge design practice. In response, some studies regarding fluid-bridge interactions have been done; however, they primarily focused on two-dimensional analyses of the bridge. The objective of this work was to examine three-dimensional fluid-bridge interactions utilizing the computational fluid dynamics solver OpenFOAM with a multiphase fluid solver and a Reynolds-Averaged Navier-Stokes (RANS) based turbulence model. Numerical test cases were validated by existing data from flume tests to examine capabilities of OpenFOAM in modelling fluid-bridge interactions. Subsequently, three-dimensional models were developed to examine geometric modifications to the bridge including skewness, grading and superelevation of bridge decks. These modifications were incorporated to resemble common bridge designs. Results showed a clear correlation between forces on the bridge structures and changes in the geometry of the superstructure and these effects should be properly considered in future designs.

TABLE OF CONTENTS

LIST OF FIGURES

ACKNOWLEDGMENTS

I am grateful to Dr. Michael Motley and Dr. Marc Eberhard, my advisers, whose expertise, guidance, patience and support made this work possible. Thank you for offering me a genuinely extraordinary research experience and having faith in my abilities. It has been an absolute pleasure to work with you. I would also like to thank Dr. Pedro Arduino for reviewing my thesis.

Financial support from the National Science Foundation and Dr. Richard Fragaszy, program manager, through Grant No. CMMI-1344615 is gratefully acknowledged. The use of Hyak, a high-performance computing, storage and networking infrastructure, in this work was supported in part by the University of Washington eScience Institute.

Chapter 1
INTRODUCTION

1.1 Sources of Tsunamis

Earthquakes in subduction zones are known for their capability of producing tsunamis. The sequence of tsunami formation in a subduction zone is illustrated in Figure 1.1. First, the subducting plate slips under the overriding plate the two interlock with each other at the plate boundary. Then, stress in the stuck zone increases as the plates squeeze in, causing the overriding plate to bulge upward. When the interlocked plates break free in an earthquake, the overriding bounces back and creates a tsunami.

The Pacific Plate has multiple subduction zones with records of tsunamis, including the Cascadian subduction zone adjacent to the West Coast of the U.S. Figure 1.2 shows that recent tsunamis in Indonesia (2004), Japan (2009), Samoa (2009) and Chile (2009) were all near the subduction zones [3]. The Cascadian subduction zone, just off the coast of Washington and Oregon states, is no exception to creating devastating tsunamis. The Cascadian subduction zone sets off megathrust earthquakes at an average interval of 500 years. Geological evidence and plant remains buried under soil deposits have related tsunamis on the West Coast to the known earthquakes. Past events, such as the 1946 Aleutian Islands tsunami, the 1960 Great Chilean tsunami and the 1964 Alaska tsunami killed hundreds of people in total and damaged numerous buildings in United States [11]. Today, about 3,475,000 residents in the States of Alaska, California, Hawaii, Oregon and Washington are at directly at risk of tsunami impact [8]. With the last major tsunami from the Cascadian subduction zone occurring in 1700, a megathrust earthquake may set off a tsunami in the U.S. at any time [4].

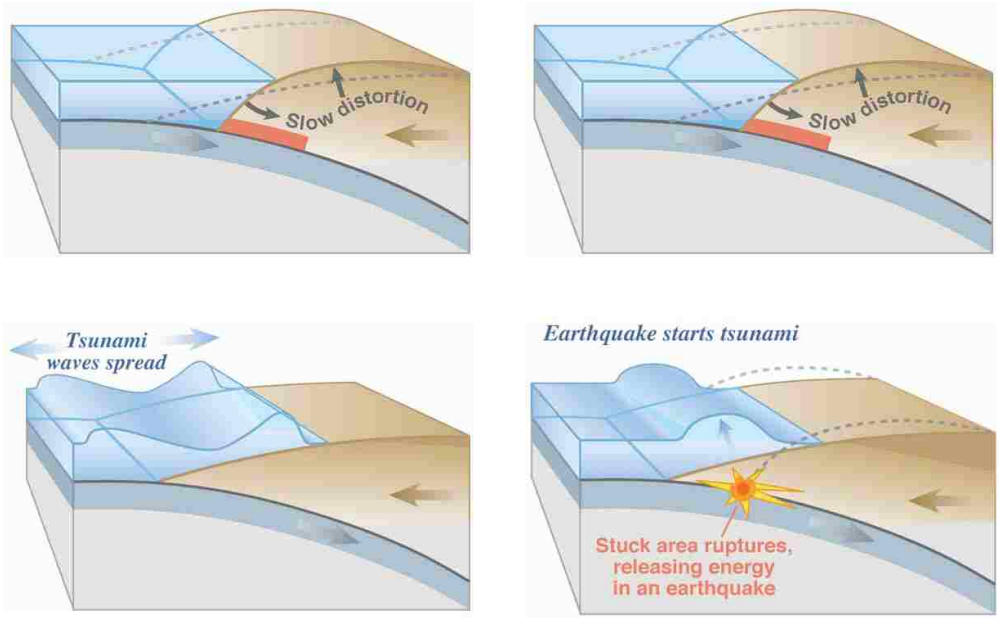

Figure 1.1: Schematic of the formation of a tsunami in a subduction zone arranged in clockwise direction. (Credits: USGS [3])

Following the 1946 and 1964 tsunamis, the National Oceanic and Atmospheric Administration established the Pacific Tsunami Warning Center and West Coast & Alaska Tsunami Warning Center respectively. The tsunami warning centers deploys sensors in Pacific Ocean, monitors for signs of tsunamis and issues warnings to communities in danger [25]. While tsunami warning systems contribute to timely evacuations of people, structures remained unprotected and have generally not designed to withstand tsunamis.

1.2 Role of Bridges Following Tsunamis

Tsunamis can have a major impact on coastal communities, taking away lives, and causing significant damage to buildings and infrastructure systems. Upon reaching the shore, the large amount of water wipes out weaker structures in low-lying areas, and creates large-scale damage and devastation. The extent of tsunami inundation depends on the local topography. Flooding caused by the 2011 Tōhoku tsunami damaged lands that were 7 miles away from the

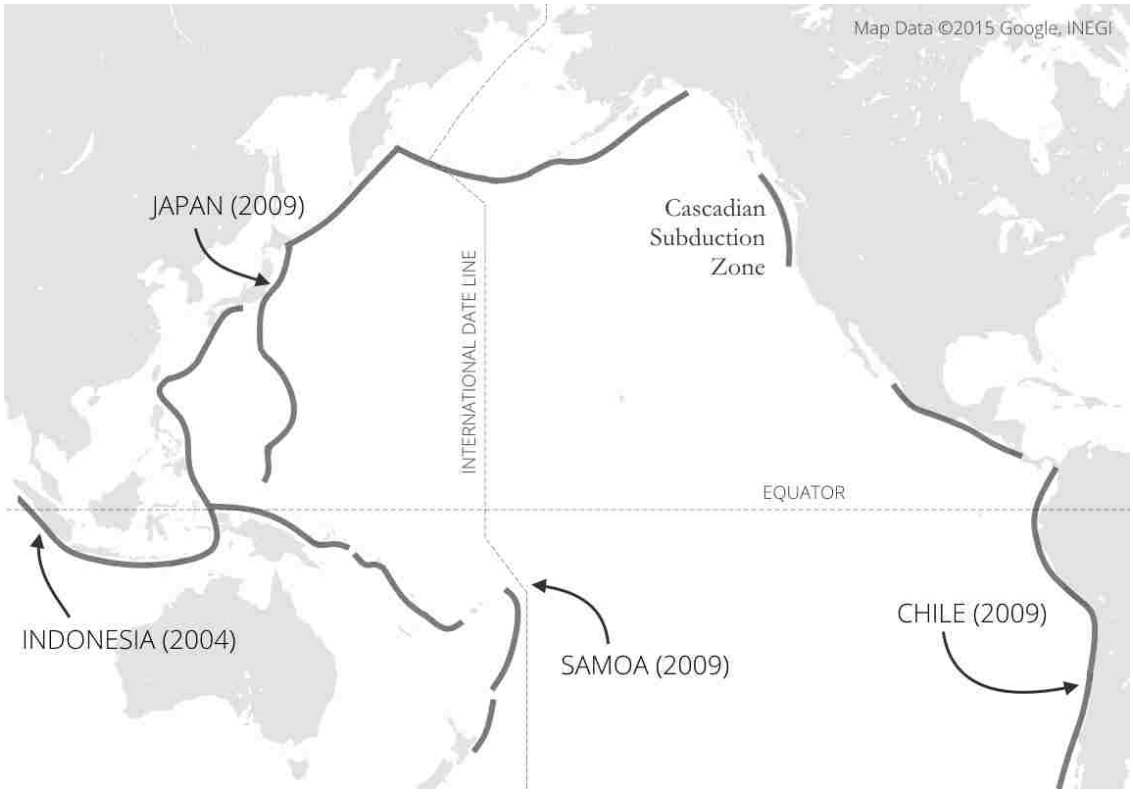

Figure 1.2: Major tsunamis in around the Pacific Plate since 2000 and approximate locations of subduction zones.

shore and damaged over 162,000 buildings in Miyagi Perfecture [13]. The economic impacts from the tsunami put Japan into its worst crisis since World War II, with direct material damage as high as $300 billion, estimated by the Japanese government [15].

Disaster relief has played a significant role in providing a lifeline to survivors of tsunamis. Records show that rescue efforts following tsunami events have been made as early as the Edo Period in Japan. Documents from the year 1700 describe Kuwagasaki (today's Miyako, Iwate, Japan) having been hit by a tsunami at night and having lost over thirty houses. Following the tsunami, magistrates nearby distributed rice to villages who fled to high ground and provided wood for building temporary shelters [4]. Today, the essence of disaster management continues to be support of humanitarian needs and help with recovery of affected

communities. When a disaster strikes a region, governments and international organizations strive to send their rescuers and workers to the hardest-hit areas as quickly as possible. Unfortunately, the experiences of recent tsunamis have demonstrated that dispatching workers and cargo is frequently challenging, because much of the infrastructures is unusable. Washed away roadways, abandoned vehicles and bridge damage made ground transportations impossible following recent events. As a result, relief coordinators could not distribute goods to survivors in need, even though supplies from foreign aid were arriving nearby ports and warehouses. [5, 30].

Gaining access to affected locations is an important aspect of emergency response. Response relief efforts after a tsunami require access to isolated areas. Often, bridges are crucial links to travel across rough terrains. For example, following the 2004 Sumatra tsunami, hundreds of bridges in Indonesia and Thailand were severely damaged and closed. Consequently, roadways to isolated areas were cut off. Until temporary crossings such as the Bailey bridges were deployed to reestablish access to disaster zones, airlift by a limited number of helicopters was the only mean of effective transportation, emphasizing the importance of operational bridges in post-tsunami logistics [12]. Similar issues were seen in the 2011 Tōhoku tsunami when bridges were washed away, causing significant delay in disaster relief and recovery in the regions [17].

Not all bridges hit by tsunami waves were unusable; surveys following the 2011 Tōhoku tsunami revealed that bridges with strong supports survived impacts from waves and debris. In particular, bridges that were properly designed or retrofitted to satisfy seismic requirements generally performed well under lateral fluid load and debris impacts even though they were not intentionally designed to withstand a tsunami. One bridge in Miyako, Japan, sustained only minor damage despite being impacted by a boat that went over a nearby seawall. Some bridges were fully overtopped by tsunami flows mixed with debris and sustained no significant damage to their structural components apart from missing guardrails. In contrast, bridges that did not have adequate strength were much more severely damaged. Some bridge columns were disjointed from their foundations by high velocity flows and then tipped

over. In addition, precast girder bridges with weak uplift resistance were unseated from their abutments and hammerhead beam caps. Field investigators believed that air trapped between girders and around beam caps by rising water created substantial buoyancy and help displace the bridge superstructures [32]. In areas where the flow velocity was high enough, the flow overturned the bridge decks or, with oblique wave fronts, applied an uplift force and carried the decks away. To prevent similar failures from tsunami loads, bridges must be designed to withstand tsunami loads. [10, 21].

1.3 Vulnerability of U.S. Bridges to Tsunamis

Recent events have shown that U.S. infrastructure may fail in the same manner as seen in the Sumatra and Tōhoku tsunamis. When Hurricanes Ivan (2004),Katrina (2005), and Sandy (2012) hit the East Coast, they brought storm surges that flooded and damaged bridges in coastal regions. For example, bearings and fixed connections supporting bridge girders were torn by surge-induced loads. Bridge spans were shifted if not overturned or carried away. Tugboats and barges collided with piers and misaligned bridges. The floods also eroded infill in abutments and caused scouring around piles, which led to foundation failure [20, 26]. Investigators linked damage observed in storm surges to those in tsunami inundations and recommended considerations of hydrostatic uplift and buoyancy when designing bridges [28].

A design code that considers tsunami loads and their effect on bridges is needed to minimize damage to bridge structures. As of today, there is no building or bridge code that takes tsunami loads into account. The upcoming ASCE/SEI 7-16 *Minimum Design Loads For Buildings and Other Structures* is expected to include a chapter on tsunami loads and effects, and serves as the first national standard for structural engineering that addresses tsunami risk and minimum design loads. However, the equivalent standard in bridge engineering, *AASHTO LRFD Bridge Design Specifications* has no provisions on tsunami design. While FEMA P646 *Guidelines for Design of Structures for Vertical Evacuation from Tsunamis* provides recommendations on vertical structure designs such as scouring near foundations and estimation of tsunami loadings, the guidelines are not be suitable for bridge superstructures

[6, 19].

Despite the fact that bridges serve as lifelines to survivors after earthquake and tsunami events, bridges have received much less attention in the research related to tsunami engineering. Almost all past tsunami research has studied inundation modelling, emergency management, and only recently, the structural design of buildings and foundations. Whereas many surveys of post-event damage to bridge structures have been published after each major tsunami, many of the models for tsunami loading on bridges are inadequate. Only when engineers understand the behavior of bridge structures during tsunamis can guidelines for bridge design considering tsunami loads be made.

1.4 Previous Numerical Modeling

Post-tsunami field investigations have shown that the level of damage is often correlated to the three-dimensional geometry of the bridge and the surrounding bathymetry. For example, skewed bridges have been found to be more vulnerable to unseating [7, 9]. Numerical tsunami-bridge modelling in the past has often been limited to two-dimensional analyses due to very high computational demands. Models were built in a two-dimensional computational domain to reduce the total number of degrees of freedom, so that the models would take less time to compute; even then, they could take days to run on a parallelized system [33]. Although two-dimensional analyses are faster to run than their three-dimensional counterparts, they cannot capture three-dimensional effects of non-uniform geometric properties of bridge structures, local bathymetry and turbulence. Unjoh et al., Ren et al. and other researchers have performed two-dimensional analyses which essentially model a cross-section of a bridge and assume a uniform load across the bridge superstructure only, excluding the aforementioned three-dimensional effects [31, 27, 33].

Technological advancements have made computing power drastically more affordable, giving researchers the ability to solve three-dimensional fluid dynamics problems in a reasonable timeframe. Still, no studies have looked into the three-dimensional effects of bridge geometries on tsunami load predictions. For example, Nimmala et al. performed a case study

of the Spencer Creek Bridge on Highway 101 in Oregon using LS-DYNA. The actual bridge designed was modeled and tested with a tsunami model tailored to the local geographic characteristics. Since it was a case study for a particular bridge, no other bridge geometry was tested [23]. Lau et al. focused on modelling how a tsunami would flow around a 30 m span of concrete I-girder bridges commonly constructed in countries around the Indian Ocean using Flow-3D, a computational fluid dynamic program that solves transient and three-dimensional flow problems. The study focused on how fluid load changed with respect to bridge deck clearance rather than changing the span's geometry [18]. Other researchers attempted to use finite element methods (e.g. OpenSEES), smooth particle hydrodynamics and material point method to approximate tsunami loads on bridges; however, those methods have been outperformed by OpenFOAM in force predictions [24].

1.5 Research Objectives

The primary goal of work presented here is to evaluate the effects of changes in the three-dimensional geometry of a bridge superstructure, specifically skew, slope and superelevation, on predicted tsunami loads for a typical girder bridge. Analyses were performed using OpenFOAM, an open-source computational fluid dynamics software package. The ability to model tsunami-bridge problems was first validated with existing experimental flume test data of a standard bridge (i.e., no skew, grade, or superelevation). Then, three-dimensional effects of bridge geometries are investigated by modifying the validated bridge structure. As this has not yet been presented elsewhere in the relevant literature, specific trends will be evaluated and initial recommendations will be made. Ultimately, these results will provide a valuable step toward the development of probabilistic performance-based tsunami engineering criteria for the design of tsunami-resilient bridges. This thesis is organized as follows. Chapter 2 presents the methodology of numerical modeling of tsunami impacts on bridges using OpenFOAM, and the validation results of the method are discussed in Chapter 3. Analyses of skew, slope and superelevation effects are presented in Chapter 4 through 6, followed by the conclusion (Chapter 7).

Chapter 2
METHODOLOGY

This chapter describes the numerical modeling strategy used to model the effects of tsunamis on bridges. The key features of the strategy include:

- Understanding how OpenFOAM functions as a computational fluid dynamics software toolbox.
- Mesh generation of the bridge models that has high efficiency and high fidelity.
- Wave generation as a dam-break problem in a flume and the corresponding boundary conditions and initial values for the problem.
- Assignments of fluid properties, such as laminar and turbulent flow models.

The strategy was applied to three-dimensional bridge geometries that spanned across a flume. The validation of the numerical model with experimental flume test data from a previous study is presented in Chapter 3. It was assumed that the wave generated in the experiment was a representative wave model of an actual tsunami.

2.1 Introduction to OpenFOAM

OpenFOAM, the acronym for "Open Field Operation and Manipulation", is an open-source software toolbox that was originally designed to solve a wide range of problems using computational fluid dynamics (CFD). The toolbox can solve fluid dynamics problems involving compressible and incompressible flows, multiphase flows and buoyancy-driven flows for which both laminar and turbulent solvers are available. OpenFOAM also comes with a variety of

applications called utilities, helping users prepare files for analyses and post-process results. All solvers are self-contained program executables; users may customize their workflow by running analyses with any combinations of utilities and solvers that are compatible. In fact, the OpenFOAM developers encourage users to create their own applications to extend the functionalities of the toolbox. All components in OpenFOAM are written in C++ programming language and distributed under GNU general public license (GPL), giving users the freedom to modify any part of the codes and recompile the program as long as terms in the license are not violated. The copy of OpenFOAM used in this work, version 2.3.1, is also used in modeling of combustion, heat transfer, solid mechanics and magnetism, and has been seen in both commercial and academic projects from many engineering disciplines [29].

The open-source nature of OpenFOAM allows users to deploy the software in virtually any computing device with a C++ compiler. Without any cost associated to the CFD software package, setting up a system that runs OpenFOAM is highly flexible and economical compared to proprietary software packages commonly used in CFD.

The source code for OpenFOAM is available for download on the OpenFOAM Foundation's website (`http://www.openfoam.org/download/`) and Git repository. Users with Ubuntu operating systems may also consider using Ubuntu's Advanced Packaging Tool (APT). Since software running on different environments may behave differently, the procedures for setting up analysis cases may vary. Solving a CFD problem generally involves setting up the case, running the case with a solver, and interpreting the results. OpenFOAM provide utilities for doing all necessary jobs, from pre-processing to post-processing.

Because the models developed in this work need to consider both the water and air in the domain, the solver used should be able to handle multiphase flows. The analyses also include wave generation and subsequent flow due to gravity. The built-in two-phased incompressible flow solver `interFoam` can be configured to accomplish these requirements. In addition to determining an appropriate solver, an understanding of the desired quantities for post-processing is important, because OpenFOAM needs instructions for which output variables should be stored. Ultimately for this work, the goal is to determine forces acting

on the bridge, wave velocities and height at sampling points, and the appropriate output variables to determine these quantities are discussed below.

2.2 File Structure of an OpenFOAM Case

OpenFOAM organizes data into various files and directories according to their purposes. Each OpenFOAM case has its own *case directory*, which contains all of the files needed to run a case. While most of the files used by OpenFOAM solvers as input parameters are written in C++ language, the files are simply for data storage purposes and contain almost no programming algorithms. OpenFOAM has many solvers that perform a wide range of analyses, and each type of analyses has a unique requirement of files and input parameters. Files that define parameters used by a solver are called *dictionaries*. The file structure presented in this section holds true for the `interFoam` analyses performed in this work.

2.2.1 Main Directories

Directory `0`

The `0` directory stores files that define boundary conditions and initial values. It serves as the initial time directory from which OpenFOAM reads information needed to compute results in the first time step. Mandatory files include `alpha1`, `p_rgh` and `U`, which describe boundary conditions of volumetric ratio, gravity-corrected pressure and flow velocity, respectively. Depending on the fluid model, additional files may be required to fully define the initial conditions. For example, a k-ϵ turbulence model requires an additional file `k` to define boundary conditions and initial values for turbulent kinetic energy.

Time Directories

OpenFOAM stores output into time directories at a user-specified interval of time. Each directory is named after the time step in which output is written. Note that during an OpenFOAM run, the solver does not read results from these time directories. However, a

case run can be restarted using a dataset stored in a specific time directory instead of starting from time zero.

Directory `constant`

Quantities and definitions that remain constant throughout an analysis are stored in the `constant` directory. They include physical properties of fluids, turbulence model definitions and mesh descriptions. Files that are part of the mesh descriptions are put into a sub-directory called `polyMesh`.

Directory `system`

The `system` directory has dictionaries that control the solution algorithm used. The directory contains the following mandatory files: `controlDict`, which specifies parameters that control a run such as time step increments, start and end times, output formats, maximum Courant number, etc.; `fvSchemes` which outlines the numerical discretization scheme to be used in solving partial differential equations; and `fvSolution` which defines the equation solver and smoothers and states tolerances and relaxations for solving equations. Some utilities that request user input choose to have their dictionaries stored in the `system` directory or as a sub-dictionaries in `controlDict`.

Directory `postProcessing`

This directory stores some results that are not part of the data required by the solver. Rather, the results are usually requested by users using utilities. An example would be forces exerted on a patch in the mesh, which could be derived by summing pressures applied to the patch over its area (a patch is defined as a group of cell faces). If no additional results are requested, this directory will not be created.

2.3 Mesh Generation

A mesh is the discretization of a domain where fluid flows and interacts with boundaries. Often, most physical features presented in the problem are included in the form of a boundary. Physical features come in all different shapes. While major features, such as regularly-shaped flume and channel walls can easily be modeled with large blocks of finite volumes, irregular objects such as complex bathymetries or bridge deck and substructure components are much more difficult to define by manually typing in the coordinates, and proper mesh refinement study for these complex geometries is impractical through manual development of the mesh. OpenFOAM provides a variety of utilities to automate the mesh generation process using different methods. For this work, mesh generation requires the creation of a background mesh of a simple rectangular prism, inclusion of the complex geometric components within the background mesh, and the systematic refinement detailed below.

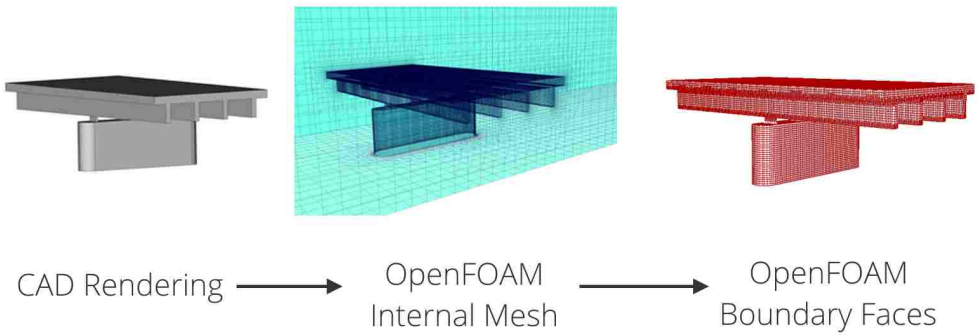

Figure 2.1: Bridge structures in CAD rendering and OpenFOAM mesh.

Resolution of physical features is driven by cell density around the features. Large cells in the background mesh may not capture details and lead to errors. Also, tessellations of spherical shapes and curved surfaces with small amount of cells are likely to result in crude polygonal edges. Thus, regions with complex geometries need relatively small cells. One way to resolve resolution issues is to use a very fine background mesh. However, a mesh with

many small cells demands impractical computational power and time during the analysis as a tradeoff. Ideally, only regions with sharp features should have high-level of refinement while the rest of the mesh should remain coarse. OpenFOAM provides settings to identify regions which need more grid cells and adaptively adjust the level of refinements.

2.3.1 Background Mesh

The background mesh is defined as a rectangular block using a utility called `blockMesh`. The purpose of the background mesh is to provide a crude and easily implemented mesh for further refinements of details. In this work, the background mesh is simply a structured mesh with the same dimensions as the flume. `blockMesh` is used for generating the background mesh because of its simplicity in defining a structured mesh. The parameters that specify how the background mesh is created are stored in `<case dir>/constant/polyMesh/blockMeshDict`. To create a rectangular block of cells, the three-dimensional Cartesian coordinates of vertices used in the mesh are first given. Next, a hexahedron that defines the boundary of the flume is created using vertices defined previously along with the number of cells needed in each direction. Uniformly distributed cells are defined by the argument `simpleGrading (1 1 1)` in the block definition, which means the cell expansion ratio along all edges is 1, i.e., all cells have the same size. Lastly, each face of the block is named and given a boundary type `wall` to designate all faces of the block are physical boundaries instead of internal faces.

2.3.2 Mesh Refinement

The bridge structures are incorporated into the mesh with `snappyHexMesh`, a utility that removes hexagonal cells from a background mesh with reference to three-dimensional computer-assisted drawing (CAD) models. The amount of time needed to mesh irregular objects, such as wide-flange girders, circular columns, and guardrails, increases drastically as the level of detail grows. `snappyHexMesh` is a tool tailored for converting CAD models into a mesh that conforms to complex geometries.

2.3.3 Preparation of CAD Model

The CAD model to be meshed can be either an ASCII or a binary stereolithography (STL) file format. Surfaces in a CAD model are triangulated into smaller triangles, called facets. The three-dimensional cartesian coordinates of three vertices of the facets and their unit normal are recorded into STL files [1]. STL file formats are widely supported by 3D CAD applications including FreeCAD 0.16, an open-source application used in this work to create bridge models. The STL files are stored in `<case dir>/constant/triSurface/`.

While `snappyHexMesh` reads triangulated surfaces from STL files directly, it requires definitions of the feature edges on the topography. The underlying cause of this requirement is that STL files do not store definitions of feature edges but only those of surfaces. OpenFOAM needs to know where feature edges are to implement sharp mesh boundaries. This is done using `surfaceFeatureExtract`, which recognizes features based on topography angles as defined in `<case dir>/system/surfaceFeatureExtractDict`. The utility will write a basic edge mesh file in OpenFOAM's native .eMesh format for each STL file supplied in `<case dir>/constant/triSurface/`. When a user executes `snappyHexMesh`, the utility looks into the directory and loads both the STL mesh files and the corresponding eMesh files.

2.3.4 Setup for `snappyHexMesh`

`snappyHexMesh` includes three features to conform a mesh to the surface of the CAD model. All necessary parameters are defined in `<case dir>/system/snappyHexMeshDict`. The first step, `castellatedMesh`, projects the CAD model into the background mesh and removes all cells that cross the surfaces of the CAD model. In the next step, (`snap`), the jagged surfaces after cell removal are smoothed by replacing original cells near the surfaces with smaller ones and subsequently distorting them to fit curved and nonorthogonal surfaces. Lastly, additional layers of hexahedral cells may be added to surfaces where irregular cells are unwanted; this last step (`addLayers`) is not used in this work, since the quality of the meshes generated using the first two steps was deemed acceptable.

Parameters that control the removal of cells are defined under the subdictionaries called `snappyHexMeshDict.castellatedMeshControls`, and they are explained below.

- `maxLocalCells` limits the maximum number of cells handled per processor before switching to a weighted balancing method in domain decompositions, and it is set to be 1,500,000,000.

- `maxGlobalCells` limits the maximum global cell count, where beyond that number refinements will stop, and is set to be 2,000,000,000. Both numbers are set to be much higher than the number of cells expected throughout the refinement process, since computational power during mesh refinements is not a concern.

- `minRefinementCells` is generally set to 1, meaning that refinement will be performed if at least one cell meets the criterion specified in this subdictionary.

- `maxLoadUnbalance` is set to 0.1 to allow a maximum of 10% cell unbalancing during the processes, which means any processors are permitted to process up to 10% more cells than the average workload in parallel computing. If `snappyHexMesh` is executed with one processor only, all settings related to load balancing are irrelevant. Then, the eMesh mesh edge files are loaded with `level 0` to keep the edges as they are defined in the mesh edge files without refinement.

- `locationInMesh` is set to be a point located within the flume. This signifies to the utility to keep the part of the mesh in which the point is located as opposed to the part which is about to be discarded.

- The level of `refinementSurfaces` is set to the minimum and maximum refinement level respectively. Each refinement level is a transition from the original cell size to roughly a quarter of that size.

- Step `snap` is controlled by the subdictionary `snappyHexMesh.snapControls`, which defines how smoothing is enforced. In each iteration, the boundary faces are relaxed and set back to get as close to the surface defined by the STL file as possible, as illustrated in Figure 2.2. The number of iterations of smoothing, mesh displacement relaxation, and cell snapping used in this work were set tp 2, 5 and 10 respectively. In practice, the number of iterations needed depends on the complexity of the structure being meshed.

- Finally, there is also a subdictionary `snappyHexMesh.meshQUalityControls` that controls the distortion and size limits on new cells generated

2.3.5 Modifications for Two-Dimensional Analysis

Two-dimensional analyses in OpenFOAM's `interFoam` solver are performed by using a mesh that is one-cell thick, resulting in a de facto two-dimensional mesh. Therefore, meshes with more than one cell in their thickness will not work, as information is passed in three dimensions. This characteristic becomes problematic when meshes are generated by `snappyHexMesh`, because the utility does not allow differential refinement levels in all three Cartesian coordinate directions. Even if the background mesh is originally one cell thick, `snappyHexMesh` will split cells in the thickness direction, resulting in a three-dimensional mesh. Therefore, the refined mesh must be processed by the `extrudeMesh` utility to reduce the mesh back to one-cell thick, resulting in a two-dimensional domain.

`extrudeMesh` is set-up by dictionary `<case dir>/system/extrudeMeshDict`. When reducing number of cells in the thickness direction, extrudeMesh works by extruding the `left` patch (which is the `sourcePatches` in the dictionary) to the `right` patch (the `exposedPatchName`) and filling the new mesh with just one layer of cells (`nLayers 1`). This method of extruding cells from one patch to another parallel patch is called `linearNormal` in OpenFOAM.

2.4 Fluid Properties

Modelling tsunami-bridge interaction involves dual-phase analyses. The two phases of fluid are water and air, which are both modelled as incompressible. Properties of the fluids, including density, viscosity, etc. are defined. Each cell also has a quantity that describes the water-to-air ratio, called `alpha1`, with 1 being purely water and 0 being purely air. Initial water depth is then defined by assigning cells with `alpha1` equals to 1.

2.4.1 Incompressibility Assumption

The two fluids, water and air, are modelled as incompressible flows in OpenFOAM. Both fluids in the models are expected to travel at a speed much slower than Mach 0.3, and can be considered to exhibit no compressibility. Thus, they can be modelled as incompressible flows. This allows the use of `interFoam` solver, as it only works with fluids that are incompressible[16].

2.4.2 Physical Properties

The physical properties of the fluids are stored in `<case dir>/constant/transportProperties`.Standard values for the physical properties of air and water are used. Note that SI (m, kg, s) units are used for all OpenFOAM analyses presented in this work. . Gravity is 9.81 m/s^2 negative y-direction, and is specified in file `<case dir>/constant/g`.

2.4.3 Flow Models

Both laminar and turbulent flow models are investigated. The choice of flow model is specified in file `<case dir>/constant/turbulenceProperties`. Cases with a laminar flow model has `simulationType` set to be `laminar`; no additional setting is required. The turbulent cases use a Reynolds-Averaged Navier-Stokes (RANS) k-ϵ model. In OpenFOAM, the RANS model is designated as the Reynolds-Average Simulation (RAS) solver. To use the k-ϵ model, `simulationType` is set to `RASModel`. An additional file called `RASProperties` stored in

directory `constant` is necessary, in which `RASModel`, `turbulence` and `printCoeffs` are set to be `kEpsilon`, `on` and `on` respectively.

2.5 Boundary Conditions

Definitions of boundary conditions for all patches are stored in the directory `<case dir>/0`. Boundary condition files are named corresponding to the field that they represent. In each file, the initial values for internal field (`internalField`) and boundary fields (`boundaryField`) are specified. Values associated with the internal field are assigned to all cells that are not part of any boundary. Similarly, values associated with the boundary fields will be assigned to the faces of cells that coincide with the physical boundaries. Two types of physical boundaries exist in the model. The first one is of type `wall`, which means no fluid can flow across the boundary. This boundary condition includes the walls of the flume walls and all bridge components. Another type of physical boundary is the atmosphere, which corresponds to the open-top of the flume.

2.5.1 Volumetric Ratio `alpha1`

As noted above, `alpha1` values of 1 and 0 represent water and air, respectively. The internal field has a value of `uniform 0`, which means the flume initially contains air only. All walls are type `zeroGradient`, meaning that the boundaries do not change the value of `alpha1`. Physically, the walls do not change water to air or vice versa, so the walls should not alter the value of `alpha1`. The boundary type also implies that surface tension effects are not considered.

The atmosphere is type `inletOutlet`, OpenFOAM's designation of a conditional inlet and outlet. `inletOutlet` requires two additional parameters: `initialValue` and `value`. The boundary condition of `alpha1` at top face changes depending on the direction of flow. If the flow velocity at the atmospheric boundary is into the flume, it is assumed that air is flowing in. Hence, the `initialValue` is 0. On the other hand, when the flow velocity is moving out of the flume, the boundary should let the fluid flow outward freely regardless of

whether it is water, air or a mixture of both. Thus, the boundary has a 0 gradient on `alpha1` and does not alter the value of `alpha1`. The boundary cell has an initial `alpha1` value of 0, which is same as the rest of the flume.

Since the top face of the numerical model only replenishes air, any water that flows out of the flume will not travel back to the flume. In reality, however, water that travels through the open-top through splashing may reenter the flume. Since the modelled domain does not include the space above the flume, OpenFOAM has no way of keeping track of where water goes once it crosses the top face. Certainly, there is error associated with this, but the error is assumed to be negligible. The computational cost of modelling the entire space above the flume is not justified for the possible modest improvement in flow estimation, and the amount of water reaching the top face of the domain at any time has been found to be negligible.

2.5.2 Flow Velocity `U`

Fluids are at-rest in the beginning of an analysis to simulate a dam-break problem. At the walls, the boundary condition `U` is required in all three Cartesian coordinate directions. Since the walls are impermeable, the velocity normal to the wall surfaces is zero. In the plane of each wall, the viscous fluid (water) has no relative velocity with respect to the wall, i.e., the no-slip condition. Thus, a Dirichlet boundary condition of zero velocity in all direction is imposed. In OpenFOAM, the boundary type is `fixedValue` with a value of `uniform (0 0 0);`

At the top face, a boundary type of `pressureInletOutletVelocity` is introduced. It is required for the pressure boundary type `totalPressure` and volumetric ratio boundary type `inletOutlet` to function properly. When the flow is exiting the domain through the top face, the gradient of velocity is zero, i.e., the boundary does not slow the flow down. On the other hand, inflowhas the same velocity as the velocity normal to the boundary patch. Initial value for the velocity at the top face is `uniform (0 0 0)`, which means air is stationary.

2.5.3 Gravity-Corrected Pressure `p_rgh`

Gravity-corrected pressure `p_rgh` refers to the part of static pressure that does not include hydrostatic pressure. Fluid in the flume is assumed to have no `p_rgh` initially; thus, the `internalField` has a value of `uniform 0`. In the first iteration, the solver will compute `p_rgh` in each cell based on gravity and amount of water within the domain.

All walls have the boundary type of `fixedFluxPressure`, which means the solver will adjust the pressure gradient so that the flow across the boundary remains zero while satisfying the velocity boundary condition.

The top boundary type is `totalPressure`, where total pressure is defined as the sum of `p_rgh` and the dynamic pressure as described in Bernoulli's principle. At the top face, the total pressure is set to be the atmospheric pressure, which is zero in gauge pressure. Gauge pressure is chosen to be the method of pressure measurement, because the fluid pressure is compared to the surrounding atmosphere. The dynamic pressure is defined as $\frac{1}{2}\rho U^2$, where ρ and U are fluid density and flow velocity, respectively. `p_rgh` at the top boundary is thus the negative of the dynamic pressure.

2.5.4 Turbulent Kinetic Energy k and Turbulent Dissipation ϵ

The RAS k-ϵ model requires both the turbulent kinetic energy k and turbulent dissipation ϵ to be computed. OpenFOAM takes an initial guess of k and ϵ to start the analysis. Once the analysis begins, the solver will update the values in every time step. Since the solver is able to stabilize the values, the initial guess need not to be exact.

To estimate the turbulent kinetic energy, the flow velocity must first be determined. A numerical wave gauge was set up in a two-dimensional laminar flow case to estimate the velocity of the flow near the bridge deck. Since the flow is created using a laminar model, the flow velocity is expected to be different from one that is generated using a turbulence model. However, the velocity estimated should be accurate enough for the purpose of approximating an initial value of k. From the analysis, the average flow speed $\overline{U}_x$ was visually determined as

0.80 m/s from with a fluctuating component of the velocity $U_x^{'}$ of approximately 0.056 m/s. The fluctuating component of the velocity is the result of turbulence, and we can define:

$$k = \frac{1}{2}(U_x^{'2} + U_y^{'2} + U_z^{'2})$$

Assuming that initial turbulence is isotropic, i. e. $U_x^{'} = U_y^{'} = U_z{'}$, the equation becomes

$$\begin{aligned} k &= \frac{1}{2}(U_x^{'2} + U_x^{'2} + U_x^{'2}) \\ &= \frac{3}{2}(U_x^{'2}) \\ &= \frac{3}{2}(0.056^2) \\ &= 4.704 \times 10^{-3} \text{ J kg/m}^3 \end{aligned}$$

Note that k is expressed per unit mass density.

After k is approximated, the turbulent dissipation term is computed with a turbulence length scale l assumed to be approximately 20% of the width of the flume, i.e., 0.2 m.

$$\begin{aligned} \epsilon &= \frac{0.09^{0.75}k^{1.5}}{l} \\ &= \frac{0.09^{0.75}(4.70 \times 10^{-3})^{1.5}}{0.2} \\ &= 2.651 \times 10^{-4} \text{ m}^2/\text{s}^3 \end{aligned}$$

The computed values of k and ϵ are used to define the initial values of the turbulence parameters. In the `k` boundary condition file, the boundary type for all walls is `kqRWallFunction`, OpenFOAM's RAS k-ϵ model boundary condition. The top boundary is `zeroGradient`, which means it has no effect on the turbulence. Indeed, the free atmosphere is not expected to affect turbulence in the water in our simulations. Similarly, the wall type in the ϵ boundary condition file is `epsilonWallFunction`, and that of the top boundary is `zeroGradient`.

2.5.5 Parallelization

CFD analysis can be very computationally expensiverunning multiple domains of an analysis in parallel with multiple processors greatly reduces the computational time required. Before

running the analyses, the mesh must be decomposed into individual components and assigned to processors along with all of the associated properties such as boundary conditions and fluid properties using `decomposePar`. To run a job in parallel, users may either use the built-in utilities `foamJob`, which automatically select the available Message Passing Interface (MPI), or manually call the MPI and specify how many processors are needed. The number of processors used must match the number of decomposed domains of the mesh.

Post-processing

The output variables from OpenFOAM depend on the instructions given to the solver. In a multiphase fluid problem, typical results include velocities, pressure, density and volumetric fraction of the flow in every cell. Cases that have turbulent properties defined may include parameters specific to the turbulence model chosen. Additional information, such as forces exerted on a specific patch in the mesh, is available via optional utilities.

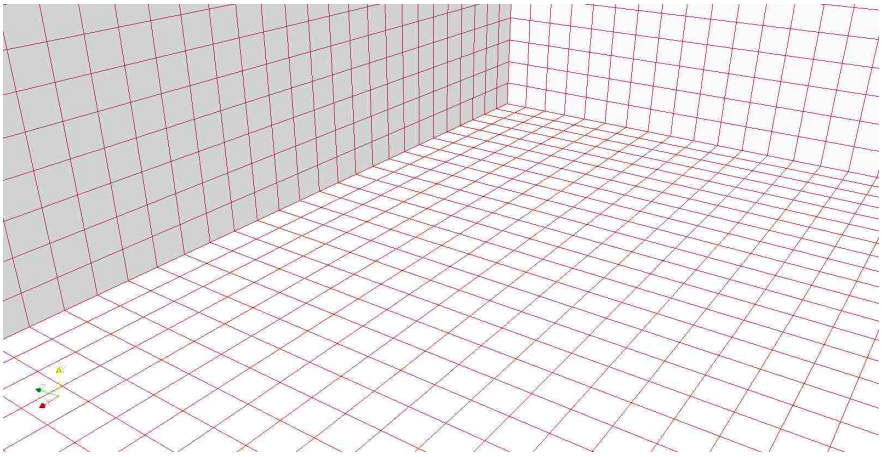

(a) View of the background mesh from inside of the domain.

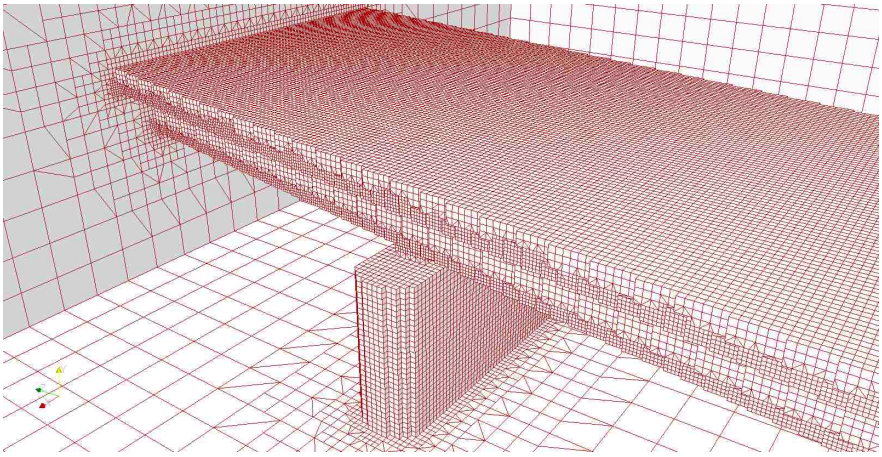

(b) Initial removal of cells to model the bridge structure.

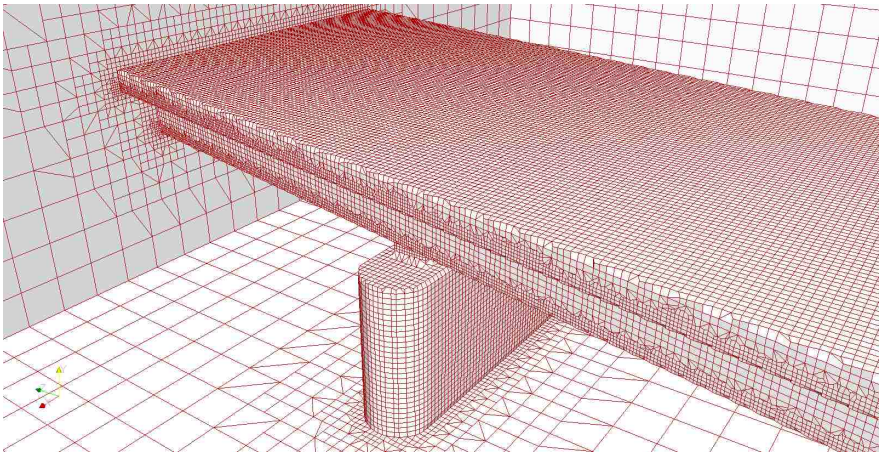

(c) Final mesh where boundary faces are "snapped" to features defined in STL files.

Figure 2.2: Illustration of `snappyHexMesh`.

Chapter 3

VALIDATION

The Public Works Research Institute (PWRI), a civil engineering research agency under the Ministry of Land, Infrastructure, Transport and Tourism in Japan, performed a series of fluid-bridge interaction experiments in a controlled environment in response to massive destruction as a result of the 2011 Tōhoku tsunami [22]. Their setup was modeled in this work to validate the newly developed numerical model. The primary validation used was denoted as Case 2 in the UJNR (**U**nited States and **J**apan established the Cooperative Program in **N**atural **R**esources) Tsunami Modeling Workshop held in Oregon State University in December 2014, which used the same data from PWRI. Two additional cases (Case 3 and Case 4), which vary slightly from case 2, were validated and presented at the end of this chapter.

3.1 Description of the Flume

The validation was performed by modeling a numerical flume and bridge structures after the experimental setup created by PWRI, and then subject the bridge with the same flow conditions as the experiment. The flume is 30-m long (in x-direction), 1-m tall (in y-direction) and 1-m wide (z-direction), as shown in Figure 3.1. For convenience in describing the setup and results, back and front refer to the positive and negative x-directions, respectively; top and bottom refer to the positive and negative y-directions, respectively; and right and left refer to positive and negative z-directions, respectively. A 12-m long reservoir is located at the front end of the flume for wave generation. The reservoir was filled with water to a height of 0.617 m, and the initial water depth in the flume was 0.100 m. When the gate was opened, the wave height at the bridge deck was expected to be 0.20 m. A gauge is placed 1

m in front of the bridge superstructure to monitor flow velocity and wave height.

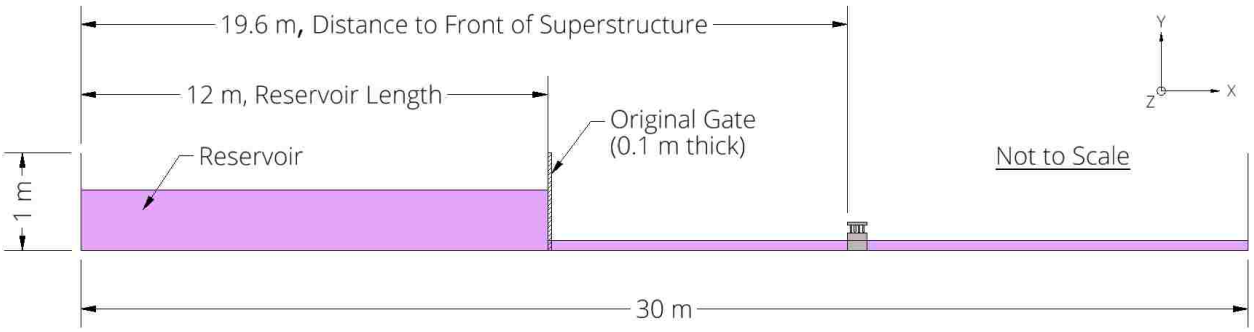

Figure 3.1: Schematic of the flume.

In the PWRI experiment, a 0.1-m thick gate, hinged at the bottom, was used to hold water back from the rest of the flume until a flume test began. Since the gate pivoted about its bottom edge, water would spill out from the top first when the gate dropped. In OpenFOAM, modelling a moving gate with an Eulerian mesh is highly complex. Instead, the analysis was treated as a typical dam-break problem. At the beginning of each analysis, an imaginary dam that holds water back is moved, which causes the water to flow out and create waves. Since water is flowing out of the reservoir instantaneously, there will be no time delay as one would expect with a gate dropping. Consequently, the arrival time, height and velocity of wave at the bridge deck are slightly different from the experimental data. However, the differences are expected to be small and acceptable for engineering applications.

Once the gate is removed, the space originally occupied by the gate is mostly filled with air except for the region near the bottom face of the flume where it will be filled by water to prevent backflow from the initial water depth in the flume. The depth of water there is the same as the rest of the flume. If the space is left empty, water in the flume will flow back at the beginning of the analysis and hit with water coming from the reservoir, creating additional turbulence and splashing.

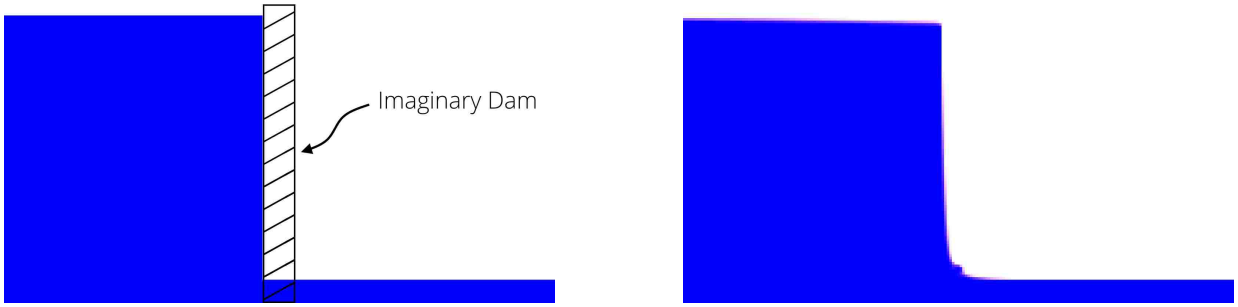

(a) Right before the analysis begins, water in the reservoir (left) stands still as if a dam is holding it back from flowing out.

(b) The analysis begins by removing the imaginary dam. Water flows out of the reservoir from the bottom due to gravity.

Figure 3.2: Illustration of a dam-break problem.

3.2 Description of the Bridge Model

The validation of the capabilities of the `interFoam` multiphase solver is done using bridge model 5 presented in Nakao et. al. [22] Each of the experiments performed used a 1/20-scale model of a prototype bridge. The model-scale bridge superstructure has four 0.02 m wide girders, and the deck is 0.50 m wide. To put it into perspective, the deck at full scale could fit two 3.7-m wide lanes and a sidewalk on each side. When the bridge deck installed into the flume, there is a 7.5 mm spacing between the flume wall and the deck. The superstructure sits on a pier which is mounted to the bottom of the flume parallel to the direction of flow. The pier is 0.51-m long, 0.18-m tall and 0.08-m wide with a 0.04-m radius fillet on each of its front and back end. Bearings on which each girder rests on are also modeled. The dimensions of the bridge structure are given in figure 3.3.

3.3 Similitude

As noted above, the bridge models are 1/20-scale, while the fluid properties for both air and water, as well as gravity, cannot be scaled. The length scale L_{ratio}, gravity ratio g_{ratio}, fluid

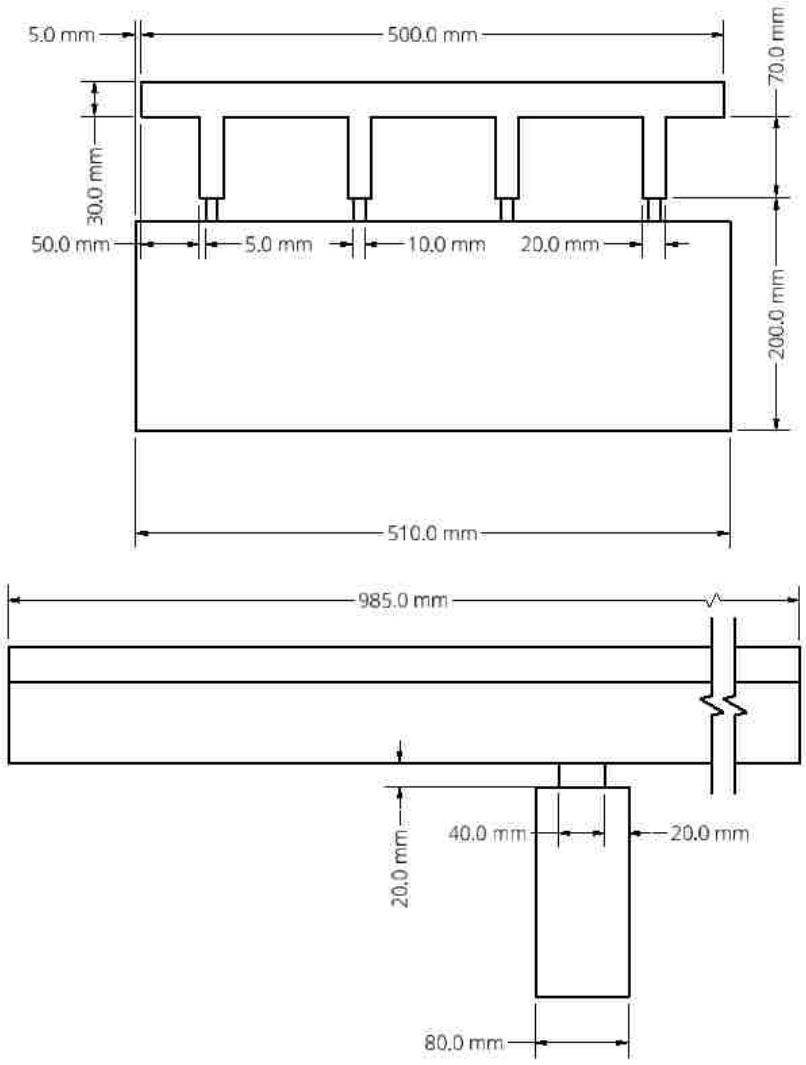

Figure 3.3: Dimensions of the model-scale bridge structure.

density ratio ρ_{ratio} and time scale T_{ratio} are written as

$$0L_{ratio} = \frac{L_{model}}{L_{prototype}} = 1/20$$

$$g_{ratio} = \frac{g_{model}}{g_{prototype}} = 1$$

$$\rho_{ratio} = \frac{\rho_{model}}{\rho_{prototype}} = 1$$

$$T_{ratio} = \frac{T_{model}}{T_{prototype}} = \sqrt{\frac{L_{ratio}}{g_{ratio}}} = \sqrt{\frac{1}{20}}$$

By definition, velocity is the rate of displacement. The velocity of the prototype $V_{prototype}$ can be computed from results of the model as follows:

$$V_{prototype} = \frac{L_{prototype}}{T_{prototype}} = \frac{L_{model}/L_{ratio}}{T_{model}/T_{ratio}} = V_{model}\frac{T_{ratio}}{L_{ratio}} = V_{model}\frac{\sqrt{1/20}}{1/20} = V_{model}\sqrt{20}$$

Similarly, forces in the prototype $F_{prototype}$ can be determined from the model results. Newton's second law of motion says that the vector sum of external force $F = Ma$, where M and a are mass and acceleration of the object of interest, respectively. The object of interest herein refers to the flow being modeled. In addition, a is the rate of change in V, i. e. $a = V/T$. Using the Newton's second law of motion, the definition of a and the ratios defined previously,

$$\begin{aligned} F_{prototype} &= M_{prototype}a_{prototype} = \rho_{prototype}L^3_{prototype} \times \frac{L_{prototype}}{T^2_{prototype}} \\ &= \frac{\rho_{model}}{\rho_{ratio}}\left(\frac{L_{model}}{L_{ratio}}\right)^3 \times \frac{L_{model}/L_{ratio}}{\left(T_{model}/T_{ratio}\right)^2} = F_{model}\frac{T^2_{ratio}}{\rho_{ratio}L^4_{ratio}} \\ &= F_{model}\frac{\left(\sqrt{1/20}\right)^2}{1 \times (1/20)^4} = F_{model} \times 8000 \end{aligned}$$

Quantities presented in this work follow the convention of how results were presented in the experimental results used in the validation. Bridge geometries are presented at model scale, while forces, flow velocities and wave heights are presented corresponding to the full-scale results.

3.4 Two-Dimensional Analysis with Laminar Flow Solver

The first analysis essentially serves as a test platform for getting used to the OpenFOAM environment and utilities. The mesh is one-cell-thick with no bridge pier modelled, and has 40,000 square cells per square meter. The automatic mesh generator `snappyHexMesh` is able to capture the geometry of the girder bridge and preserves all of the orthogonal corners. A laminar flow solver is used to see if it is sufficient to model the wave actions. The two-dimensional mesh and laminar flow solver are computationally cheap compared

to a three-dimensional mesh with a turbulent solver, allowing changes to be made more frequently. Parameters being monitored include horizontal and vertical applied forces on the bridge superstructure, wave height and wave velocity. The wave height is computed based on `alpha1`, and is measured from the initial free surface level to the center of the highest cell that has `alpha1` larger than 0.5. It is important that the highest cell is selected when computing the wave height instead of the first free surface from the bottom, because the wave is a mixed air-water flow that has multiple free surfaces in the entrapped air. To compare results, the numerical results are shifted by -0.5 seconds, i. e. subtracting 0.5 seconds from the original time stamps, so that the peak force at impact from the results matches with the experimental data. The time shift accounts for variations of results due to method of wave generation and simplified boundary conditions in two-dimensional analyses and approximations in the flow model.

While the wave impact followed by a slower post-impact flow is clearly observed from the time histories, neither the time histories of loads, flow velocity, nor wave height are accurate. From figure 3.4, all results show large oscillations which resemble a series of nonphysical waves impacting the bridge superstructure. In the vertical force history, the oscillations are frequently as high as 200% of what the experimental data shows and occur throughout the analysis. This inaccuracy exists because the flow is highly turbulent instead of laminar, as seen in figure 3.5, which makes the laminar flow solver unsuitable.

3.5 Two-Dimensional Analysis with RAS Turbulence solver

With an RAS turbulent solver, results no longer include the large oscillations seen in the laminar flow case. The numerical results are shifted by 1.4 seconds instead of -0.5 seconds in the laminar flow case, suggesting that kinetic energy is lost through turbulence, which slows the flow down. The exact arrival time of the wave impact is not important here; rather, the force predictions are the primary concerns.

The two-dimensional model with the turbulence solver greatly reduces the errors seen in the laminar flow case, although it still overestimates the loads. For the horizontal forces,

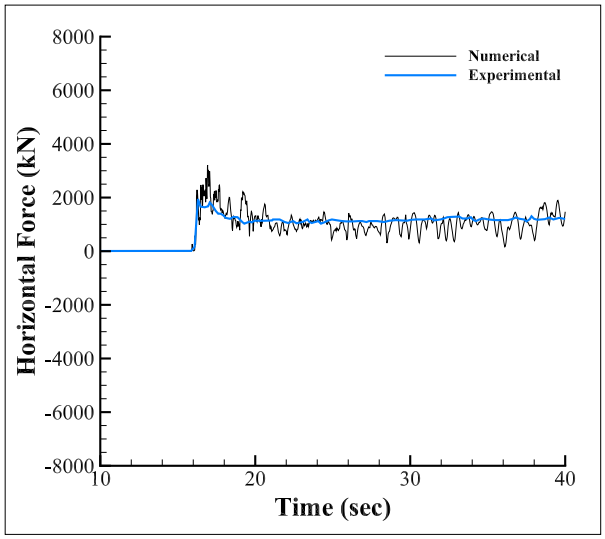

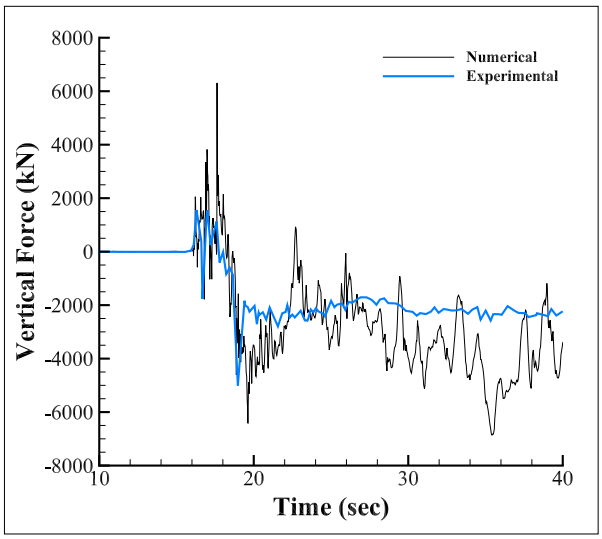

(a) Loads

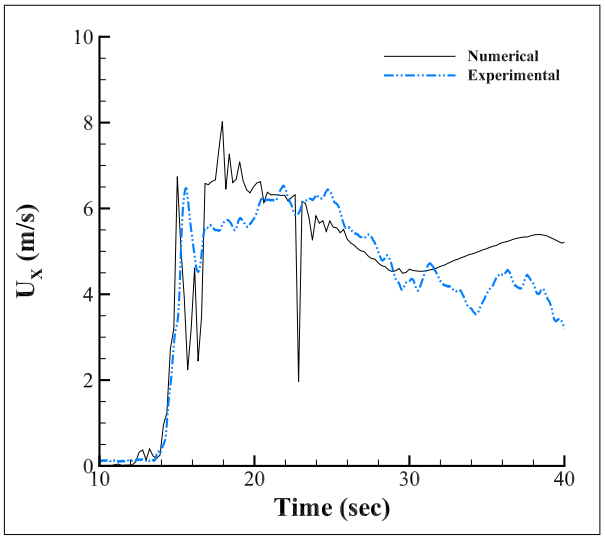

(b) Flow Velocity

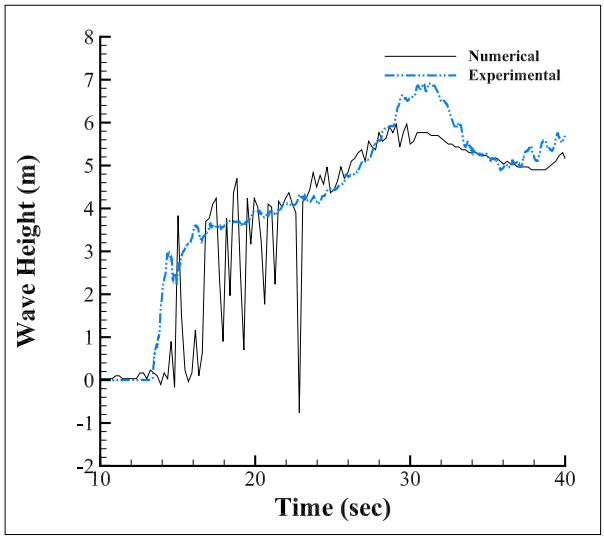

(c) Wave Height

Figure 3.4: Time histories of the two-dimensional laminar flow case.

the model slightly overpredicts both the wave impact and the resulting hydrodynamic drag force following the impact. The vertical force is qualitatively predicted at impact and during the crashing of the wave on the deck that follows; however, the approximated peak force

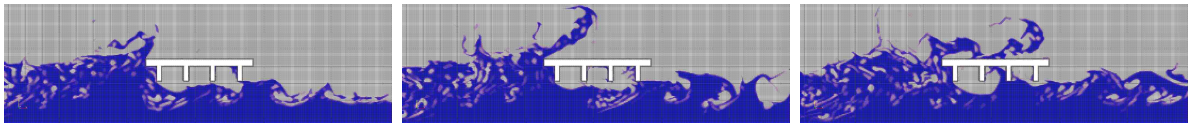

Figure 3.5: Time-lapsed figures (from left to right) of flow mixing and wave breaking near the bridge superstructure during impact in the two-dimensional laminar flow case.

is about 70% too high. In addition, the model predicts less fluid on the top of the deck in post-impact flow, producing a lower magnitude of downward force. One thing noticeable is that the downward force is underestimated throughout most of the analysis. Since the two-dimensional model does not have the 7.5 mm gap between the girder ends and the flume walls, the superstructure traps lots of air underneath the deck and between the girders, resulting in extra buoyancy that provides uplift on the deck. In addition, the boundary conditions prescribed contribute to the overestimation of the forces. In two-dimensional analyses, the left and right wall have a boundary type of `empty`, which means the solver assumes that the boundary does not affect the flow in any way. The `empty` walls may be considered as very flat surfaces that are perfectly smooth. When water flows near the walls, there is no shear stress between the flow and the wall. Since the no-slip boundary condition is not enforced at the walls, there is no dissipation of kinetic energy by shear stress. Also, turbulence does not exist in the z-direction by the definition of the two-dimensional domain. Therefore, there are less eddies dissipating kinetic energy by viscous forces. Thus, the flow travels faster and carries more momentum in the two-dimensional domain than in the experiment, hitting the deck harder than expected.

In reality, the tsunami modelled may or may not need the no-slip condition defined on the left and right boundaries depending on the local bathymetry and landscape. If the site of interest has clearly defined boundaries , e.g. a river or a valley, then the no-slip boundary should be introduced. However, if the site is at the center of a very wide channel or a flood plain, then the actual left and right boundaries of the flow will have little influence on

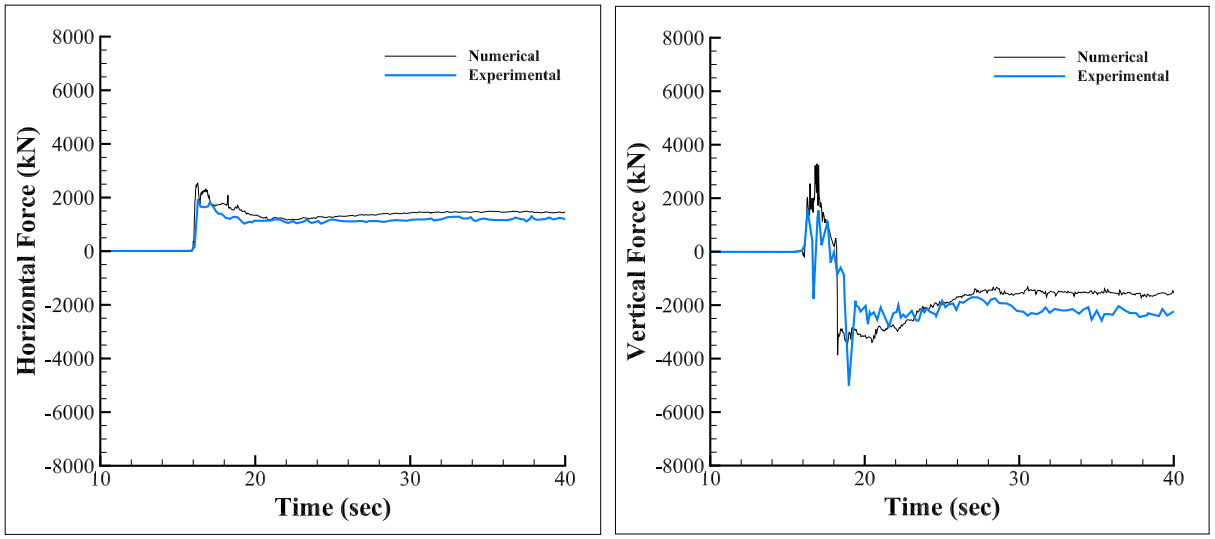

(a) Loads

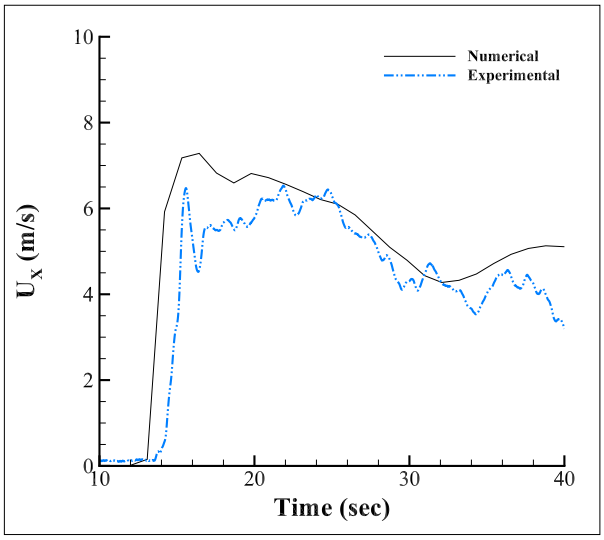

(b) Flow Velocity

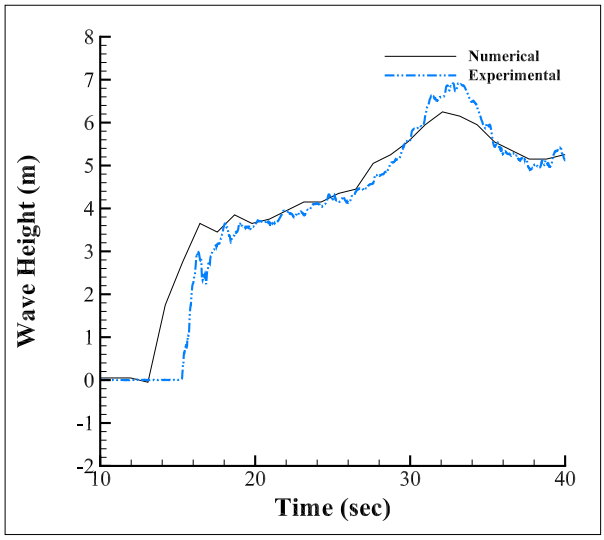

(c) Wave Height

Figure 3.6: Time histories of the two-dimensional turbulent flow case.

the point of interest. In that sense, it may make more sense to apply an `empty` boundary condition to avoid restricting the flow. For our validation purposes, the no-slip condition is desired to reproduce the behavior of flow expected in a flume.

Although the two-dimensional analyses fail to accurately approximate the magnitude of forces, they successfully demonstrate that the RAS solver outperforms the laminar flow solver in modelling the wave travelling through the flume. The RAS solver eliminates the unrealistic oscillations shown in the laminar flow case by accounting for turbulence created by the waves and mixing actions of the fluids.

3.6 Three-Dimensional Analysis

Knowing that the two-dimensional analyses have their inherent weaknesses in dissipating kinetic energy and modelling three-dimensional features, a three-dimensional model is developed to match the experimental setup from PWRI. The three-dimensional mesh includes the bridge pier with rounded face and back faces and girder supports. The background mesh has $600\times20\times20$ cells in the background mesh, and has six level of mesh refinement in the vicinity of the bridge structure. The mesh conforms to the rounded faces of the bridge pier and shows no jagged surfaces. The no-slip boundary condition is enforced on all physical boundaries. As shown in Figure 3.7, the approximated applied horizontal and vertical impact forces at impact are comparable to the experimental results. There is a downward force peak shown in the experimental data at about 19 seconds that the numerical result does not show, but overall the results are consistent with the experimental results. In post-impact flow, the horizontal force is consistently overestimated by 15%, and the vertical force is quantitatively the same as the experimental results. For the purpose of this work, the results are acceptable.

3.7 Additional Validations

Cases 3 and 4 from the UJNR tsunami workshop are validated to ensure the model would function properly in other situations, and they both showed good results in force predictions. The setup is very similar to Case 2; for brevity, only the differences are mentioned. Case 3 has a shallower reservoir (0.518 m) and higher initial water level in the flume (0.150 m). Case 4 has the same initial water conditions as Case 2; however, a fairing shown in figure 3.8 is installed on the impact-side of the deck. The results from Case 3 and 4 (figure 3.9)

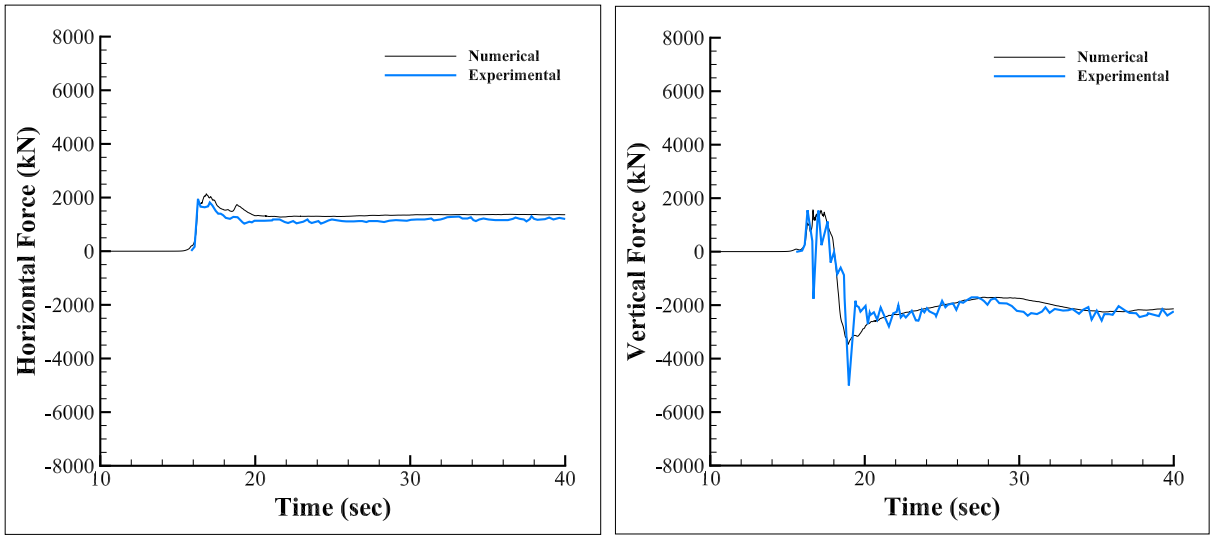

Figure 3.7: Load histories of the three-dimensional turbulent flow case.

suggest that the three-dimensional turbulent model performs as expected.

3.8 Computational Time

Computational fluid dynamics modelling can be very computationally expensive; however, OpenFOAM supports parallelization and dramatically mitigates the large time requirements if the user has access to multiple computing cores. The run time of the validation analyses varies based on whether the two- or three-dimensional domain and/or laminar or turbulent flow solvers are employed. The two-dimensional laminar flow case and the turbulent flow case take about two hours and seven hours using 64 processors, respectively, while the three-dimensional turbulent model takes about 31 hours with 128 processors. Compared to two-dimensional analyses in past studies that cost days to run, the OpenFOAM performance is much more practical.

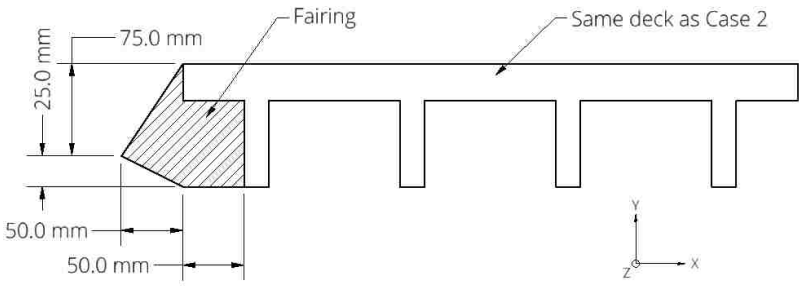

Figure 3.8: Dimensions of the fairing used in Case 4.

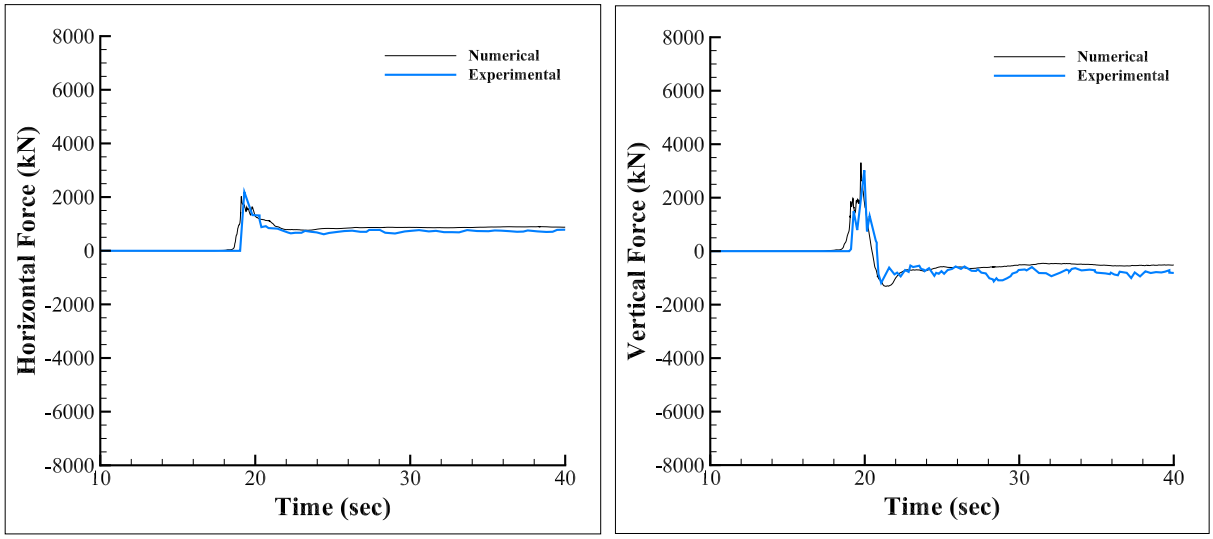

(a) Case 3

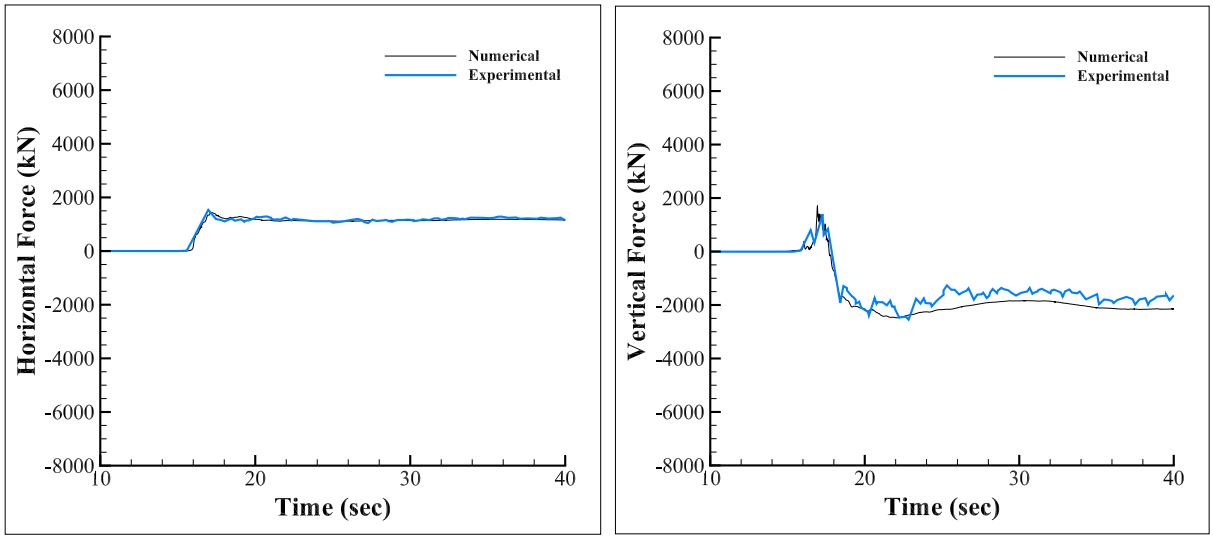

(b) Case 4

Figure 3.9: Load histories of the additionally validated cases.

Chapter 4
SKEWED BRIDGES

Skewed bridges are bridges whose abutments are not perpendicular to the longitudinal direction of a bridge. Such bridges are usually constructed to cross a landscape feature or highway that is not perpendicular to the direction of traffic. The impact of a tsunami on a skewed bridge is different from its impact on an unskewed bridge for three main reasons:

- The skewed bridges have a longer superstructure, which increases the surface areas on which the fluid loads act.

- The angle of attack of incoming wave is not perpendicular to the longitudinal axis of the bridge.

- The wave impacts one side of the bridge before it impacts the other side. Consequently, the bridge superstructure will experience forces and moments that cause the deck to spin and pitch in addition to rolling.

Two-dimensional models cannot represent the three-dimensional geometry of a bridge. Therefore, a series of three-dimensional models were developed to examine how skew angles change the support reactions.

4.1 Orientation of Bridge Decks

Bridge superstructures with skew angles of 5°, 10°, 15°, 20°, 30° and 40° were modelled using the same flume shown in Figure 3.1 and initial water height described in Section 3.1 as the validation Case 2, so that results from the skewed cases could be compared with the unskewed one. The skewed bridges were created by rotating the four-girder bridge span

about its geometric centroid while keeping the position of the geometric centroid unchanged with respect to the flume. The substructure was unchanged and remained parallel to the flow direction, as it would be in practice to reduce flow resistance.

The four corners of the deck are designated by their location (front or back of bridge) and the size of the angle (acute or obtuse) at the deck corners. The front acute and back obtuse corners of the bridge superstructure are located on the right side of the flume, and their nearest girder supports are labelled as FA and BO, respectively. Similarly, the girder supports corresponding to the front obtuse and back acute corners are labelled FO and BA, respectively, and they are on the left side of the flume. The layout of the supports is presented in Figure 4.1.

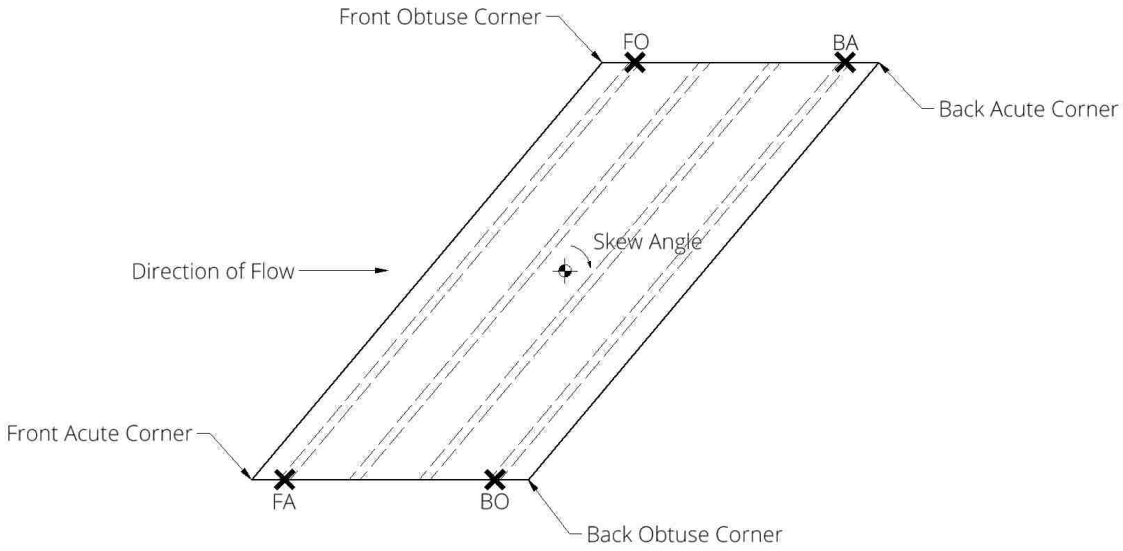

Figure 4.1: Schematic of a four-girder skewed bridge.

Since the front acute corner (FA) is nearest to the reservoir, the wave will arrive at the corner sooner than for the bridge with no skew (Case 2). For the purpose of comparing the results of the analyses, it is assumed that the bridge is sufficiently far away from the reservoir that waves are fully-developed when they impact the bridge structures. Hence, the change in wave height and velocity at the time of impact are negligible.

In all cases, `snappyHexMesh` was able to generate a mesh that conformed to the geometry of the bridge deck regardless of the nonorthogonal alignments of the superstructure and background mesh.

4.2 Notations of the Loads

In describing the loads, F_X, F_Y and F_Z refer to forces applied in X, Y and Z direction respectively, and M_X, M_Y and M_Z refer to moments applied about X, Y and Z axes respectively. In addition, horizontal forces F_H are defined as the square root of the sum of squares of all horizontal loads, i.e. F_X and F_Z. Support reactions are named in the similar manner. Each support reaction is named by the support's name, with a subscript that denotes the directional component of the reaction. For example, FA_H refers to the horizontal reaction at the front acute corner support.

4.3 Decoupling Horizontal Loads from Vertical Reactions

The loads were applied through a point on the plane of supports of the bridge projected vertically from the geometric centroid of the bridge. A skewed bridge with no grade or superelevation runs parallel to the ground, which means all supports have the same elevation. By applying the loads at the plane of supports, there is no eccentricity between the horizontal loads and the horizontal supports. Subsequently, the horizontal loads and reactions do not form moment couples that would otherwise be resisted by vertical reactions. Consequently, the horizontal loads (F_X, and F_Z) and spinning moment (M_Y) are decoupled from the vertical reactions. Similarly, F_Y, M_X and M_Z do not cause any horizontal reactions.

4.4 Calculating Support Reactions

The support reactions of the four-girder bridge were computed using a matrix stiffness method, assuming the superstructure to act rigidly. The pinned girder supports are located on the two ends of the bridge, and the bridge pier is assumed to resist no tsunami loads. Each support was considered to be a node supported by three springs, one in each of

the Cartesian coordinate directions, giving the supports degrees of freedom only in displacements but not rotations. When tsunami loads are applied to the bridge, the springs deform, which allow support reactions to be computed from the spring deformations.

The actual stiffness of the springs is irrelevant in computing the support reactions even though it affects the deformation of the springs, because the same stiffness was used when calculating the support reactions from the spring deformations. For simplicity, the spring stiffness was assumed to be equal, so that forces would be distributed equally to each spring.

4.4.1 Transformation Matrix

A unique transformation matrix **T** relates the applied forces and moments at the origin of loads to the relative resistance of the springs at each support. The matrix has six rows, corresponding to F_X, F_Y, F_Z, M_X, F_Y and F_Z, and three columns, corresponding to the support reactions in X-, Y- and Z- directions.

The applied force in each direction was resisted only by supports in the corresponding direction. Therefore, the transformation factors of the first three rows of **T** are 1 on the diagonal and 0 elsewhere.

The applied moment about each axis was resisted by support reactions in the two directions that were not parallel to the axis, and the magnitude of resistance was determined by the proximity of the support to the origin of loads. For example, Figure 4.2 illustrates that the moment applied about the X-axis is resisted by support reactions in positive Z-direction and negative Y-direction. If the distance from the origin of loads to the support is **r**, then

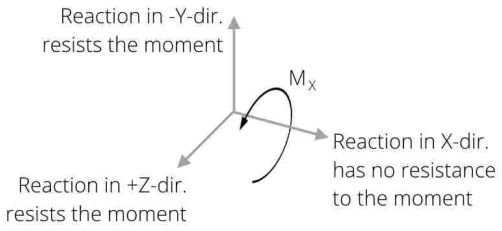

Figure 4.2: Resistance to M_X by support reactions.

$$\mathbf{T} = \begin{bmatrix} 1 & 0 & 0 \\ 0 & 1 & 0 \\ 0 & 0 & 1 \\ 0 & -r_Z & r_Y \\ r_Z & 0 & -r_X \\ -r_Y & r_X & 0 \end{bmatrix}$$

where r_X, r_Y and r_Z refer to the components of $\mathbf{r}$ in the X, Y and Z directions, respectively.

4.4.2 Stiffness Matrix

The local stiffness at a support is a 3×3 matrix that relates the spring force in each direction to the corresponding spring deformation. Let k be the magnitude of the stiffness of all springs. Each of the three springs respond only to their own direction. Then, the local stiffness matrix $\mathbf{k}$ can be written as:

$$\mathbf{k} = \begin{bmatrix} k & 0 & 0 \\ 0 & k & 0 \\ 0 & 0 & k \end{bmatrix}$$

The local stiffness matrix is then transformed into $\mathbf{K}$, which is compatible with the global degrees of freedom using $\mathbf{T}$ by

$$\mathbf{K} = \mathbf{T^T}\ \mathbf{k}\ \mathbf{T}$$

4.4.3 Solving for Support Reactions

At each time step, reactions at a support were computed by premultiplying the force vector $\mathbf{F} = [F_X\ F_Y\ F_Z\ M_X\ M_Y\ M_Z]^\mathbf{T}$ by $\mathbf{K}$ at the support to get the spring deformations, then multiplying $\mathbf{k}$ by the spring deformations to get support reactions in each direction.

4.5 Results

Similar to the unskewed bridge (Case 2), the time histories presented in Figure 4.4 show a rapid increase in forces and moments that correspond to the wave impact, followed by a decay of the load to the steady-state flow regardless of skew angle. The arrival time of the wave slightly changed based on the skew angle, because the front-acute corner of the deck is closer to the reservoir. No time shift was applied to the data to preserve the variations due to skew effects.

The trend of load histories of the 7 skew cases shows a strong correlation with the skew. Since the intermediate angle cases follow the trend, the remaining discussion of skew effects focuses on the two extreme cases — 0° and 40°.

4.5.1 Resultant Forces

As the skew angle increases, the tsunami wave hits the bridge over a longer duration. Unlike an unskewed bridge, the front face of a skewed bridge is not perpendicular to the flow. The skewness puts part of the bridge more upstream than the rest of the structure. When the wave arrives, it impacts the front-acute corner first and gradually spreads to the front-obtuse angle. The distribution of forces over a longer period of time is demonstrated by a wider peak in the load histories in Figure 4.4.

The magnitude of F_X decreases in a skewed bridge at the time of impact but not steady-state. Since the wave does not hit the bridge simultaneously on a skewed bridge, the load is no longer concentrated at a short time frame. In addition, the skewed front face redirects some of the impact loads towards the abutments. Therefore, the maximum magnitude of F_X decreases. On the other hand, F_X is insensitive to the skew angle in steady-state flow, because the projected frontal area and its shape remain the same despite the skew angle of the bridge. When the bridge is subjected to the same flow, the force in the direction of flow is roughly the same.

The skewed front face diverts flow towards the abutments and introduces F_Z to the bridge.

As the skew angle increases, the effect is more pronounced. At 40° skew, the magnitude of F_Z is roughly the same as that of F_X at steady-state.

Skew effects are insignificant to F_Y during impact but drastically decrease the downward force in steady-state. Because a skewed bridge extends to the left and right flume walls, the longer overhang at the front side tends to attract more uplift during impact. The effect is then offset by the reduced force due to the extended duration of impact. Therefore, the peak uplift does not change with skewness. The effect is different in steady-state. Girders of a bridge with higher skew angles are more in-line with the flow. Because water flows through the girders easier, it displaces air between girders more efficiently and provides more support to the deck from bottom. Note that the air between girders in this particular set-up provides little or no upward buoyancy force, because the air is free to escape from the gap between the bridge and the flume walls. Air appears to be trapped simply because the girders shield the fast-moving flow from getting into the voids. Buoyancy exists in the discussion of two-dimensional models which have no gaps between the bridge and the walls, because as soon as the flow slows down and tries to get into the voids, the walls prevent air from escaping and instead force the air to displace water. Figure 4.3 shows that water can easily fill into the voids between girders from the side of the bridge and displace air in the three-dimensional model.

4.5.2 Resultant Moments

Moments about all three axes are sensitive to skew angles. The skewness introduces M_X and M_Y, which are negligible in an unskewed bridge. M_X causes the bridge to go higher on one side of the flume. In the case of a skewed bridge, the initial uplift of the front-acute corner results in a negative M_X. Then, M_X becomes negligible when the resultant uplift force acts at the centerline of the deck. By the time the resultant uplift force acts on the front-obtuse angle, water starts flowing on top of the right side of the deck and makes the magnitude of positive M_X greater than the negative value. Shortly after the impact, water fully overflows the deck while the uplift force diminishes. The shape of the positively skewed

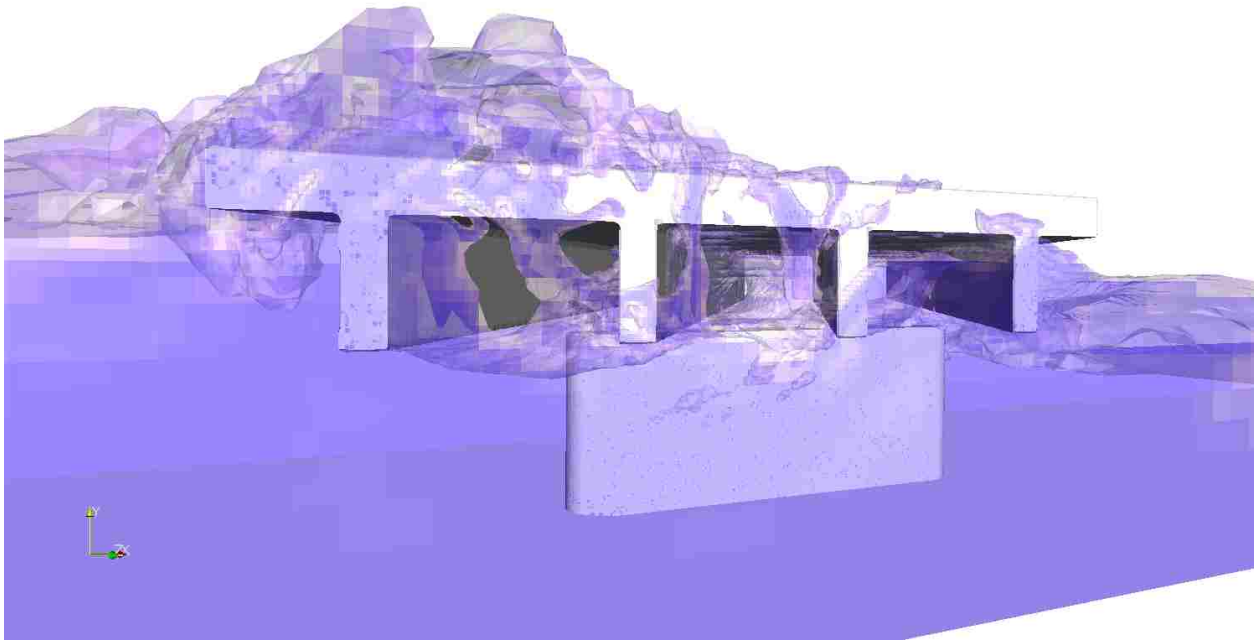

Figure 4.3: Rendered image of the 40° skewed bridge taken at 16 seconds showing the water flowing to the right-hand side.

bridges modeled here channels water to the left side of the flume, causing more water to overflow on the left side of the deck and creating a negative moment. As the flow slows down, water flows more evenly on top of the deck and M_X becomes negligible. Note that in reality, water channeled to one side of the bridge will not create significant moment like the flume test, because it is unlikely to have a wall that allows water to build up on a particular side of the bridge.

Another effect of skewness is the introduction of M_Y, also known as the spinning moment. M_Y causes the bridge to spin, i.e. rotate in the horizontal plane. An unskewed bridge does not spin, because the horizontal force acts symmetrically on the bridge. In a skewed bridge, the non-synchronous impact and forces in the direction perpendicular to the abutments spin the bridge. When the wave hits the bridge, only the right side of the bridge is under positive

F_X and F_Z; thus, the forces create a positive M_Y. When the resultant F_X acts on the left side of the bridge, it creates a negative M_Y. However, the negative moment is counteracted by increasing F_Z from full-contact of the flow and the skewed front face of the bridge, resulting in a positive M_Z. In steady-state, the flow evenly applies dynamic pressure in the direction of flow (this argument is supported by Figure 4.7 where F_X resisted by the left and right supports are the same in steady-state.) M_Y remains positive because of the positive F_Z acting on the front face of the bridge.

The effect of skewness on M_Z is the most obvious in steady-state. M_Z increases in a skewed bridge, because the distance between the front and back acute corners are further apart than in an unskewed bridge.

4.5.3 Horizontal Support Reactions

Structural engineers are often more interested in support reactions of a bridge rather than the load histories, because each support has a unique reaction due to the resultant moments according to the location of the support relative to the origin of summing moments.

Figure 4.5 shows the histories of the horizontal reactions at the four corner supports (BA, BO, FO and FA). The horizontal reactions are the magnitudes of the resultant reactions in the directions of flow and perpendicular to the abutments. Horizontal supports resist F_X, F_Z and M_Y (M_{SPIN}) only, because the vertical force (F_Y) and its corresponding moments (M_X and M_Z) are decoupled. The contributions of the loads to the reactions at supports are plotted in Figure 4.7 and Figure 4.8. F_X and F_Z are evenly distributed to the supports regardless of the skew angle. When the bridge is unskewed, the four supports resist the same amount of horizontal load, because there is no spinning moment (M_Y). In a skewed bridge, the spinning moment changes the reactions at each support.

The contribution of spinning moment to loads applied at supports in the direction of flow have the same magnitude, because each support has the same r_z to the origin of summing moments. The spinning moment in a skewed bridge reduces the reactions in all left supports (FO_X and BA_X) and increases the reactions in all right supports (FA_X and BO_X) in the

direction of flow.

This is not the case in supports in the direction of abutment. For low skew angles, spinning moment increases the reactions at the front supports in the direction of abutments (FA_Z and FO_Z) and decreases the reactions at the back supports (BA_Z and BO_Z). As the skew angles increases, FO_Z and BO_Z get closer to the origin of summing moments, reducing their effectiveness at resisting the spinning moments. For high skew angles, the front supports have different signs in r_x, which means the reactions from spinning moment now reduces for FO_Z and increases for BO_Z.

The maximum horizontal reactions from each case are normalized by the maximum horizontal reactions from the unskewed case and plotted against the skew angle in Figure 4.6. The results show a good correlation between horizontal reactions and skew angle, where the spinning moment effect amplifies as the skew angle increases. When the skew angle is increased to 40°, the horizontal reactions increases by about 25% at impact and 55% at steady-state.

4.5.4 Vertical Support Reactions

Figure 4.9 shows the histories of the vertical reactions at the four supports of interest. Since the horizontal and vertical forces are decoupled, vertical supports only resist F_Y, M_X (M_{PITCH}) and M_Z (M_{ROLL}), and their contributions to the reactions are plotted in Figure 4.11 and Figure 4.12.

F_Y is evenly distributed to the supports regardless of the skew angle. It decreases when the skew angle increases as described in section 4.5.1.

In an unskewed bridge, the loads are symmetric about the XY-plane but different along the direction of flow. Therefore, M_X is zero, whereas M_Z is not. The magnitude of contributions of M_Z to the reactions at all supports is the same. The moment increases reactions in the front supports and decreases in the back supports at impact

In a skewed bridge, the moment contributions are more complicated due to coupling of M_X and M_Z. This is because resistance of M_X inherently creates an additional M_Z to the

system, and vice versa. The effects are summarized in Figure 4.12. The M_Z in steady-state almost cancels out downward force applied by the weight of water at the front supports, which means the bridge is about to be overturned. Many girder bridges are installed by setting the girders onto a bearing pad with minimal or no tension reinforcement, which means they are very prone to M_X in steady state.

The maximum vertical reactions of each case are normalized in the same manner as the horizontal reactions and presented in Figure 4.10. Again, the figure shows that a highly skewed bridge has much less downward force applied to the front supports and can be overturned much more easily than an unskewed bridge.

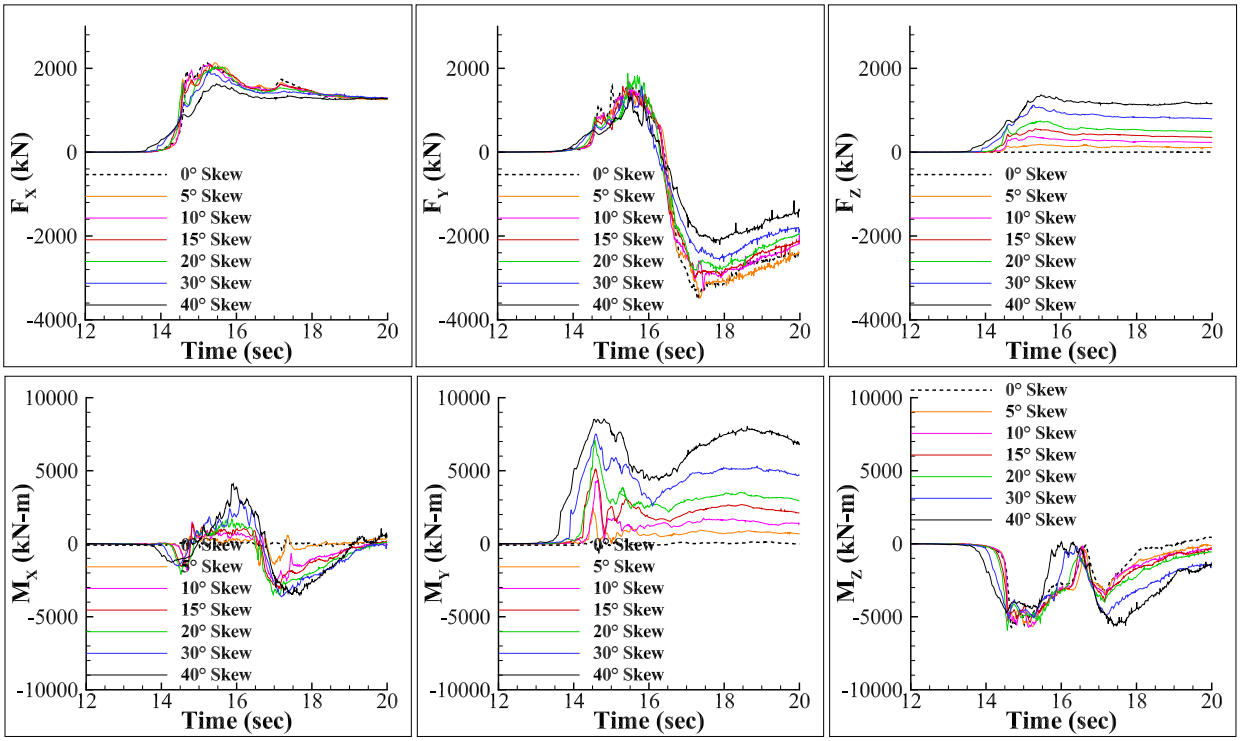

(a) All 7 cases including the unskewed one.

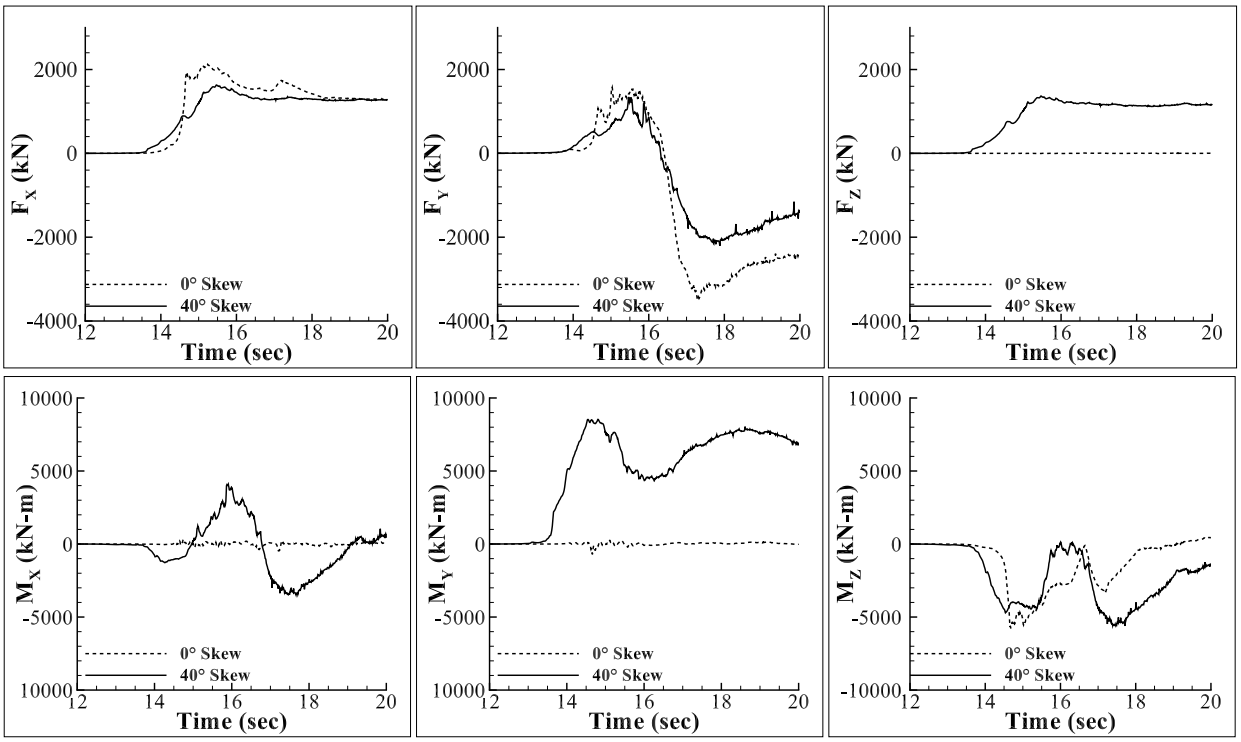

(b) 0° and 40° skew only.

Figure 4.4: Load histories of skewed bridges.

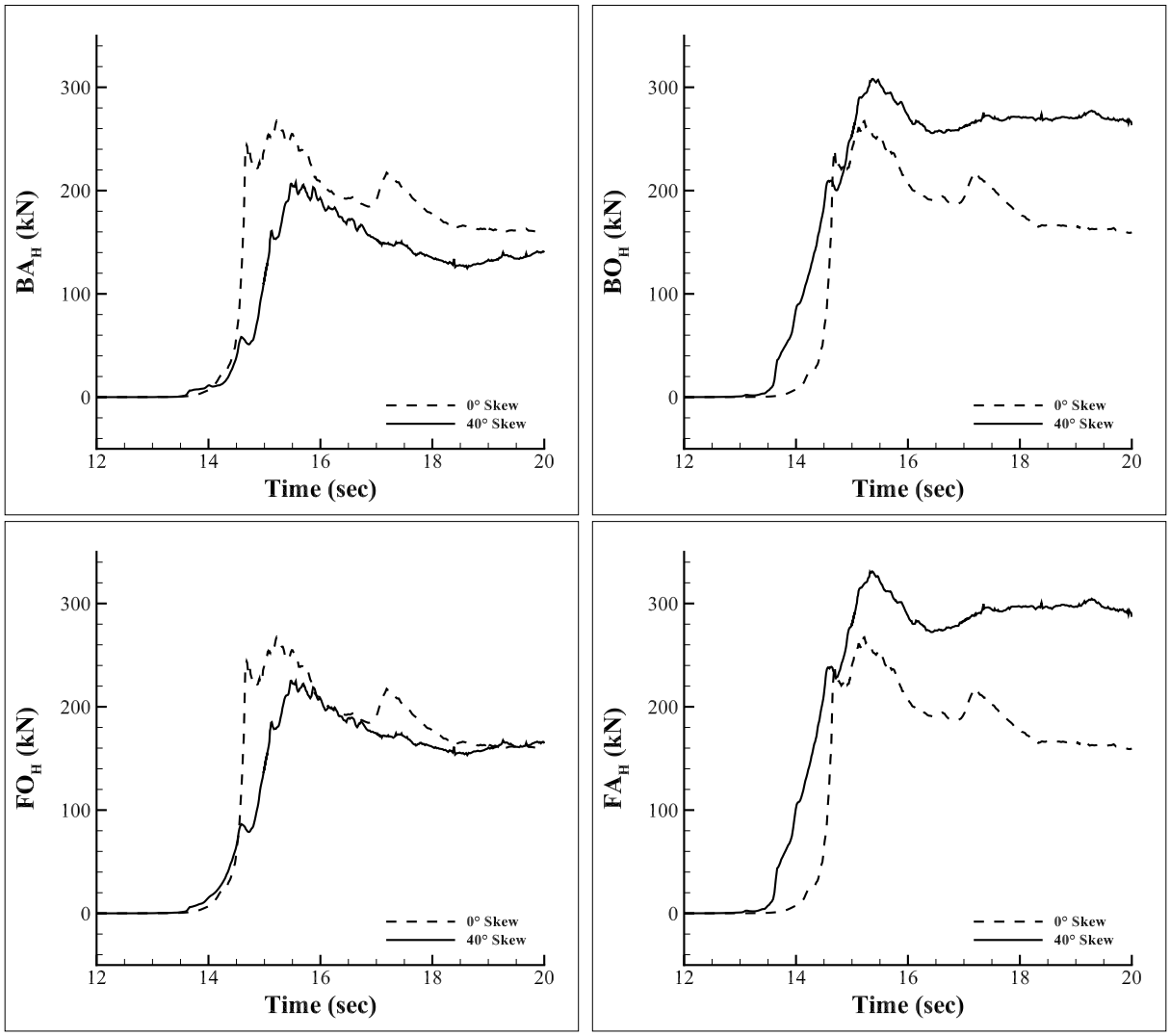

Figure 4.5: Histories of horizontal support reactions.

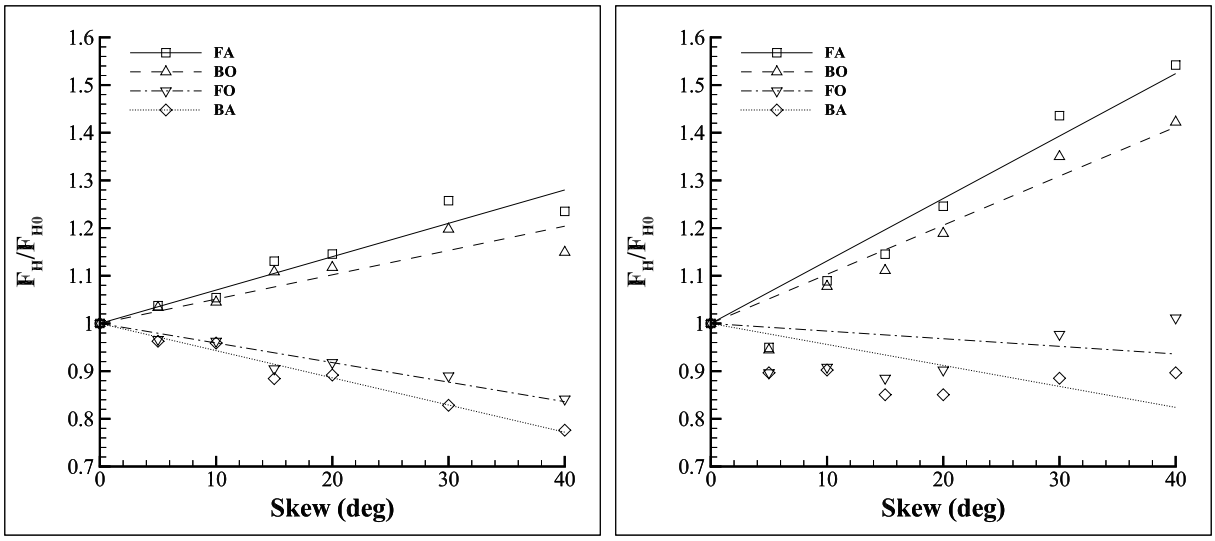

(a) Impact

(b) Steady-State

Figure 4.6: Normalized maximum horizontal support reactions as a function of skew angle.

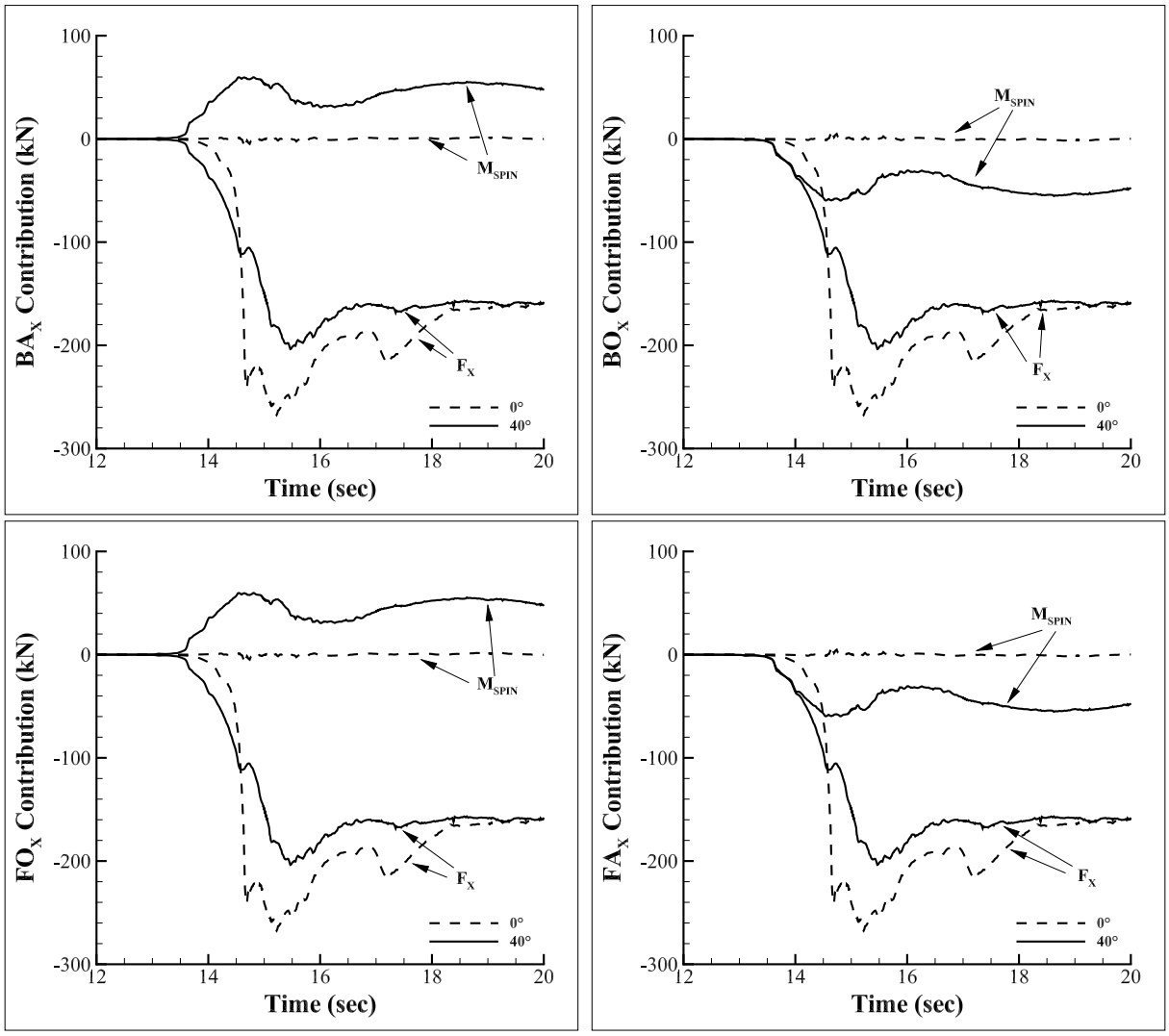

Figure 4.7: Contribution of horizontal forces and spinning moment in direction of flow for 0° and 40° configurations.

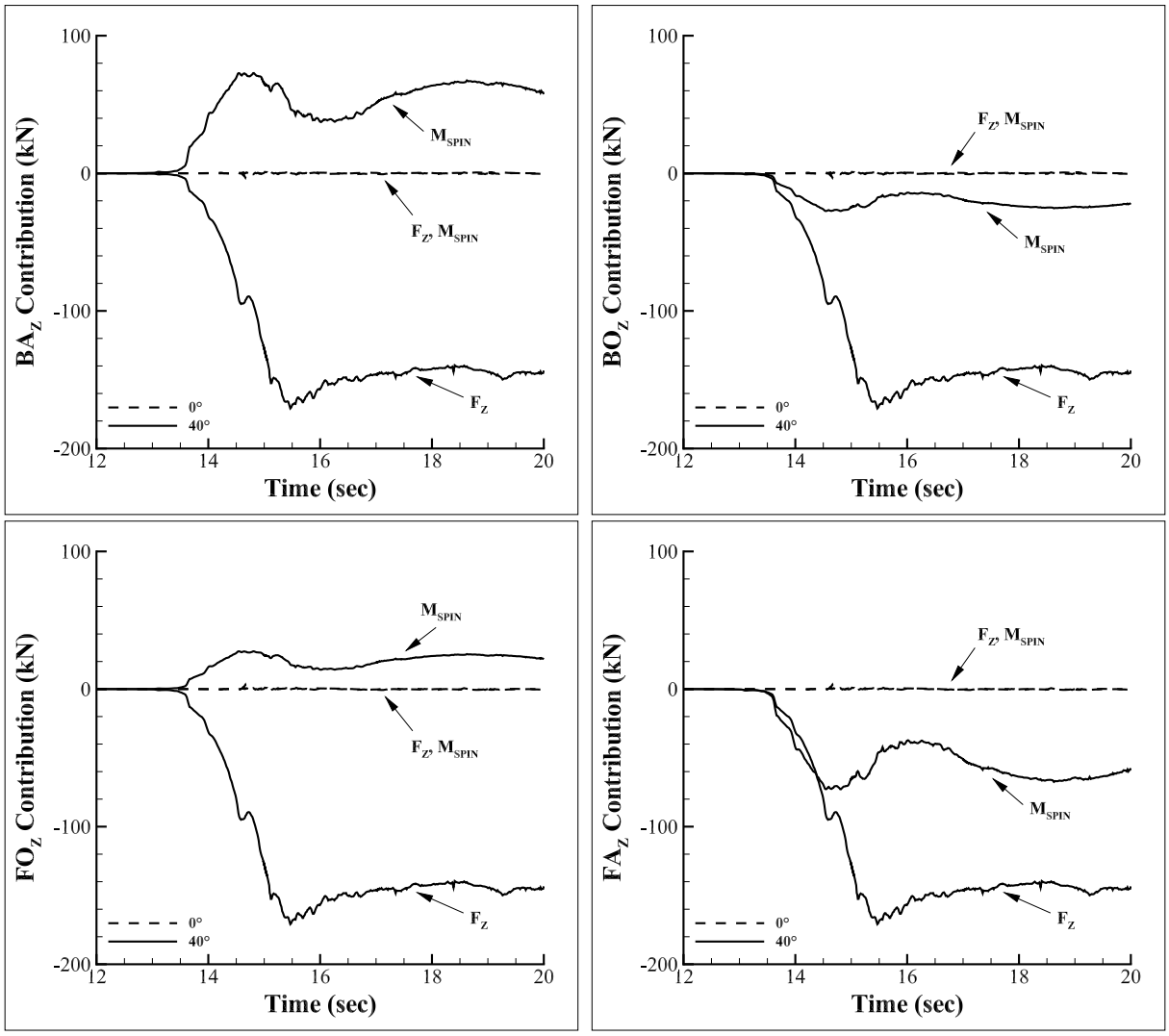

Figure 4.8: Contribution of horizontal forces and spinning moment perpendicular to abutments for 0° and 40° configurations.

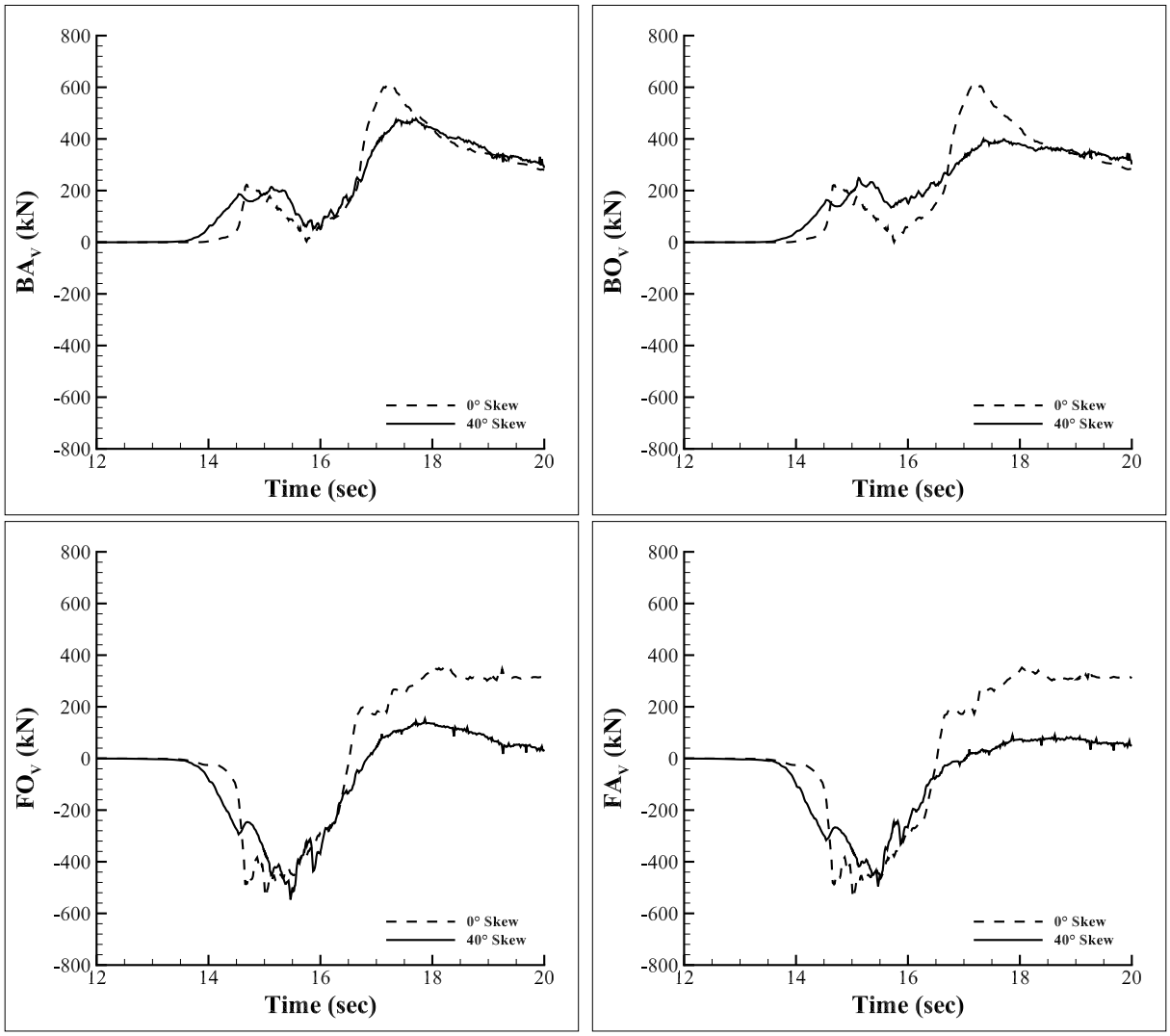

Figure 4.9: Histories of vertical support reactions.

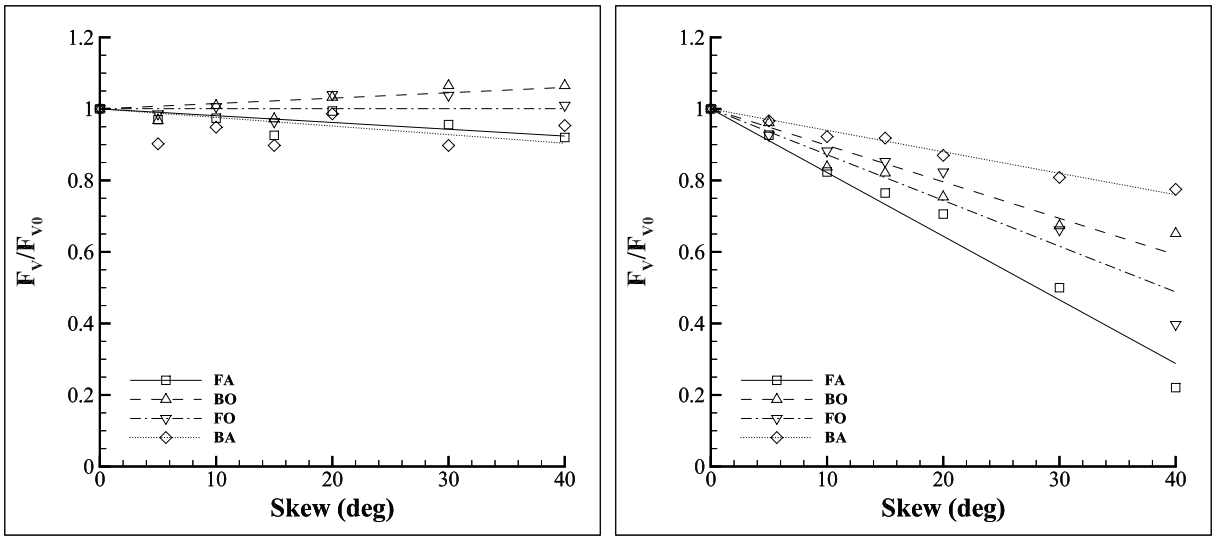

(a) Impact

(b) Steady-State

Figure 4.10: Normalized maximum vertical support reactions as a function of skew angle.

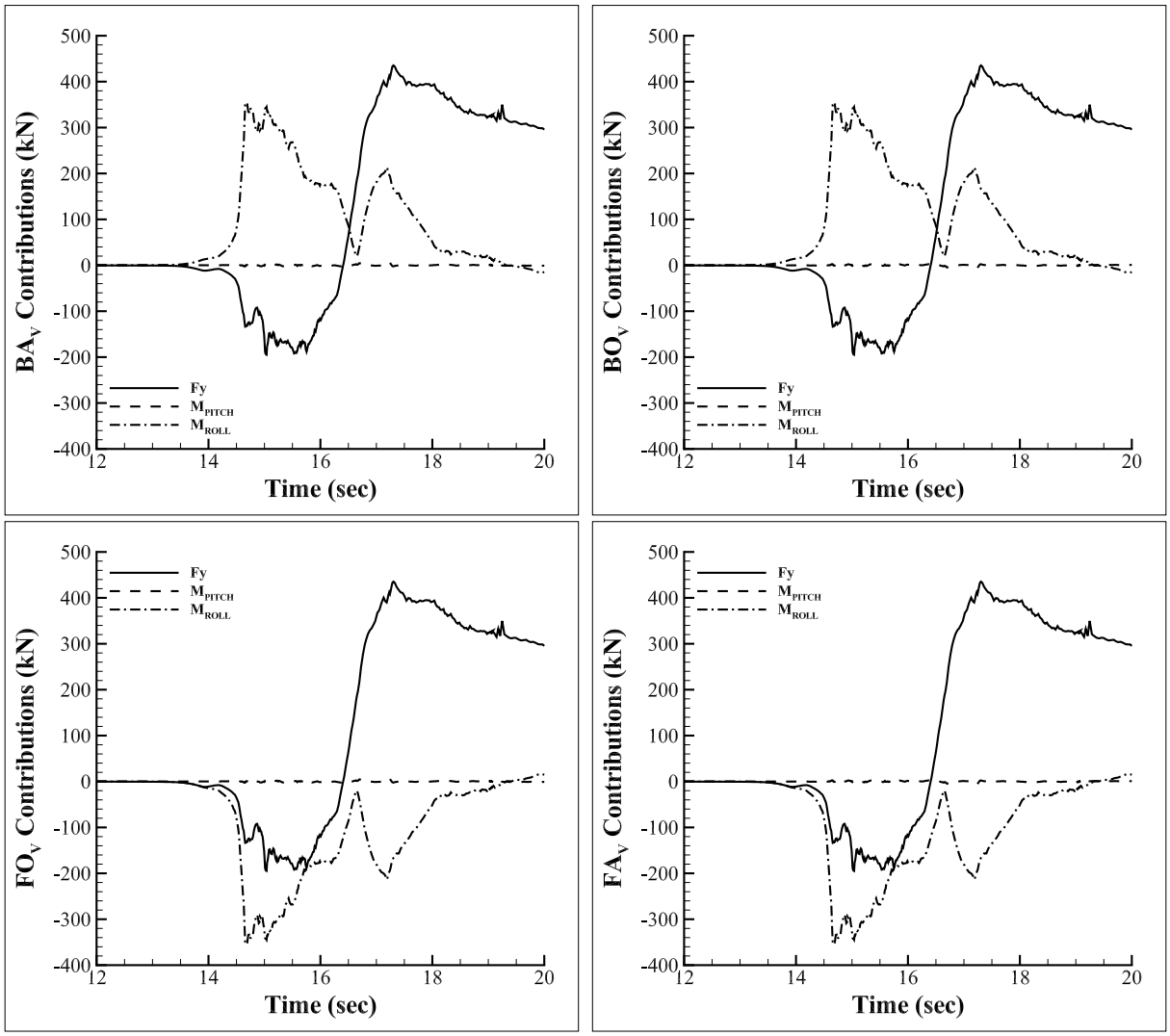

Figure 4.11: Contribution of uplift force and pitching and rolling moments to the vertical support reactions for the 0° configuration.

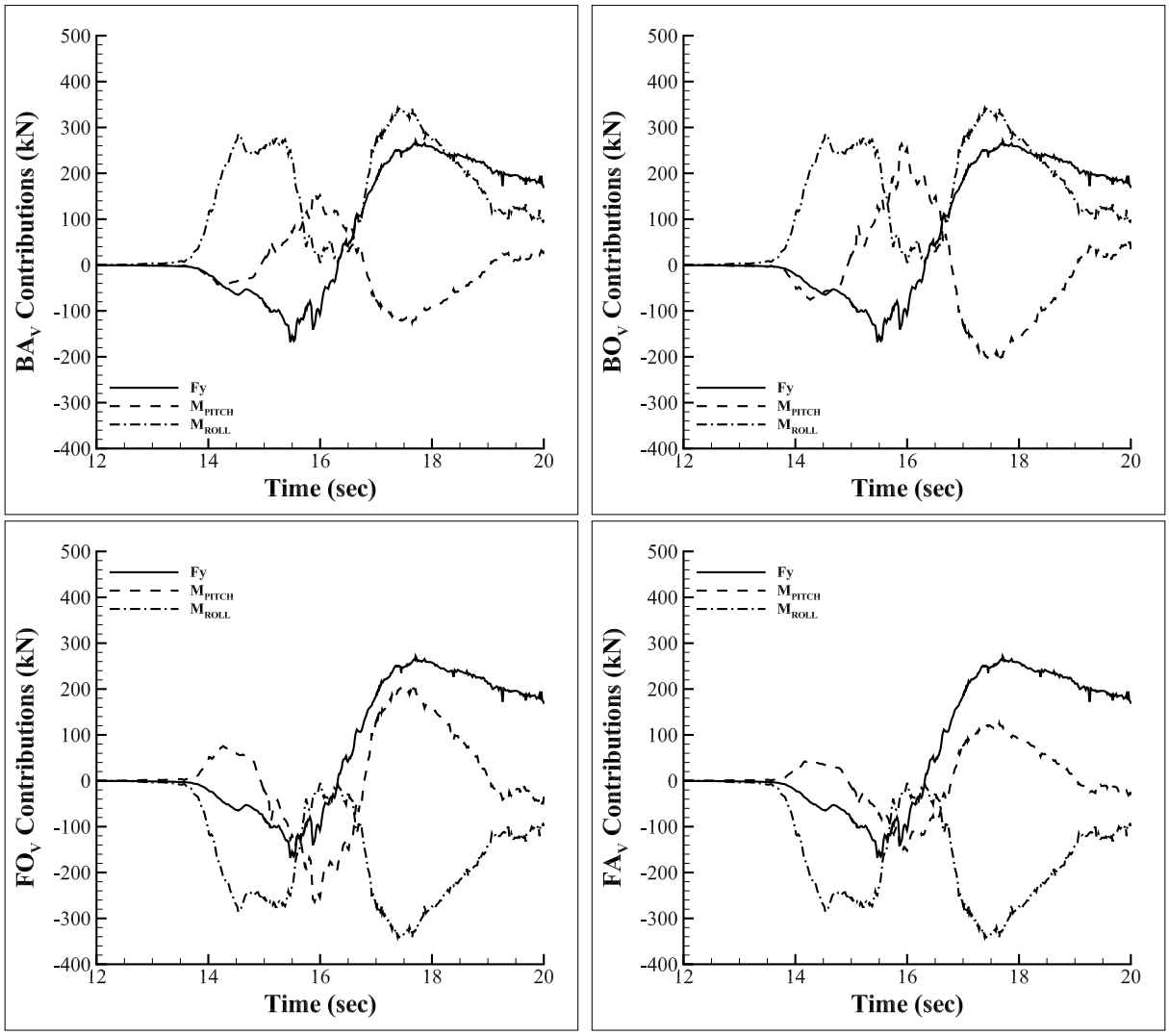

Figure 4.12: Contribution of uplift force and pitching and rolling moments to the vertical support reactions for the 40° configuration.

Chapter 5
SLOPED BRIDGES

Sloped or graded bridges are bridges whose abutments do not have the same elevation. The impact of a tsunami on a sloped bridge is different from its impact on an unsloped bridge for several reasons:

- Similar to skewed bridges, the sloped bridges have a longer superstructure than unsloped bridges, which increases the surface area over which the fluid loads act.
- The deck and girders are not unsloped, which means vertical loads will create horizontal components in support reactions.
- One side of the bridge is closer to the surface of the water, which results in asymmetric and asynchronized loads on the bridge that cause the bridge to spin and pitch in addition to rolling.

Two-dimensional models cannot represent the three-dimensional geometry of a bridge. Therefore, a series of three-dimensional models were developed to examine how changes in the slope of the bridge superstructure affect the support reactions.

5.1 Orientation of Bridge Decks

Bridge superstructures with a grades of 2%, 4%, 6% and 8% were modeled using the same flume shown in Figure 3.1 and the same initial water height described in Section 3.1 as the validation Case 2, so that results from the sloped cases could be compared with the unsloped experimental results. Negative grades were excluded from the parametric study, because they would give essentially the same results by symmetry. The sloped bridges were

created by rotating the four-girder bridge span about its geometric centroid while keeping the position of the geometric centroid unchanged with respect to the flume. The substructure was unchanged and remained parallel to the flow direction, as it would be in practice to reduce flow resistance.

The four corners of the deck are designated by their location (front or back of the bridge) and the relative elevation (high or low) at the deck corners. The front low and back low corners of the bridge superstructure are located on the right side of the flume, and the girder supports nearest to the corners are labelled as labelled as FL and BL, respectively. Similarly, the girder supports corresponding to the front high and back high corners are labelled FH and BH, and they are on the left side of the flume. The layout of the supports is presented in Figure 5.1.

5.2 Results

The results from the sloped bridge cases are presented here. Notations of the loads, decoupling of horizontal loads from vertical reactions and the method of calculating support reactions are explained in Sections 4.2, 4.3 and 4.4, respectively.

Similar to the unsloped bridge (Case 2), the time histories presented in Figure 5.2 show a rapid increase in forces and moments that correspond to the wave impact, followed by a decay of the loads to the steady-state flow regardless of the percentage of grade. The difference in the arrival time of the wave between the various cases considered was negligible, because the slopes were equivalent to relatively small angles of inclination. The change in elevations for the two abutments was not big enough to cause the wave to impact the lower side of the bridge significantly sooner than in the unsloped case. Hence, no time shift was necessary.

The trends of the load histories for the 5 sloped cases show a strong correlation between fluid forces and bridge slope. Since the intermediate slope cases follow the trend, the remaining discussion of slope effects focuses on the 0%, 4% and 8% cases for clarity in the plots.

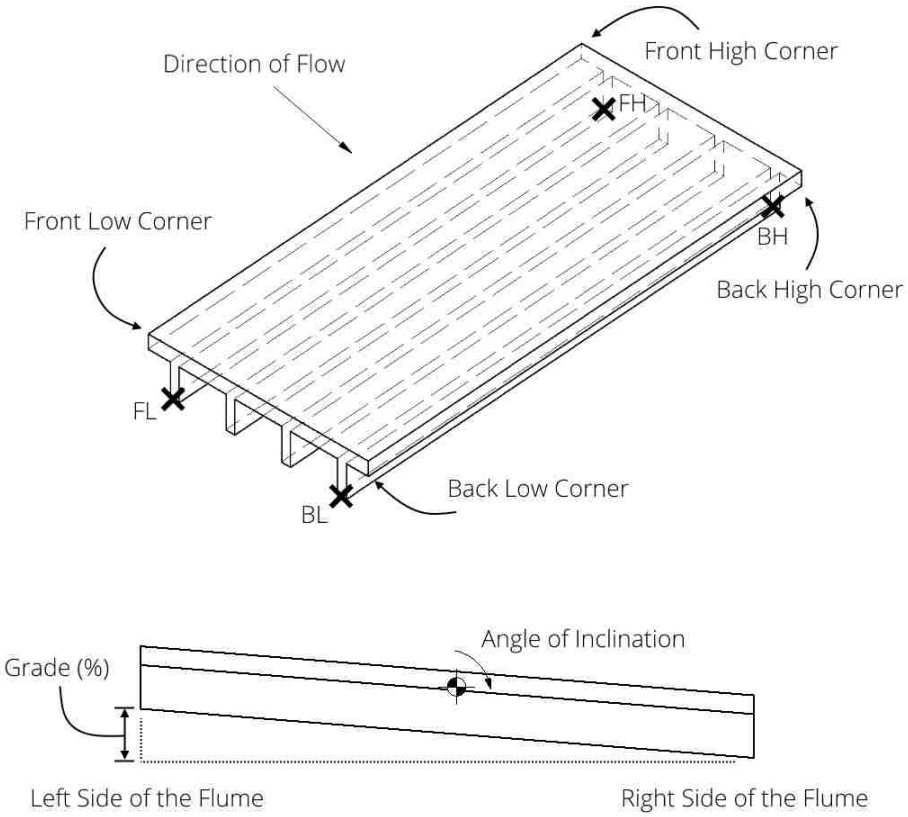

Figure 5.1: Schematic of a four-girder sloped bridge.

5.2.1 Resultant Forces

Overall, the force resultant histories for the sloped cases shown in Figure 5.2 closely resemble the experimentally validated model (Case 2). At 8% slope, the steepest bridge tested, the peak values of F_X and F_Y at impact match the ones from the validated model . This is because the sloped bridges, which had their front face perpendicular to the flow, were hit by the wave simultaneously. Immediately after the impact, not all of the surge piled up in front of the overhanging deck and crashed onto the bridge. Instead, the sloped bottom of the overhanging deck allowed some of the fluid to flow to the higher side of the deck, which relieved some of the pressures that would otherwise cause the wave to overtop at a greater

height.

In the subsequent steady-state flow, however, the forces decrease as the grade increases, because the sloped bottom diverts flows in the direction away from the right abutment and avoids concentration of hydrodynamic forces at the overhang and between the girders. During the impact, the upward vertical force from the oblique wave front applied a horizontal force to the right (positive Z-direction) of the sloped bottom of the bridge, resulting in a slight increase of F_Z with a positive value. The effect is most noticeable at about 16 to 18 seconds on the F_Y and F_Z histories when the magnitude of the vertical force decreases and the force in the abutment direction increases to a steady-state. Since the post-impact flow is caused by submergence of the bridge deck, it results in a negative F_Z because of the additional water overflowing on the right, lower portion of the bridge.

Because the front face of the bridge remains perpendicular to the flow regardless of the slope, water cannot flow into the voids between the girders as easily as in the skewed cases. Without the additional support of the water coming from the bottom of the superstructure, the vertical resultant force of the sloped cases during steady-state flow did not change from the unsloped case.

5.2.2 Resultant Moments

Moment histories change significantly for M_X and M_Y, but not as much for M_Z. For M_X, there is a negative peak at the beginning of impact which then reduces to zeros. That corresponds to the fact that the wave hit the lower end of the bridge superstructure first, lifting the right side up and creating a negative M_X. Approximately half a second later, the flow lifted the entire front end of the deck at once. Therefore, the resultant force was applied almost symmetrically about the mid-point of the front edge and resulted in a very small magnitude of M_X. At about 16.5 seconds, there is a large peak in positive M_X due to water overflowing the lower end of the deck. Eventually, the entire deck was submerged, and again M_X was small because of the more even loads. In steady-state flow, the sloped case sees an increase in positive M_X. As the grade increases, the magnitude of M_X that the bridge

experienced becomes larger. This is because, when the flow slows down, the depth of water dropped and water tended to flow to the lower end of the bridge, creating an unbalanced gravity load.

The sloped cases had positive M_Y throughout the analyses, because the lower end was subjected to more fluid loads, especially at impact and immediately after. Spinning moment is created by forces in the horizontal directions. When the bridge is not sloped, the four supports resist the same amount of horizontal load, because there is no spinning moment (M_Y). In a sloped bridge, the flow pushes harder on the lower side, because the lower part is closer to the flow and subjected to a stronger wave impact. In the steady-state flow, the entire bridge is submerged to the flow. Since the flow is acting on the whole superstructure more evenly, the magnitude of the spinning moment is much lower.

Changes in M_Z were much smaller compared to those in F_Y when the slope of the bridge increases. Most noticeably, the rolling moment is less at impact, because the uplift force is diverted to horizontal forces. Other than that, the sloped cases qualitatively had the same M_Z as the unsloped case.

5.2.3 Horizontal Support Reactions

Figure 5.3 shows the histories of the horizontal reactions at the four corner supports (FL, BL, FH and BH). The horizontal reactions are the magnitudes of the resultant reactions in the directions of the flow and the abutment. Horizontal supports resist F_X, F_Z and M_Y (M_{SPIN}) only, because the vertical force (F_Y) and its corresponding moments (M_X and M_Z) are decoupled. The contributions of the loads to the demand at supports are plotted in Figure 5.5 and Figure 5.6. F_X and F_Z are evenly distributed to the supports regardless of the slope.

The changes in support reactions in the direction of flow (X-direction) are mostly due to the spinning moment. From Figure 5.5, F_X does not change much when the slope increases from 0% to 8%. However, M_{SPIN} increased the maximum reactions by 20% on the lower supports (FL_X and BL_X) and reduced those on the higher supports (FH_X and BH_X) by

the same amount.

Support reactions in the abutment direction are affected by the force in the abutment direction (F_Z) and moments in all three directions (M_X, M_Y and M_Z). In the unsloped bridge, the support reactions in the abutment direction are zero, because loads are symmetric about the XY-plane. In 8% slope bridges, the support reactions are non-negligible as seen in Figure 5.6. F_Z forces (presented in Figure 5.2) are evenly distributed to all four supports. At impact, both the spinning moment (M_Y) and rolling moment (M_Z) amplify the reactions, while the pitching moment M_Z has much less influence on the support reactions. The small elevation difference in the abutments means the supports in the abutment direction are ineffective at resisting M_Z, because the lever arm of the moment couple is short.

The maximum horizontal reactions from each case are normalized by the maximum horizontal reactions from the unsloped case and plotted against the percentage of slope in Figure 5.4. The results show a good correlation of horizontal reactions as a function of slope. At 8% slope, the maximum forces are increased by approximately 15% at impact and approximately 10% in the steady-state.

5.2.4 Vertical Support Reactions

Figure 5.7 shows the histories of the vertical reactions at the four supports of interest. Since the horizontal and vertical forces are decoupled, vertical supports only resist F_Y, M_X and M_Z, and their contributions to the demands are plotted in Figure 5.9 and Figure 5.10.

F_Y is evenly distributed to the supports regardless of the slope. The effects of slope on F_Y are described in Section 5.2.1.

In an unsloped bridge, the loads are symmetric about the XY-plane but different along the direction of flow. Therefore, M_X is zero whereas M_Z is not in Figure 5.9. The magnitude of contributions of M_Z to the reactions at all supports is the same.

In a sloped bridge, M_Y is coupled with M_X and M_Z inherently; however, the effect is not obvious in the sloped cases because of the small elevation change in the supports. When M_Y is applied and resisted by the horizontal supports, which are at different elevations,

the reactions create M_X and M_Z that need to be resisted by vertical reactions. Since the difference in elevation is small, the resultant M_X and M_Z are small too, which has negligible effects on the vertical support reactions. Therefore, the M_Y contributions are excluded from Figure 5.9 and Figure 5.10 for brevity.

The vertical support reactions are lower when the bridge is steeper, because the sloped bottom relieves stress from the uprising flow by diverting the flow horizontally towards the left abutment. When comparing the vertical support reactions for the 0% slope (Figure 5.9) and the 8% slope (Figure 5.10), the M_Z at about 17 second is essentially eliminated. This is because water does not crash on the deck in the 8% case; rather, the flow is gradually rising and eventually overtops the deck. The slope also introduces M_X, which has insignificant magnitudes compared to F_Y and M_Z.

The maximum vertical reactions for each case are normalized in the same manner as in the horizontal reactions and presented in Figure 5.8. It appears that BH_V is the only support that has reduction in reactions when the slope increases. However, the maximum BH_V of the unsloped case is low already as seen in Figure 5.7. Subsequently, any changes in the vertical reaction would result in a significant decrease in the normalized plot. Taking that into account, it was concluded that the change in slope would not effectively change the vertical support reactions at impact. On the other hand, a good correlation was observed in the steady-state flow, where the vertical support reactions decrease as the slope of the bridge increases.

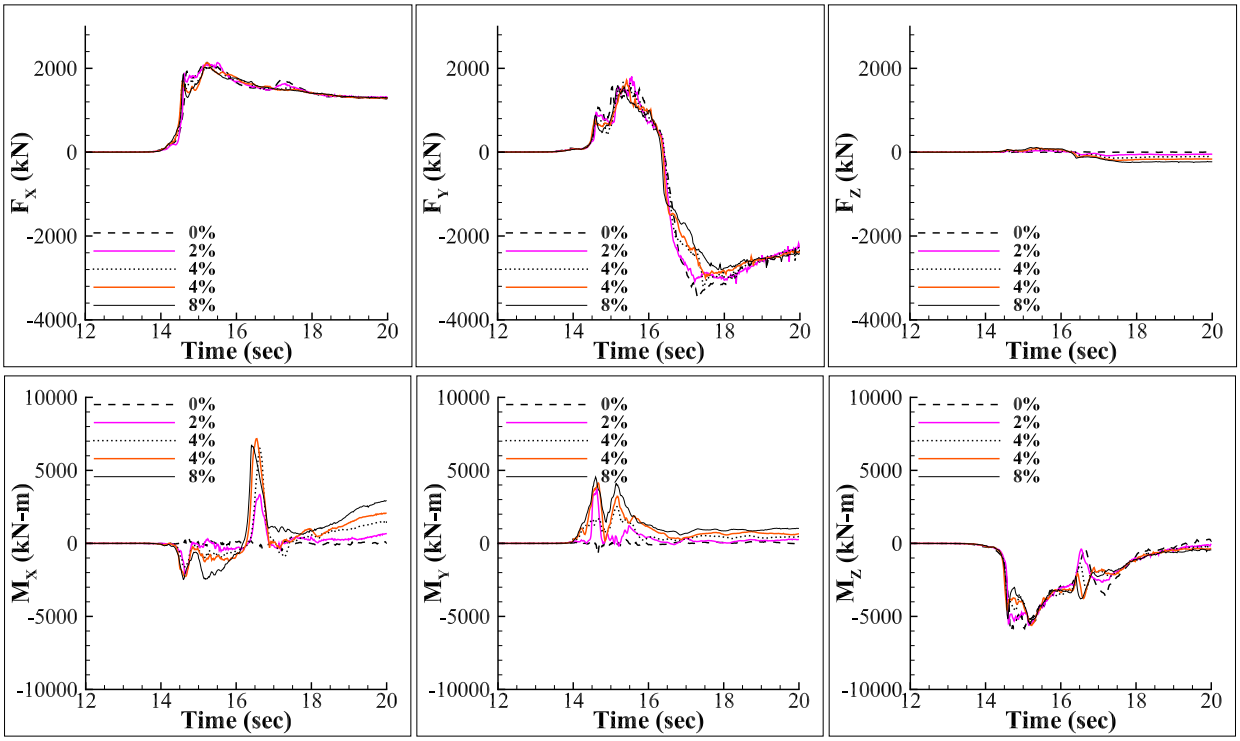

(a) All 5 cases considered, including the unsloped one.

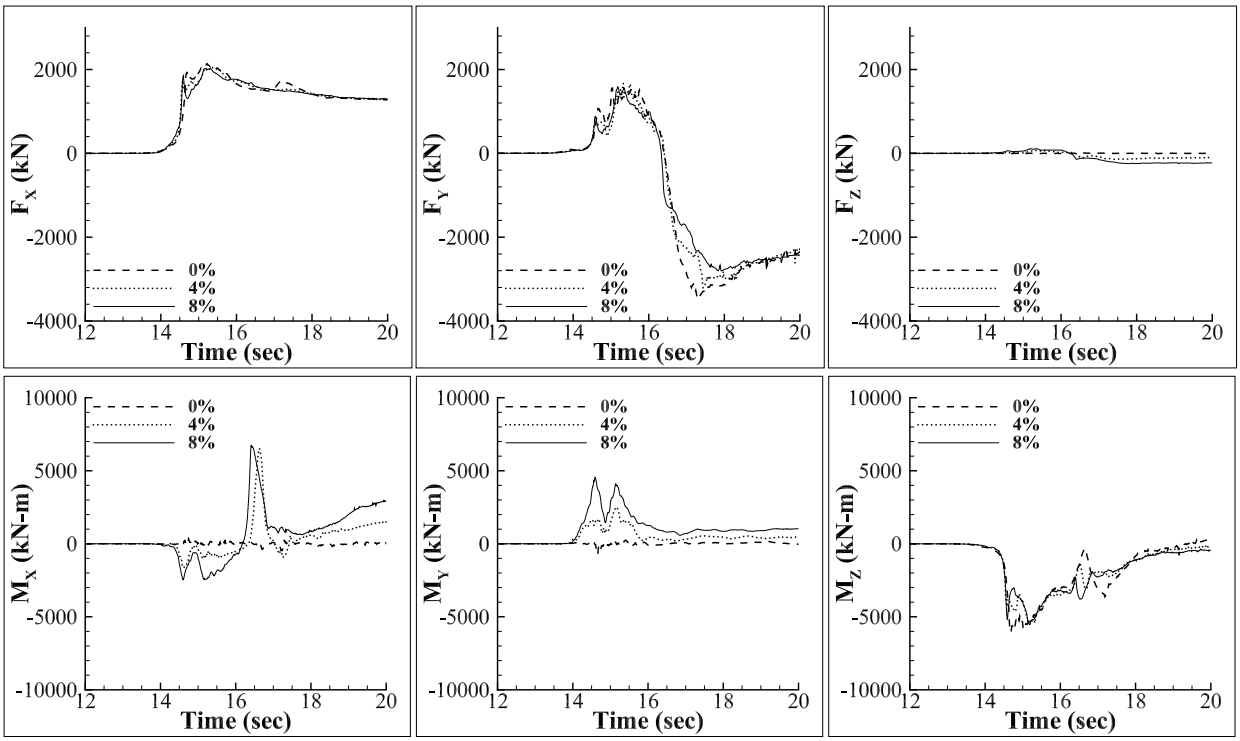

(b) 0%, 4% and 8% cases only.

Figure 5.2: Load histories for sloped bridges.

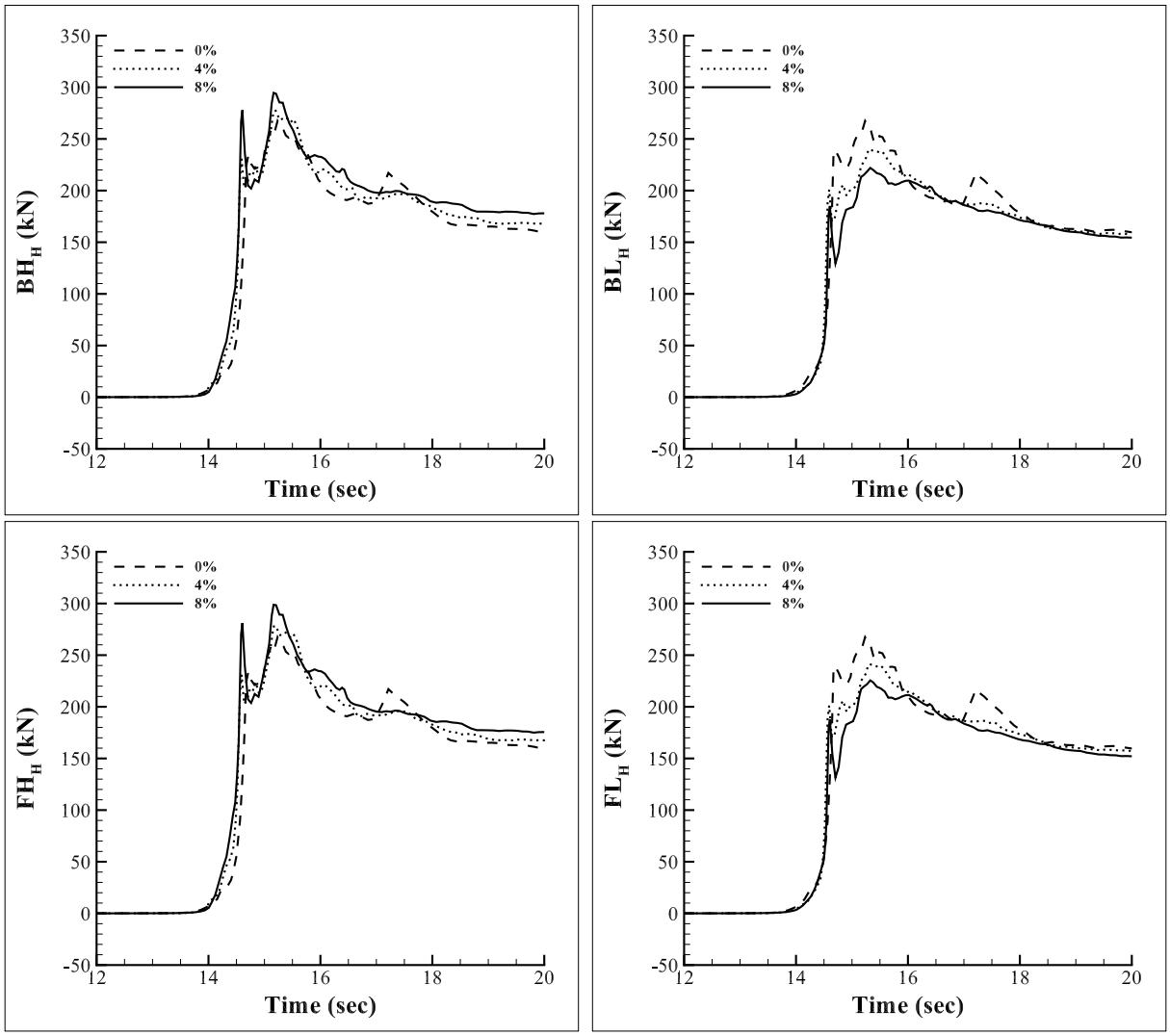

Figure 5.3: Histories of horizontal support reactions.

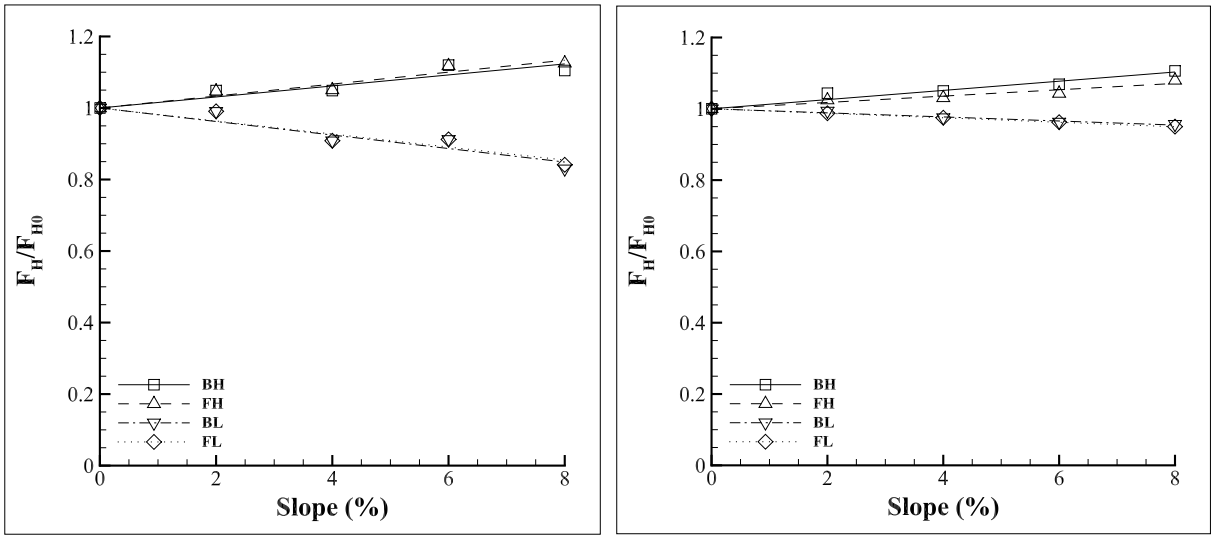

(a) Impact (b) Post-Impact

Figure 5.4: Normalized maximum horizontal support reactions as a function of slope gradient.

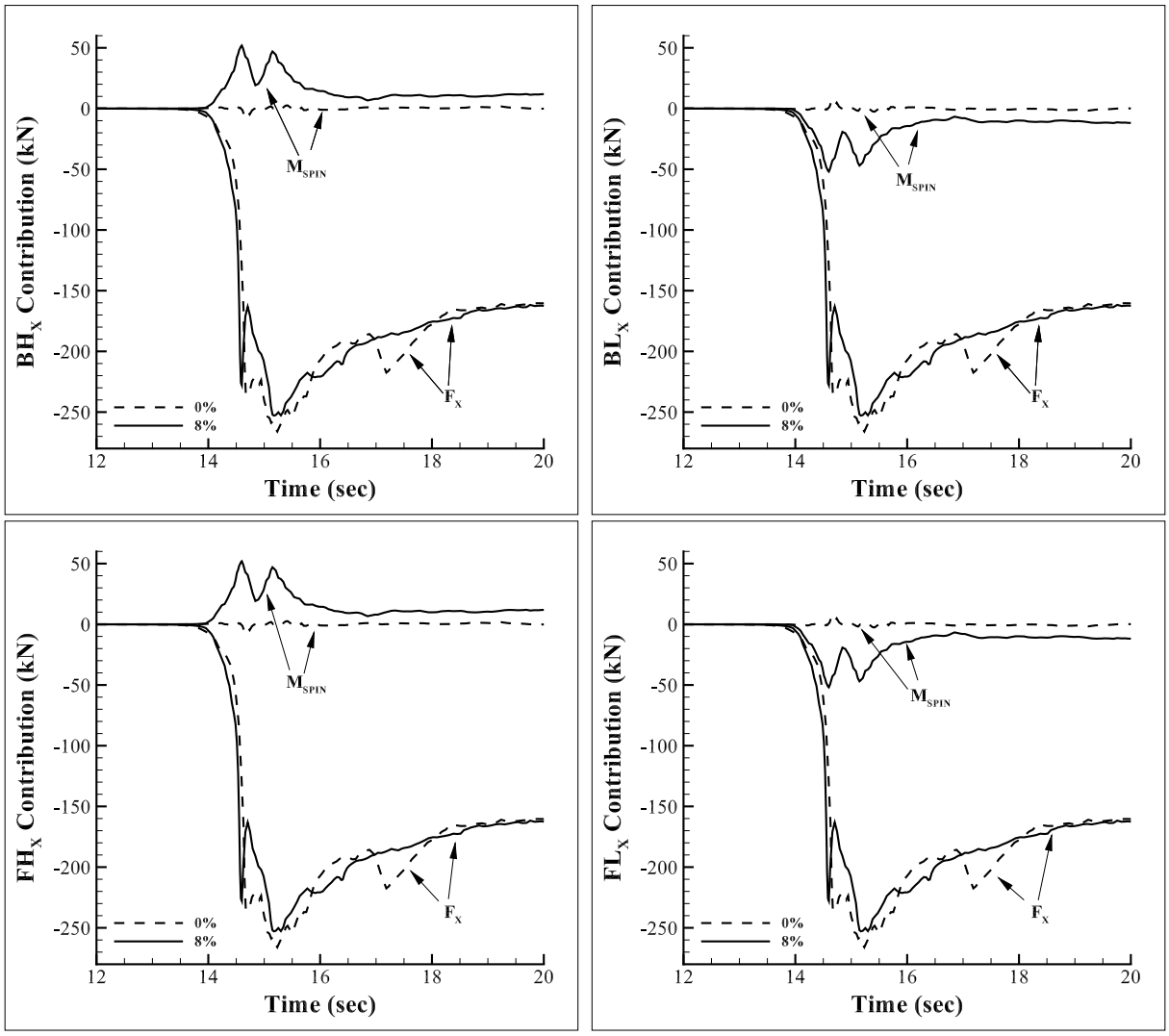

Figure 5.5: Contribution of horizontal force and spinning moment in direction of flow for 0% and 8% slope configurations.

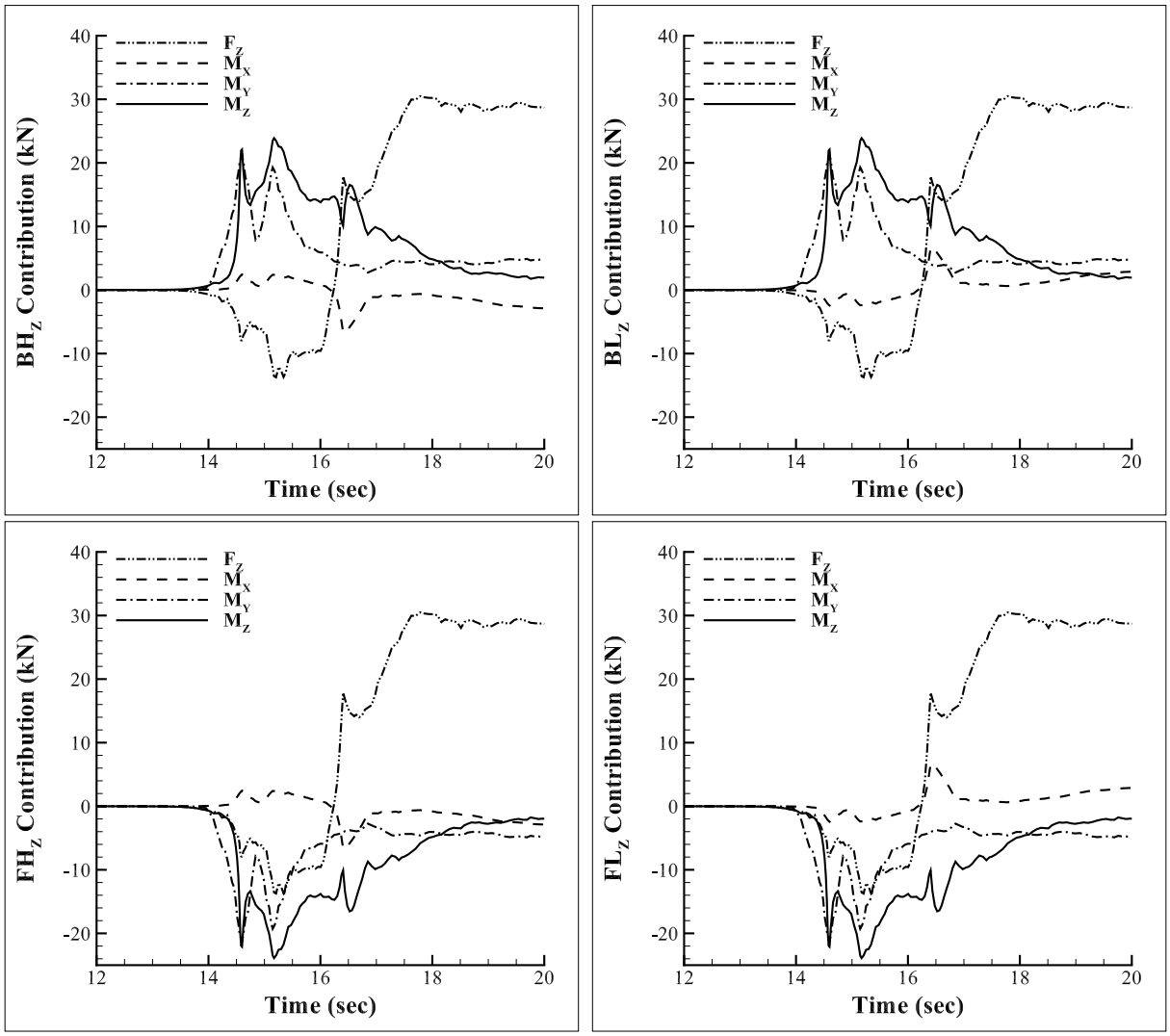

Figure 5.6: Contribution of horizontal force and spinning moment perpendicular to abutments for 8% slope configuration.

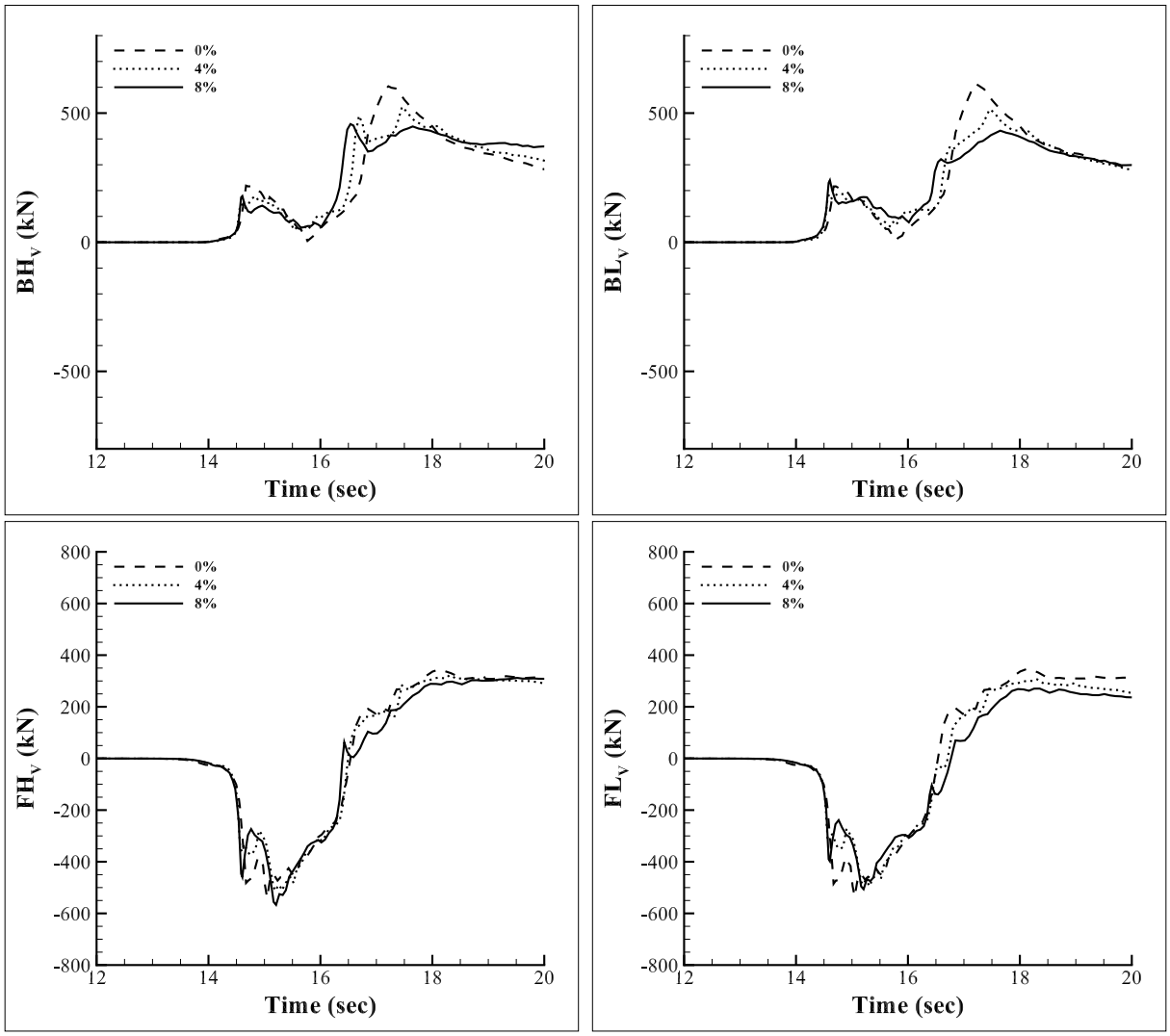

Figure 5.7: Histories of vertical support reactions.

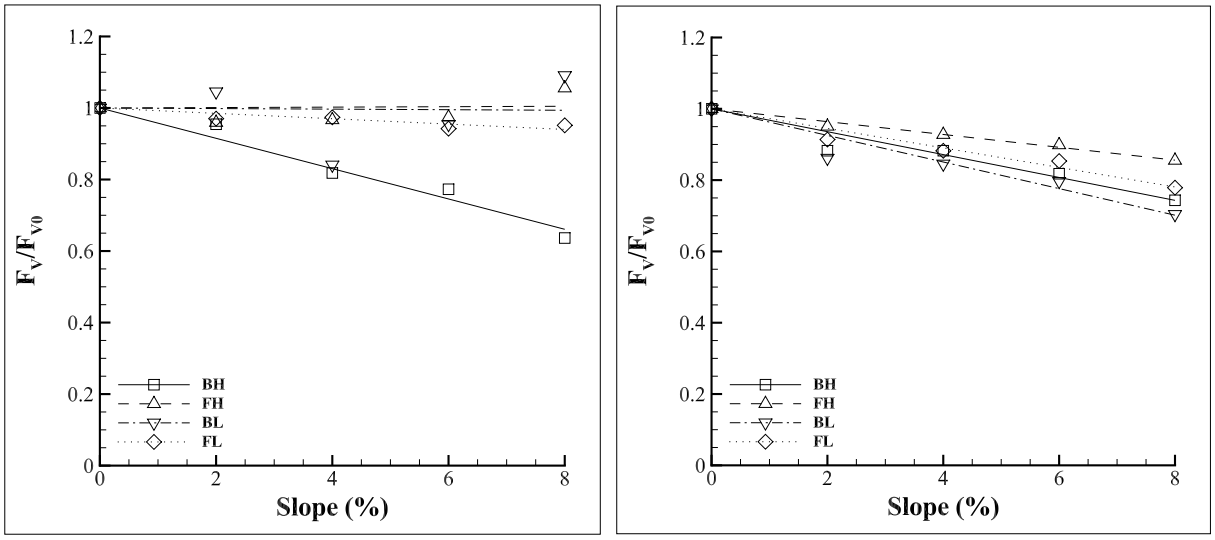

(a) Impact

(b) Post-Impact

Figure 5.8: Normalized maximum vertical support reactions as a function of slope.

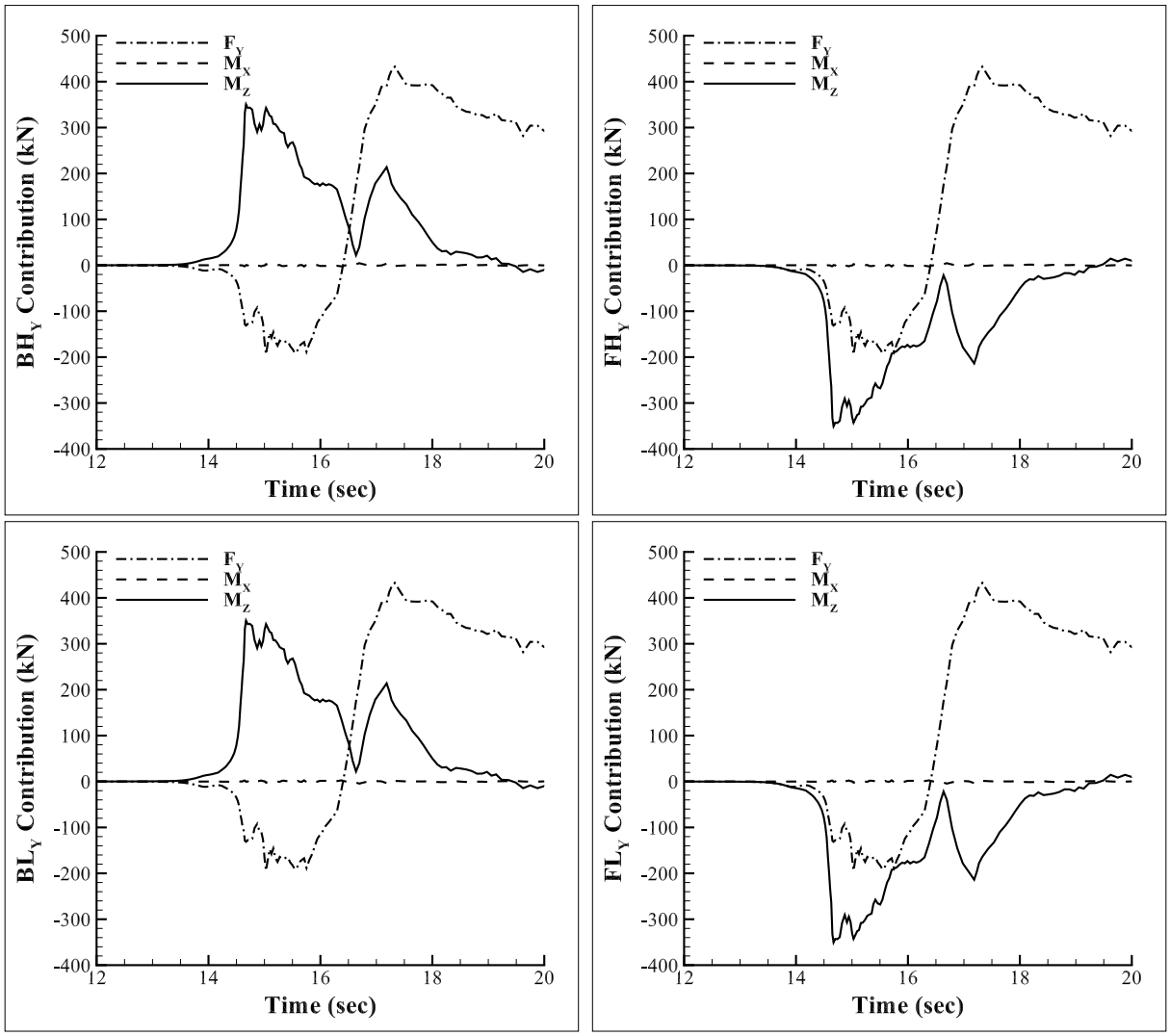

Figure 5.9: Contribution of uplift force and pitching and rolling moments to the vertical support reactions for the 0% slope configuration.

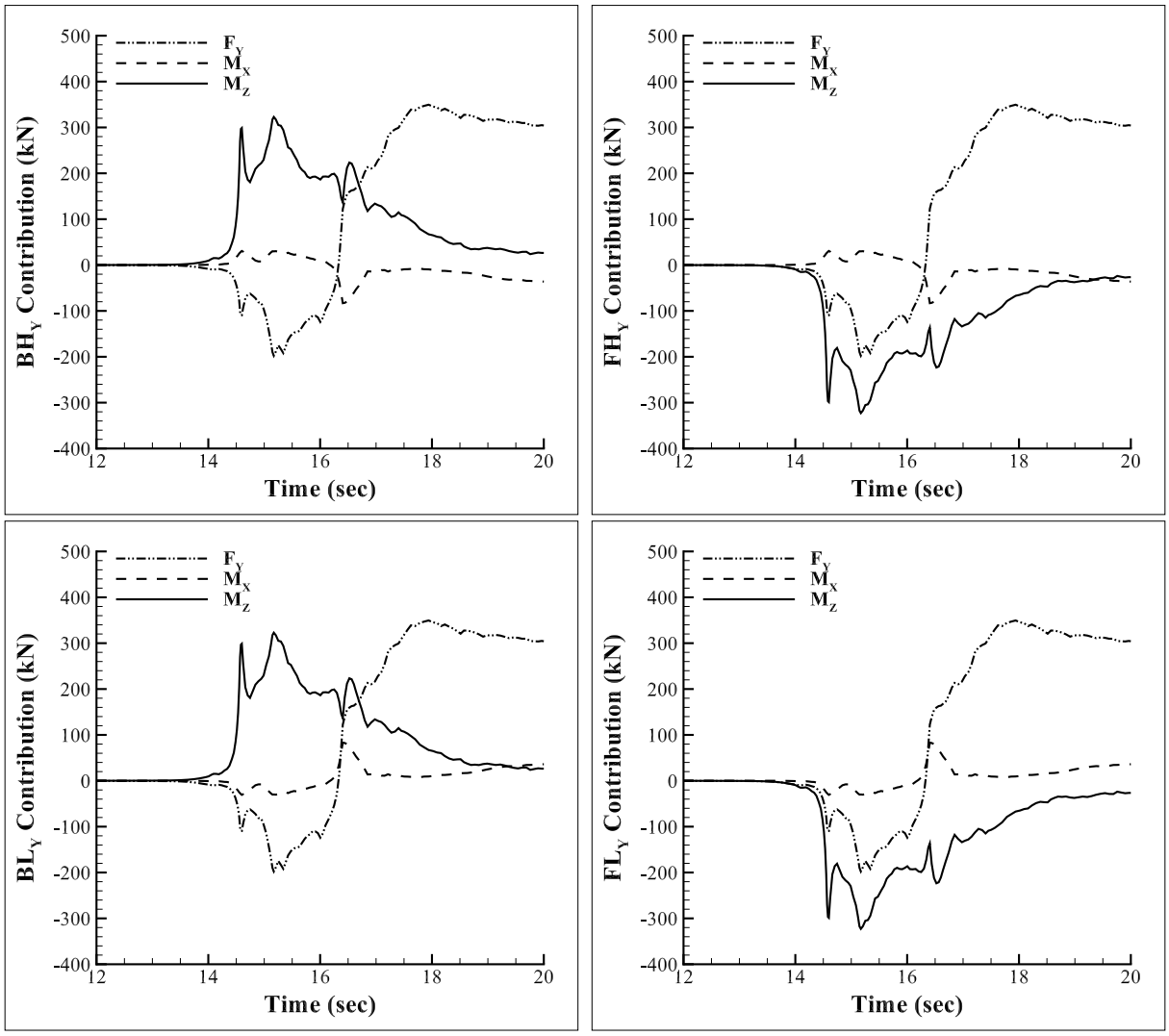

Figure 5.10: Contribution of uplift force and pitching and rolling moments to the vertical support reactions for the 8% slope configuration.

Chapter 6
SUPERELEVATED BRIDGES

Superelevated bridges are bridges for which the surface is banked through a horizontal curve. Superelevation can be measured as the angle between the bridge deck and a horizontal plane, and is designed to provide centripetal force to vehicles while they turn at the designated speed of the roadway. Bridges are often superelevated as part of a horizontal curve or an approach to a curve. The impact of a tsunami of a superelevated bridge is different from its impact on a bridge with no superelevation, because the bridge profile has changed:

- If a bridge is superelevated such that the deck is facing towards the incoming flow, the flow will exert more downward force to stabilize the superstructure and help prevent it from being carried away by the flow. The effect is similar to spoilers in an automobile which exert downward force to reduce the likelihood of skidding.

- On the other hand, a bridge superelevated such that the bottom of the superstructure is facing towards the incoming flow will experience more uplift from the flow, increasing the risk of being displaced. The added pressure to the superstructure's bottom face creates lift, because the flow above the structure is open to air and applies less resistance to uplift of the superstructure.

While the superstructure with only superelevation (i.e., no skew, slope or curve) can be represented in two-dimensions, three-dimensional models provide more accurate approximations to the force predictions as demonstrated in Section 3.6, because they account for factors such as three-dimensional geometry, turbulence and the substructure. Therefore, a series of three-dimensional models were developed to examine how superelevation in both directions would change the support reactions.

6.1 Orientation of Bridge Decks

Bridge superstructures with superelevations of ±2.5°, ±5°, ±7.5° and ±10° were modeled using the same flume shown in Figure 3.1 and the initial water height described in Section 3.1 as the validation Case 2, so that results from the superelevation cases could be compared with the validated case. The superelevated bridges were created by rotating the four-girder bridge span about its geometric centroid while keeping the position of the geometric centroid unchanged with respect to the flume. The substructure was unchanged and remained parallel to the flow direction, as it would be in practice to reduce flow resistance.

The four corners of the deck are designated by their location (front or back and left or right of the bridge). The nearest girder supports to the front-left, back-left, front-right and back-right corners of the bridge superstructure were designated as FL, BL, FR, and BR, respectively. The layout of the supports is presented in Figure 6.1.

For the purpose of this work, the superelevation of the superstructure was modeled as uniformly applied to the full span of the straight bridge. In reality, superelevation gradually changes as the roadway approaches and passes through a horizontal curve. In the analyses, the transition of superelevation and the horizontal curve were not included in the model, because they would introduce too many parameters and make identifying the cause of changes in the results impractical. In this parametric study, superelevation was chosen to be the parameter of interest. The transition of superelevation and horizontal curve can be modeled easily by changing the CAD model of the bridge superstructure, but they are outside of the scope of this work.

Despite the fact that three-dimensional effects of the model created non-uniform loads across the bridge, the loads were symmetric about the model's XY-plane. Therefore, the left supports had the same reactions as their corresponding supports on the right. For simplicity, the discussion in this chapter focuses on the left supports (FL and BL) only, and the same conclusions can be applied to the right supports.

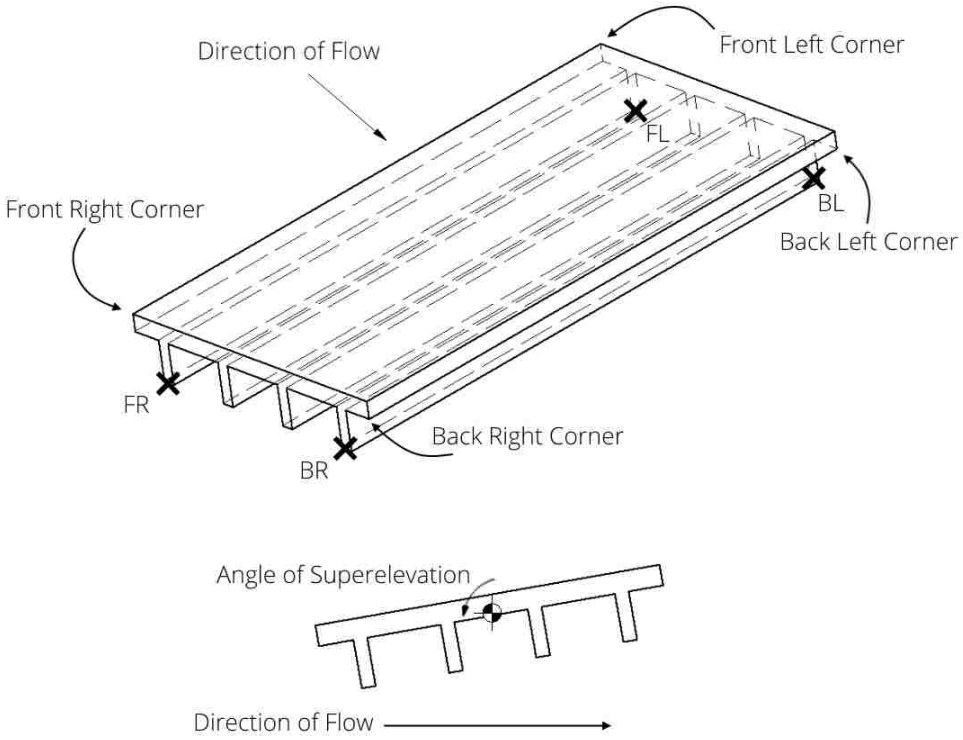

Figure 6.1: Schematic of a four-girder superelevated bridge.

6.2 Results

The results from the superelevated cases are presented in this section. Notations of the loads, decoupling of horizontal loads from vertical reactions and the method of calculating support reactions are explained in Sections 4.2, 4.3 and 4.4, respectively.

Similar to the bridge with no superelevation (Case 2), the time histories presented in Figure 6.2 show a rapid increase in forces and moments that correspond to the wave impact, followed by a decay of the loads to the steady-state condition regardless of the superelevation angles. In the F_Y histories, there is a noticeable time difference in wave impacts. Bridges with a negative angle of superelevation have a delayed impact compared to the bridge with no

superelevation; in contrast, the wave impacts bridges with a positive angle of superelevation sooner than the bridge with no superelevation. This is because a negative and a positive angle of superelevation bring the front end of the bridge superstructure higher and lower, respectively. The higher the front end is from the free surface of the flow, the later the wave would hit it. It was assumed that the wave was fully developed when it hit the bridge in all cases. No time shift was applied to the data to preserve the variations due to superelevation effects.

The trend of the load histories of the 9 superelevated cases shows a strong correlation with the superelevation angle. Since the intermediate angle cases follow the trend, the remaining discussion of superelevation effects focuses on the 0°, ±5°, and ±10° for clarity on the figures.

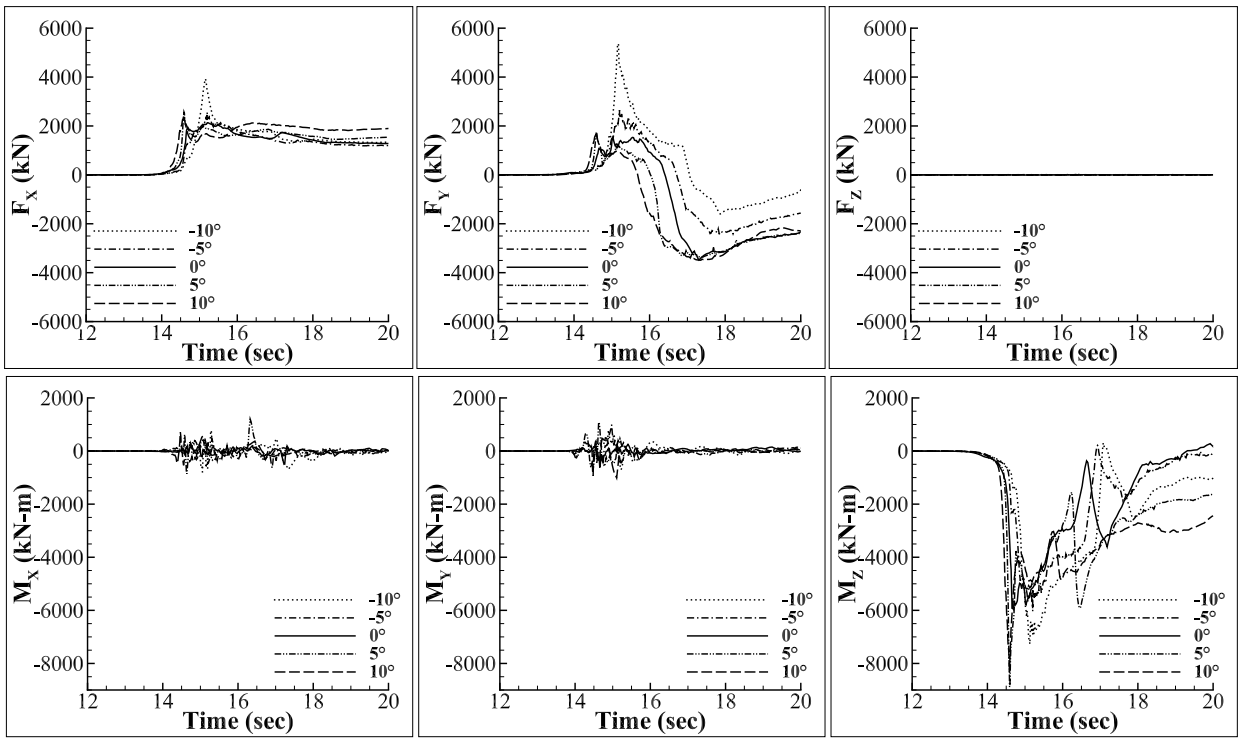

Figure 6.2: Load histories of superelevated bridges.

6.2.1 Resultant Forces

The resultant forces are presented in Figure 6.2. First of all, F_Z is zero regardless of the superelevation angle, which validates that the assumption of loads being symmetric about the XY-plane is valid.

The horizontal force (F_X) at impact increases when the superelevation was introduced in either a positive or negative angle, because the superelevation in both directions increases the effective area. The effective area is defined as the area of the bridge superstructure projected onto a XZ-plane, which is the actual area obstructing the horizontal flow. With a larger effective area, the flow would apply more horizontal pressure to the superstructure. In the $-10°$ case, the superelevation angle was high enough that the voids between the girders were exposed to the wave impact, allowing the flow to apply pressure to the bottom face of the deck, and therefore increased the impact force greatly.

F_X in the subsequent flow increased only in the cases with a positive superelevation angle because of how the weight of water acted on the bridge deck. Regardless of the direction of superelevation, the effective area increased and so did the horizontal force. In the bridges with a positive superelevation, the weight of water induced a positive F_X because of how the superstructure was oriented. On the other hand, the weight of water exerted a negative F_X force on the bridges with a negative superelevation and counteracted the increase in force due to the larger effective area. As a result, the bridges with a negative superelevation had about the same F_X in the steady-state flow as the F_X in Case 2.

The vertical force (F_Y) at impact increased when the superelevation angle was negative and decreased when the superelevation angle was positive because of the change in the behavior of the fluid load. Bridges with a negative superelevation angle had their bottom face aim more toward the flow than the bridge with no superelevation, which caused the horizontal flow to apply a vertical load upward, amplifying the magnitude of impact. In the $-10°$ case in particular, the flow that got into the voids between the girders created a huge uplift since the water could not flow away easily. In the positive superelevation cases, the

wave applied a downward force when it hit the deck, reducing the magnitude of the upward F_Y.

In the steady-state flow, the magnitude of F_Y of the negative superelevation cases is decreased by the support of water from the bottom of the deck; however, the effect was not observed in the bridges with a positive superelevation angle. In the steady-state, water overflowed the bridge, and the weight of water resulted in a downward load. In the negative superelevation cases, the bottom face was aiming towards the flow, allowing water to flow in and provide an uplift to the bridge, which reduces the resultant F_Y. In the positive superelevation cases, however, water could not get in between the girders and provide much less support to the bridge. The only location where water could provide an effective uplift was under the front overhanging deck. This was similar to the observation from Case 2 where the flow could not fill up the voids between the girders. Therefore, the positive superelevation cases experienced a similar magnitude of F_Y in the steady-state.

6.2.2 Resultant Moments

The resultant moments are presented in Figure 6.2. The resultant moments were primarily from the rolling moment M_Z. The pitching moment M_X and the spinning moments M_Y were much smaller compared to M_Z, and they were created by three-dimensional turbulence.

With superelevation, the greater influence of the F_X due to eccentricity and the variation in F_Y changed the magnitude M_Z significantly. For example, the $-10°$ case had a more negative M_Z at impact at about 15 seconds due to the increased F_X and F_Y. In steady-state flow, all bridges with superelevation experienced a greater magnitude of M_Z. For the negative case, the flow blocked by the front overhanging deck and the first girder created a horizontal force that resulted in a more negative M_Z. For the positive case, the front face of the overhanging deck and the first girder was aiming down. Even with the maximum superelevation ($10°$) considered, most of the effective area was still above the the origin of summing moments. Thus, a positive F_X would give a negative M_Z. On top of that, any uplift on the front of the bridge would always give a negative M_Z.

6.2.3 Horizontal Support Reactions

Figure 6.3 shows the histories of the horizontal reactions at the two corner supports on the left (FL_X and BL_X). The horizontal reactions are the magnitude of the resultant reactions in the directions of flow and abutment. The horizontal support reactions resisted F_X and M_Z only as seen in Figure 6.5, because the vertical force was decoupled. The F_X values are evenly distributed to all supports regardless of the superelevation angle. With no superelevation, the horizontal supports resisted no M_Z, because they lied on the same plane and did not form a couple. When the bridge was superelevated, the horizontal supports resisted M_Z with the greatest resistance at $\pm 10°$. The sign of M_Z resistance depends on the direction of superelevation. For example, a positive superelevation angle set support FL lower. Therefore, its reaction was positive to resist a negative M_Z.

The maximum horizontal reactions from each case were normalized by the maximum horizontal reactions from the case with no superelevation and plotted against the superelevation angle in Figure 6.4. It is obvious that the horizontal forces in the positive and negative superelevation cases have independent trends.

For the positive superelevation cases, the maximum horizontal reaction at impact increases at small angles of superelevation because of the larger effective area of the front face (only the front face matters, because the flow was not acting on the rest of the bridge.). At larger angles, the maximum horizontal reactions decrease since the effective area of the front faces begins to decrease. In steady-state, the increase in superelevation angle results in a larger horizontal reactions, because the effective area of the entire bridge has increased in proportion.

For the negative superelevation cases, the maximum horizontal reactions increase rapidly, because the flow was acting on the bottom face of the bridge including the surfaces between the girders, which results in a surface area much larger than just the front face as in the cases with positive superelevation. The maximum response increases to almost 2 times of that in the bridge with no superelevation, which indicates that bridges with superelevation

may experience a significant increase in the tsunami loads that is sensitive to the direction of incoming attack. In the steady-state, the front supports resisted most of the horizontal load, because the back supports were sticking up in the air.

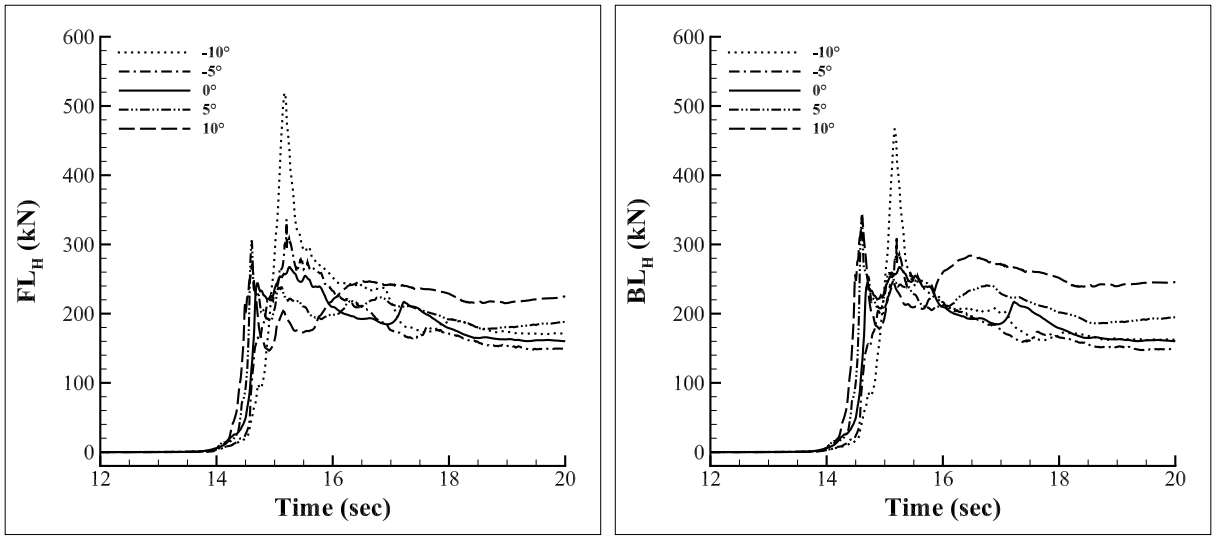

Figure 6.3: Histories of horizontal support reactions.

6.2.4 Vertical Support Reactions

Figure 6.6 shows the histories of the vertical reactions at the two corner supports on the left (FL_Y and BL_Y). Overall, the F_Y gets more negative as the superelevation angle decreases. Since the horizontal loads and the vertical reactions were decoupled, the vertical supports only resisted F_Y and M_Z, and their contributions to the demands are plotted in Figure 6.8.

F_Y is evenly distributed to the supports regardless of the superelevation angle as seen in Figure 6.8(a). The variation in F_Y from case to case is explained in Section 6.2.1.

The negative M_Z moment put the FL_Y and BL_Y of the superelevated bridges in compression and tension, respectively. This is purely due to the location of the vertical supports and how they worked as couples.

The maximum vertical reactions of each case are normalized in the same manner as in the

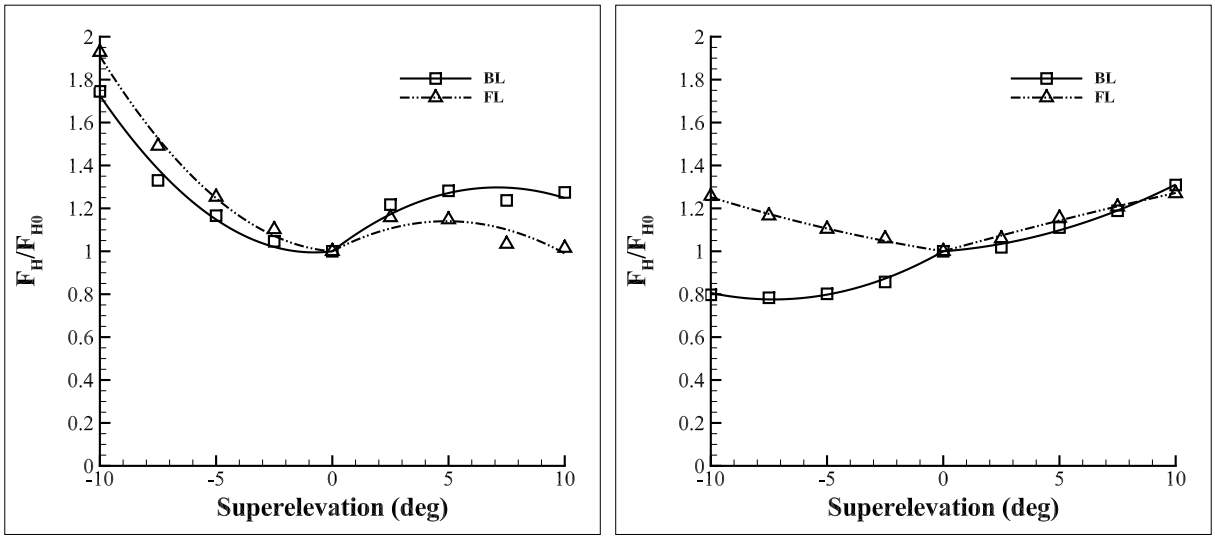

(a) Impact (b) Post-Impact

Figure 6.4: Normalized maximum horizontal support reactions as a function of slope gradient.

horizontal reactions and presented in Figure 6.7. Similar to the normalized maximum horizontal reactions, the positive and negative superelevation angles show their own independent trends.

In the negative superelevation cases, the vertical reactions change significantly as the superelevation angle increased. At impact, the wave is mostly hitting the front end of the bridge only. Since the increased superelevation made the horizontal supports resist M_Z more effectively, the vertical supports did not need to resist as much M_Z. Therefore, the front supports had to resist about two times the uplift as seen in Case 2 while the back supports were resisting only half of the uplift in Case 2. In steady-state, both the front and back supports were resisting much less downward force, with the rear supports resisting as little as 20% of the demand in Case 2. The huge reduction in downward resultant force means the bridge deck could be carried away by the flow much more easily.

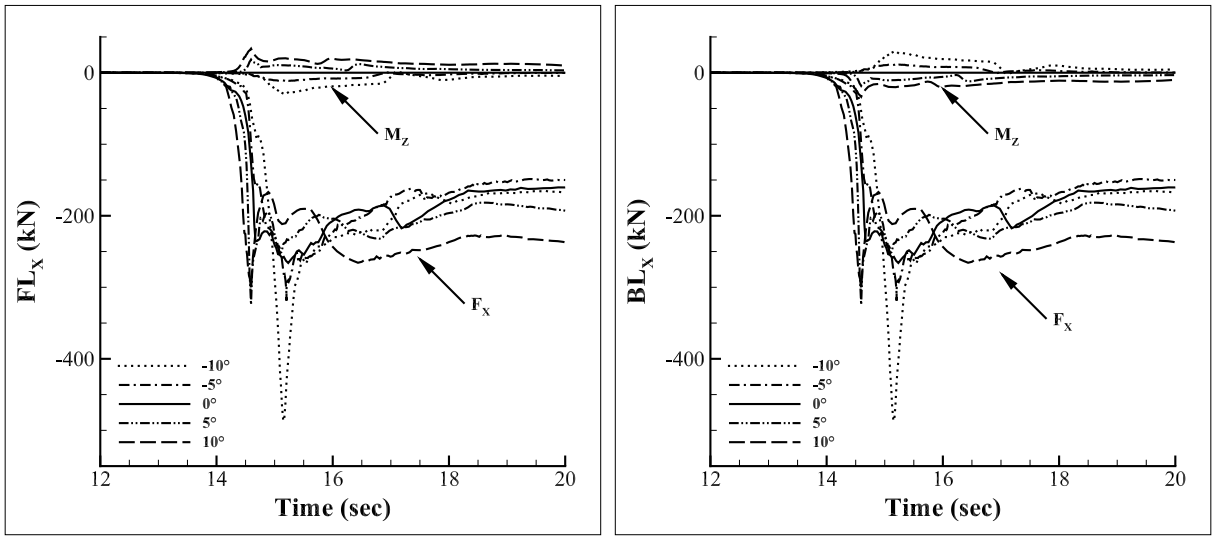

Figure 6.5: Contribution of horizontal force and spinning moment in direction of flows.

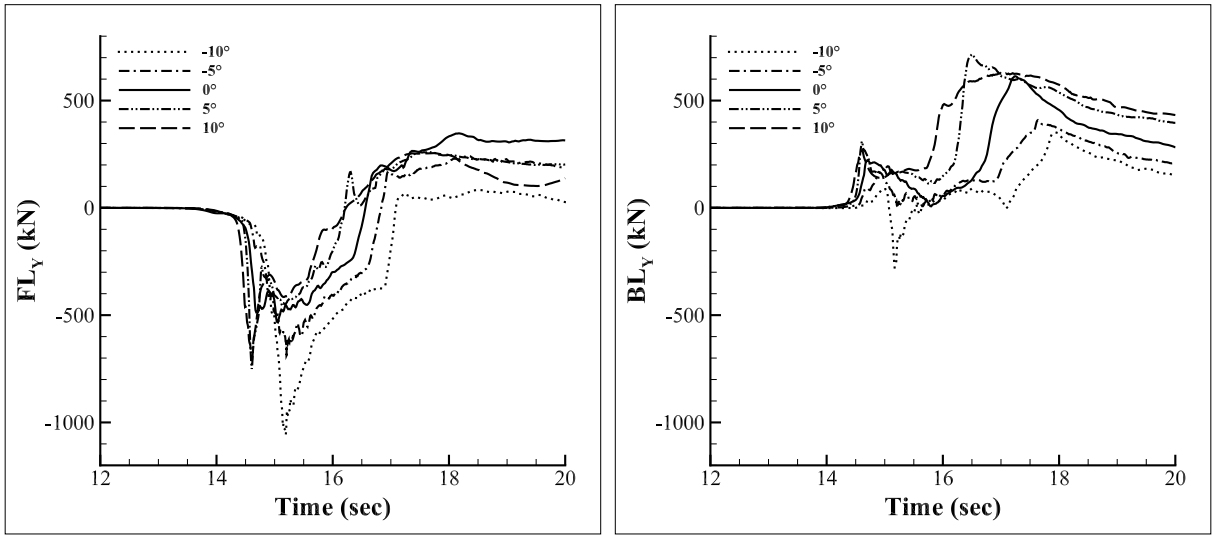

Figure 6.6: Histories of vertical support reactions.

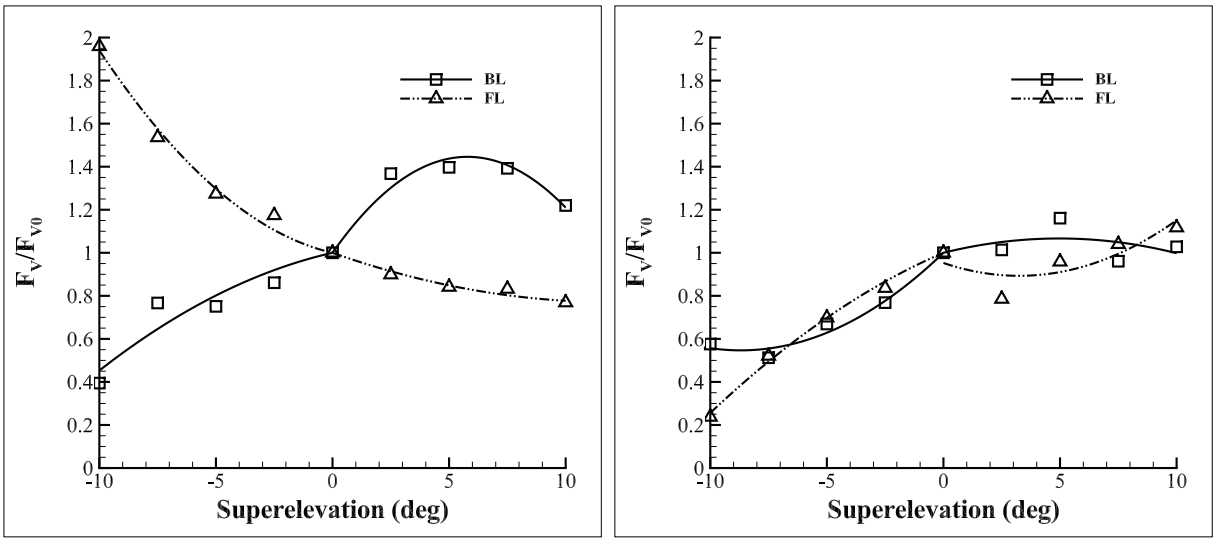

(a) Impact

(b) Post-Impact

Figure 6.7: Normalized maximum vertical support reactions as a function of slope gradient.

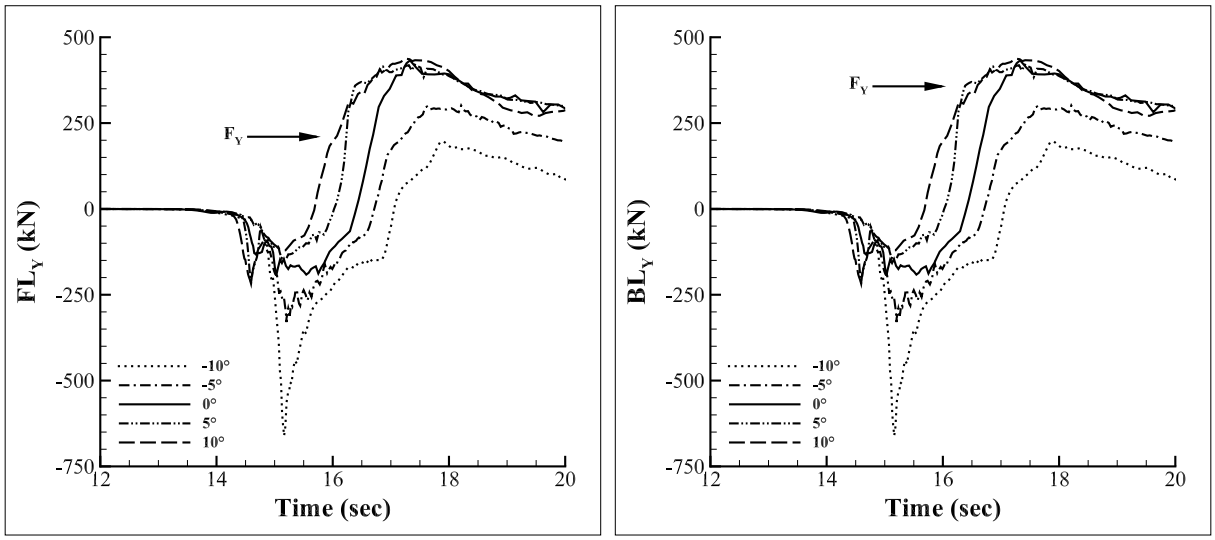

(a) Vertical Forces

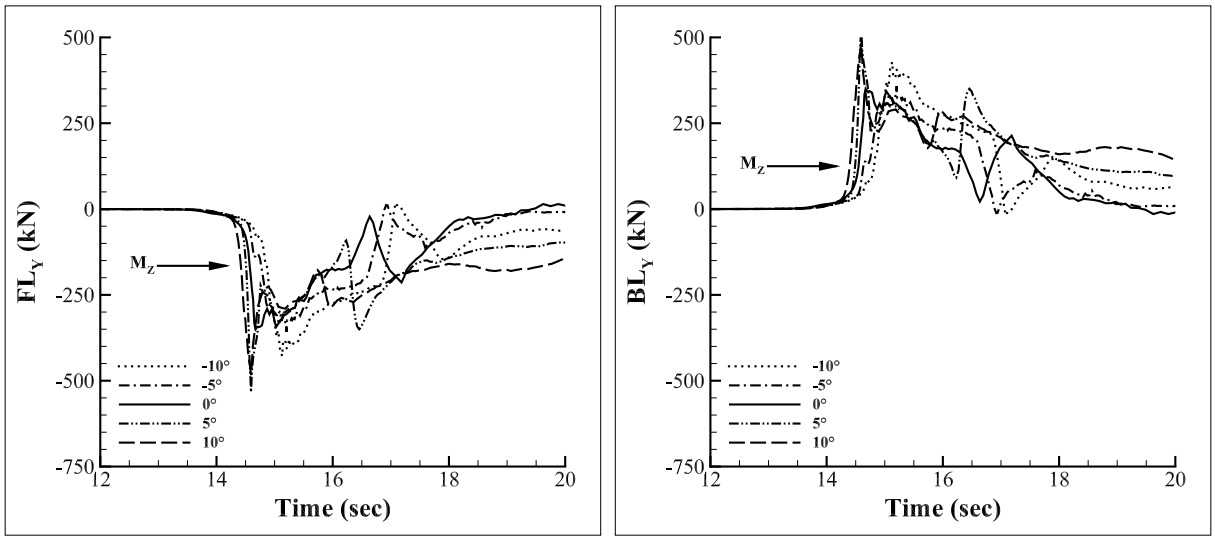

(b) Rolling Moments

Figure 6.8: Contribution of uplift force and pitching and rolling moments to the vertical support reactions

Chapter 7

CONCLUSION

Bridges designed in locations exposed to tsunami hazards are critical links in the lifelines to people in these regions. The designs of such bridges need to account for tsunami-induced loads to maintain safety and serviceability after the tsunami strikes.

The availability of affordable computing power and the performance-proven CFD solvers can provide structural engineers an effective way of understanding how tsunamis cause failures in bridges under various conditions. In the past, two-dimensional analyses have been the choice of researchers studying the effects of tsunamis on bridges, because three-dimensional simulations have been too computationally expensive to perform. Although two-dimensional analyses require less run time, they do not capture the effects of inherently three-dimensional characteristics, such as irregular geometries, local bathymetries and turbulence.

Technological advances in computing hardware and the implementation of parallelization capabilities in open-source computational fluid dynamics software, such as OpenFOAM, the toolbox used in this work, have enabled researchers to model the three-dimensional effects of tsunamis on bridges in a practical time-frame. The three-dimensional models presented in this work consistently completed in less than two days, which is a fraction time needed to complete some of the two-dimensional analyses done in the past. These analyses included the important three-dimensional effects that led to improved force predictions.

The development of the numerical models included mesh generation, property assignments, wave generations and load measurements. The flume was represented by a background mesh shaped as a rectangular prism. Then, the three-dimensional bridge structures were converted from computer-assisted drawing (CAD) models into a mesh and built into the background mesh automatically by an OpenFOAM utility (`snappyHexMesh`). After the

mesh generation, boundary conditions and initial values of the fluids were assigned. The tsunami waves were then generated by a dam-break setup, which included a reservoir of water and a dam that was removed at the beginning of an analysis, causing the water to flow down the flume and produce waves. The forces acting on the bridge superstructure were evaluated by summing the fluid pressure over the surface of the superstructure, and the moments were computed at the projected centroid on the plane of girder supports of the validated bridge model. The three-dimensional models were validated against experimental flume test data from the Public Works Research Institute [22]. The force predictions generally compared well with other force prediction methods reported from December 2014 at the UJNR Tsunami Workshop at Oregon State University [24]. The validation studies led to the following conclusions.

- Compared with the laminar-flow model, the Reynolds-Average Navier-Stokes (RANS) based k-ϵ turbulence solver can better simulate the tsunami inundations and therefore provide more realistic force predictions, because it does not include unphysical waves seen from the laminar flow solver.

- Three-dimensional models provides better force predictions than two-dimensional models even for bridge superstructures that can be represented in two dimensions subjected to a perpendicular flow, because the three-dimensional models account for effects of the bridge substructure, no-slip conditions and turbulence in three dimensions.

In this thesis, the effects of bridge skew, slope and superelevation were studied to investigate how changes in bridge superstructure geometry would affect support reactions. The simulation models were developed by rotating the experimentally validated bridge model in various directions and angles. The automatic mesh generation in OpenFOAM converted the bridge CAD models into meshes without the need for tedious manual input, making the parametric studies much easier than they would otherwise be.

The skewed, sloped and superelevated simulations demonstrated the increased risk of

failure at supports for girder bridges. Most cases had more uplift at impact and less downward force in steady-state in some or all supports.

- A skewed bridge has a front face that is not perpendicular to the flow direction. Consequently, the flow introduces force in the direction of abutments and spinning moment. In addition, the acute corners of a skewed bridge are further away from the bridge's centroid, causing greater pitching and rolling moments.

- A sloped bridge is inclined from an unsloped bridge and diverts flow in the longitudinal direction of the bridge, introducing forces perpendicular to the abutments and pitching moments.

- A superelevated bridge is rotated about the longitudinal axis of a bridge with no superelevation. With a larger effective area to the flow, the horizontal load increases. Bridges with a negative angle of superelevation sustain higher forces and moments, because their girders, which are facing the flow, concentrate the fluid pressure.

Girder bridges can be precast and rest on bearing pads with little or no reinforcements developed into their supports. With increased horizontal load, increased uplift and less downward load, the bridges were more vulnerable to being overturned or displaced by the tsunami flow than bridges without skew, slope, or superelevation. Of all the bridge models studied, the superelevated bridge with -10° superelevation was the most vulnerable. Some of its supports experienced about 200% horizontal reactions, 200% uplift and 20% downward of the load of the validated reference bridge model, making it more susceptible to the failures mentioned above.

The following concepts are suggestions to future tsunami-bridge modelling studies:

- Modifications to the fluid:

  - The fluid density can be increased to account for a mixture of sediments and smaller debris in tsunami flow to obtain a more accurate force predictions for

when the tsunami wave subsides and brings with it debris from the initial impact.

  - Larger debris can be modeled as a very dense and immiscible fluid that has very high viscosity using OpenFOAM's `multiphaseInterFoam`, a multiphase version of `interFoam`. The very high viscosity should prevent the debris from falling apart in the flow.
  - Scouring effects can be modeled by introducing a new, miscible fluid with appropriate density and viscosity around bridge substructure that represents soil. The flow will slowly carry the "soil" away and expose the substructure.

- Modifications to the mesh:
  - Parametric studies of combined effects of the bridge geometry (skew, slope, superelevation, curve, etc.) can improve structural engineers' understanding in tsunami loads.
  - As an alternative to using `multiphaseInterFoam`, larger debris can be modeled using `interDyMFoam`, an OpenFOAM solver that supports mesh motions and adaptive mesh refinements in runtime, or more practical software specifically designed to model floating solids.
  - Fluid-bridge interaction can be made possible by using `interDyMFoam` and implementing algorithms that changes the mesh boundaries according to the current load.
  - Variations in the local bathymetry such as channelization, surface roughness, etc., can be included by defining them in CAD models and incorporating them into the mesh.
  - The wave generation can be prepared in separate OpenFOAM cases or through modified boundary conditions to reduce the mesh size. Once the flow characteristics (velocity, wave height, etc.) are recorded, the flow can be generated in the flume by using proper inlet boundary conditions. An outlet can be imposed

as well at a downstream location sufficiently far away from the bridge without sacrificing accuracy of the model.

Specifically, this thesis investigated the effects of skew, slope and superelevation on the forces and reactions in bridges. More generally, this thesis demonstrated that it is practical (for a reasonable time frame and an affordable level of computational power) to perform three-dimensional simulations to study the impact of tsunamis on structures with irregular geometries. A similar strategy could be used to evaluate the effects of variations in bathymetry, and the effects of other hazards, such storm surges, on a wide variety of structures, including buildings and seawalls.

BIBLIOGRAPHY

[1] 3D Systems, Inc. StereoLithography Interface Specification. Part Number 50065-S01-00, October 1989.

[2] M. Akiyama, D. M. Frangopol, M. Arai, and S. Koshimura. Reliability of bridges under tsunami hazards: Emphasis on the 2011 Tohoku-Oki Earthquake. *Earthquake Spectra*, 29(S1):S295–S314, 2013.

[3] B. F. Atwater, M. Cisternas V., J. Bourgeois, W. C. Dudley, J. W. Hendley II, and P. H. Stauffer. Surviving a tsunami — lessons from Chile, Hawaii, and Japan. Circular 1187, U.S. Geological Survey, 2005.

[4] B. F. Atwater, M.-R. Satoko, S. Kenji, T. Yoshinobu, U. Kazue, and D. K. Yamaguchi. *The orphan tsunami of 1700: Japanese clues to a parent earthquake in North America*. University of Washington Press, 2005.

[5] BBC News. Logistical nightmare hampers Haiti aid effort. *BBC News America*, January 2010.

[6] S. Boon-Intra, S. C. Yim, S. B. Nimmala, and H. M. Winston. Development of a guideline for estimating tsunami forces on bridge superstructures. Master's thesis, Oregon State University, November 2010.

[7] I. Buckle. Lessons learned from the performance of highway bridges in recent earthquakes. In *2012 EERI Annual & National Earthquake Conference*, Memphis, Tennessee, April 2012. Earthquake Engineering Research Institute.

[8] G. Chock. ASCE 7 development of tsunami structural design provisions for the U.S. In *NEES Quake Summit 2014*, Anchorage, Alaska, July 2014. Earthquake Engineering Research Institute.

[9] Earthquake Engineering Research Institute. Learning from earthquakes: Bridge performance in the M_w 9.0 Tohoku, Japan, Earthquake of March 11, 2011. *EERI Special Earthquake Report*, October 2011.

[10] Earthquake Engineering Research Institute. Learning from earthquakes: The Tohoku, Japan, Tsunami of March 11, 2011: Effects on structures. *EERI Special Earthquake Report*, September 2011.

[11] E. L. Geist, G. R. Gelfenbaum, B. E. Jaffe, and J. A. Reid. Helping coastal communities at risk from tsunamis - the role of U.S. Geological Survey research. Fact Sheet 150-00, U.S. Geological Survey, 2000.

[12] A. Ghobarah, M. Saatcioglu, and I. Nistor. The impact of the 26 December 2004 earthquake and tsunami on structures and infrastructure. *Engineering Structures*, 28(2):312 – 326, 2006.

[13] H. Gokon and S. Koshimura. Mapping of building damage of the 2011 Tohoku earthquake tsunami in Miyagi Perfecture. *Coastal Engineering Journal*, 54(01):1250006, 2012.

[14] H. Iemura, M. H. Pradono, and Y. Takahashi. Report on the tsunami damage of bridges in banda aceh and some possible countermeasures. *Proceedings of the JSCE Earthquake Engineering Symposium*, 28:214–214, 2005.

[15] R. Ishiguro and S. Kitamura. Japan quake's economic impact worse than first feared. *Reuters.com Markets*, April 2011.

[16] R. W. Johnson. *The Handbook of Fluid Dynamics*, pages 8–3. CRC Press LLC, 1998.

[17] Y. Kawasaki and I. Kazuyuki. Mitigation of the impact of tsunami on bridges. In *Vienna Congress on Recent Advances in Earthquake Engineering and Structural Dynamics 2013*, Vienna, Austria, August 2013. Vienna University of Technology.

[18] T. L. Lau, T. Ohmachi, S. Inoue, and P. Lukkunaprasit. Experimental and numerical modelling of tsunami force on bridge decks. In M. Mokhtari, editor, *Tsunami - A Growing Disaster*, chapter 6, pages 105–130. InTech, December 2011.

[19] S. N. Livermore. Evaluation of tsunami design codes and recommendations for bridges susceptible to tsunami inundation. Master's thesis, University of Washington, 2014.

[20] T. P. Marshall. Hurricane Ivan damage survey. In *27th Conference on Hurricanes and Tropical Meteorology*, page P7.4, Monterey, California, April 2006. American Meteorological Society.

[21] M. R. Motley, H. K. Wong, X. Qin, and M. O. Eberhard. Tsunami-induced forces on skewed bridges. *Journal of Waterway, Port, Coastal and Ocean Engineering*, May 2015. Under review.

[22] H. Nakao, G. Zhang, T. Sumimura, and J. Hoshikuma. Effect of cross-sectional configuration of superstructure on hydrodynamic behavior of bridges subjected to tsunami-induced loading. *Journal of Japan Society of Civil Engineers, Ser. A1 (Structural Engineering & Earthquake Engineering (SE/EE))*, 69(4):I_42–I_54, February 2013.

[23] S. B. Nimmala, S. C. Yim, K. F. Cheung, and Y. Wei. Tsunami design criteria for constal infrastructure: A case study for Spencer Creek Bridge, Oregon. Report OR-RD-07-03, Oregon Department of Transportation, November 2006.

[24] Oregon State University College of Engineering. UJNR Tsunami Modeling Workshop. `https://secure.engr.oregonstate.edu/wiki/tsunamiworkshop/`, December 2014. [Online; accessed June 20, 2015].

[25] Pacific Tsunami Warning Center. PTWC history. `http://ptwc.weather.gov/ptwc/history.php`, November 2009. [Online; accessed June 20, 2015].

[26] J. Padgett, R. DesRoches, B. Nielson, M. Yashinsky, O. Kwon, N. Burdette, and E. Tavera. Bridge damage and repair costs from Hurricane Katrina. *Journal of Bridge Engineering*, January/February, 2008.

[27] X. Ren, Y. Morimoto, T. Nakamura, and N. Mizutani. Investigation of bridge failure caused by tsunami based on numerical method. In *Annual Meeting of the Chubu branch of JSCE*, Shinshu University, Nagano, Japan, February 2012. Japanese Society of Civil Engineers Chubu Branch.

[28] I. N. Robertson, H. R. Riggs, S. C. S. Yim, and Y. L. Yong. Lessons from Hurricane Katrina storm surge on bridges and buildings. *Journal of Waterway, Port, Coastal and Ocean Engineering*, 133(6):463–483, November/December 2007.

[29] The OpenFOAM Foundation. The OpenFOAM user guide. `http://foam.sourceforge.net/docs/Guides-a4/UserGuide.pdf`, 2015. [Online; accessed June 20, 2015].

[30] UN News Center. As pledges for tsunami victims top $1.1 billion, Annan says logistics is biggest challenge. *United Nation News Service*, December 2004.

[31] S. Unjoh and K. Endoh. Damage investigation and the preliminary analyses of bridge damage caused by the 2004 Indian Ocean tsunami. In *38th Joint Meeting*, Gaithersburg, Maryland, May 2006. U.S.-Japan Cooperative Program in Natural Resources Panel on Wind and Seismic Effects.

[32] M. Yashinsky. Lessons learned from the March 11, 2011 M9.0 Great Tohoku earthquake and tsunami. In *International symposium on engineering lessons learned from the 2011 Great East Japan Earthquake*. Japan Association for Earthquake Engineering, 2012.

[33] S. C. Yim and M. Azadbakht. Tsunami forces on selected California coastal bridges. Report CA13-1983, State of California Department of Transportation, June 2013.